Ph.D. Thesis

Earthquake-induced thermal maturation of carbonaceous materials and its implication for earthquake dynamics in plate-subduction zones

Shunya Kaneki

Department of Earth and Space Science,
Graduate School of Science, Osaka University

February, 2019

Abstract

Earthquakes that occur at plate-subduction zones can trigger destructive tsunami and thus endanger coastal area, yet our understanding about earthquake dynamics in subduction zones still remains poor, leading to difficulties in assessing the risks related to the future events. One of the dominant factors controlling earthquake dynamics is the amount of seismic energy consumed as frictional heat in the slip zones, which constitutes the largest part of total seismic budget and triggers various physic-chemical reactions in faults. For evaluating frictional heat recorded in fault rocks, various thermal proxies have been suggested. In particular, thermal reactions of carbonaceous material (CM) have been received considerable attention as a candidate of thermal index, because CM changes its organochemical characteristics irreversibly in response to maximum temperature. However, there is currently no systematic study that focuses on earthquake-induced CM reactions, and it is thus still unclear whether CM reactions can be a indicator of frictional heat.

Another important factor dictating earthquake dynamics is frictional strength of rocks. Previous studies suggest that typical crust-forming materials show friction coefficient of 0.65–0.80 and 0.1–0.4 at slow and fast slip rate, respectively. However, in the case if frictionally weak minerals exist, frictional strength of fault rocks become much lower than these typical values. CM is one of the representative weak materials that show low friction, and previous studies imply that CM is likely to lose its strength with increasing maturity. Considering relatively high concentration of CM at plate-subduction zones, CM reactions may affect strength of plate-subduction faults, yet we know little about its influence on earthquake dynamics.

In this thesis, I attempt to reveal physico-chemical processes of earthquake-induced CM reactions and its implications on earthquake dynamics in plate-subduction zones. In Chapter 1, an outline and a goal of this study is described, including general information about frictional heat and frictional strength of faults.

Chapter 2 experimentally investigates the possibility to detect heat recorded in fault rocks in terms of visible spectroscopy on CM-bearing fault materials. I demonstrated the blackening of synthetic mixtures of montmorillonite and CM and of montmorillonite and magnetite in milling, heating, and friction experiments. Color measurements on these samples before and after experiments showed that milling of black materials can result in blackening of fault rocks, and heating of CM can strengthen blackening possibly due to adsorption of

pyrolyzed gas onto clay surface. Therefore, relatively black gouge in natural faults may have experienced earthquake-induced high temperature, and this information can be useful to identify fault zones in field.

Chapter 3 examines earthquake-induced thermal reactions of CM in natural faults. I performed spectroscopic, thermogravimetric, and organic elemental analyses in conjunction with heating experiments, and demonstrated that CM in fault rocks retrieved from Shimanto accretionary complex showed similar organochemical characteristics to those of CM from surrounding host rocks heating after 500–600 °C. This indicates that CM maturity can be a strong indicator for detecting frictional heat. Numerical modeling showed that, for achieving such temperatures, earthquake event with displacement of 2–9 m is required in the studied fault. Thus, CM reactions that changes its maturity is useful not only to estimate frictional heat but also to understand earthquake dynamics in subduction zones.

In Chapter 4 and 5, I investigated both kinetic effects caused from mechanochemistry and heating rate on CM reactions for establishing CM as a more plausible thermal indicator. I conducted laboratory friction and heating experiments on CM, and evaluated both effects on CM maturation by means of spectroscopies. The results showed that mechanochemical effect on CM, which is a typical effect caused from earthquake slip and can reduce activation energy of various reactions, can promote CM reactions being occurred at relatively lower temperature. In contrast, higher heating rate, another typical condition of seismic event, can inhibit CM reactions due to its kinetic effect. These facts suggest that CM reactions during earthquake slip can be controlled by many factors, and fault geothermometer based on CM maturity should be established by considering these complicated effects.

In Chapter 6, I show how CM maturity affects on frictional strength of CM-bearing faults. High-velocity friction experiments on CM with different maturity verified that increase in crystallinity of CM can decrease its yield shear strength, possibly affecting rupture dynamics. Given that CM increases its maturity with progressive diagenetic reactions and earthquake events, carbon-bearing plate-subduction faults can lose its strength with increasing depth, possibly affecting depth-dependent rupture dynamics in subduction zones.

In Chapter 7, I briefly summarize the main results of this thesis. I also identify unsolved problems related to this thesis as future works. The important findings and overall conclusions of this thesis are as follows: (1) CM reactions can be a useful indicator for frictional heat, (2) earthquake-induced effects can affect progress of CM reactions, and (3) CM reactions may dominantly control frictional strength and thus rupture dynamics of plate-subduction faults.

Acknowledgements

I would like to thank my supervisor Prof. Dr. Tetsuro Hirono at Osaka University for his valuable and insightful discussions, experimental and analytical supports, and a lot of encouragements on completing this Ph.D. thesis. I also greatly appreciate the people involved in this thesis; Dr. Hideki Mukoyoshi for his support on field surveys, Dr. Wataru Tanikawa and Dr. Osamu Tadai for their technical assistances on XRD measurements, Dr. Akihiro Ito for his technical assistance on TEM observations, Prof. Dr. Minoru Ikehara for his support on elemental analysis, Prof. Dr. Yoshikazu Sampei for his effort on chemical treatment of CM, Prof. Dr. Kentaro Terada, Dr. Yosuke Kawai, and Prof. Dr. Tadashi Kondo for their helps on experimental procedures, and Dr. Kiyokazu Oohashi for his assistance on friction experiments. I am also grateful for my current and previous lab members not only for their helps on science but also for a lot of fun time with them in daily life. Some researches in this thesis are financially supported by JSPS Research Fellowship DC1. Finally, I sincerely thank to my family for their many supports.

Table of contents

Chapter 1

General introduction

Among various disasters triggered by natural hazards, earthquake has been considered as the most destructive one, because it causes significant damage on human life, public property, and social economy (Guha-Sapir et al., 2016). In addition, earthquake can induce urban fire, landslide, liquefaction, subsidence, and tsunami, all of which cause strong damages on our life as earthquake itself does. Therefore, assessments of the risks related to earthquake events have been in urgent requirement to minimize the influence of seismic events on the society. This requires the comprehensive understandings on earthquake dynamics, and the plausible model, which considers earthquake nucleation, rupture propagation, frictional fault slip, and fault healing processes, is also necessary. However, in spite of the several decades of studies, our knowledge about earthquake dynamics still remains poor, and thus the sophisticated model that can consistently explain complex processes associated with earthquake is not well established.

Earthquakes usually take place at (1) plate-boundary faults, and (2) inland active faults. Regular earthquakes with large magnitude usually happen in and around plate-subduction zones (i.e., plate convergent margin), where approximately 85 % of total seismic energy on Earth is released (Scholz, 2002). Furthermore, earthquakes occurred at these areas sometimes trigger sudden uplift of the sea surface and generate destructive tsunami if the rupture propagates to the seafloor, represented by the 2004 Sumatra earthquake and the 2011 Tohoku-Oki earthquake. It is therefore of great importance to improve our understandings on earthquake dynamics in plate-subduction zones, which may enable us to evaluate the potential risks of future destructive events.

Earthquake has been considered to occur as a result of a sudden release of elastic energy by frictional slip along fault. The released energy is considered to divided into three parts: (1) fracture energy E_G, (2) radiation energy E_R, and (3) frictional heat E_H (Figure 1.1).

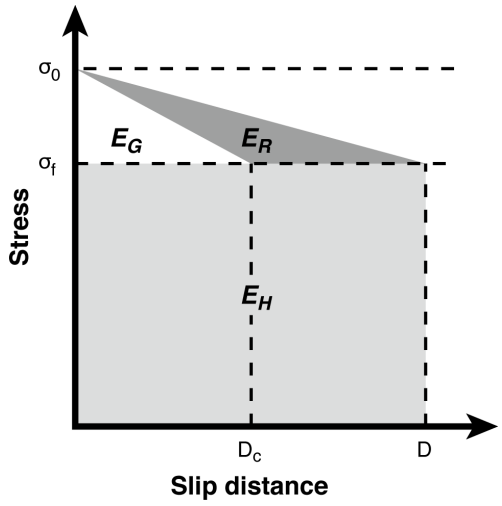

Figure 1.1. Seismic energy budget on the basis of a simple slip-weakening model. σ_0, peak shear stress; σ_f, residual shear stress.

E_G is the energy required to advance the rupture front forward, which is defined as the integral of the changes in the shear strength over the local slip (Abercrombie & Rice, 2005). In the case of natural earthquakes, E_G is used for comminution of the particles that induces grain size reduction and amorphization of lattice crystals (Brantut et al., 2008). Many studies have attempted to quantitatively evaluate comminution energy (e.g., Olgaard & Brace, 1983; Yoshioka, 1986; Chester et al., 2005; Pittarello et al., 2008; Togo & Shimamoto, 2012), as it can be easily estimated from grain size distribution or surface area of gouge materials. These studies suggested that the energy used for comminution constitutes small part of E_G (less that 10 %) and of total seismic energy (less than 1 %). Similarly, Brantut et al. (2008) conducted laboratory friction experiments and concluded that the energy used for amorphization is also small part of E_G, suggesting that most part of E_G may be converted into E_R or E_H. These studies clearly verified that E_G constitutes very small part of total seismic energy. The amount of radiated energy E_R can be calculated independently from seismological observations (e.g., Venkataraman & Kanamori, 2004; Abercrombie & Kanamori, 2005; Yamada et al., 2007). E_R is the energy used for generation of seismic wave, and previous researches have examined its ratio to total seismic moment M_0 or to fracture energy E_G. Venkataraman & Kanamori (2004) calculated radiation efficiency, η_R, for many earthquakes at plate-subduction zones, and demonstrated that

E_R is much smaller than E_G. Thus, E_R is also likely to constitute very small part of total seismic energy budget, and most of the seismic energy should convert into E_H in the slip zones (e.g., Chester et al., 2005; Brantut et al., 2008). E_H is the heat energy that triggers sudden temperature rise and promotion of various physico-chemical reactions in slip zones, which in turn affects fault slip motion and energetics of earthquake (Rowe & Griffith, 2015). These reactions include melt lubrication (Hirose & Shimamoto, 2005), flash heating (Rice, 2006), thermal and thermo-chemical pressurization (Sibson, 1973; Brantut et al., 2010; Tanikawa et al., 2015), and nanopowder lubrication (Reches & Lockner, 2010), all of which can directly reduce frictional strength of faults. Estimation of E_H is thus of great importance for understanding not only earthquake energetics but also earthquake dynamics.

Cowan (1999) investigated various potential proxies for estimation of E_H, and concluded that existence of pseudotachylyte (frictional melt of rock-forming minerals) (e.g., Sibson, 1975) is the only reliable evidence that can detect earthquake-related heat recorded in faults. However, thanks to the development of analytical techniques, other potential heat proxies have been reported in recent two decades (Rowe & Griffith, 2015). These include thermal transformation of minerals (e.g., Mishima et al., 2009; Evans et al., 2014), thermal decomposition of carbonates (e.g., Han et al., 2007), dehydration and dehydroxylation of clays (e.g., Hirono et al., 2008; Schleicher et al., 2015), high-temperature fluid-rock interaction (e.g., Ishikawa et al., 2008), and thermal maturation of carbonaceous material (e.g., O'Hara, 2004). Among these reactions, thermal maturation of carbonaceous material (CM) has been received a marked attention, because CM changes its organochemical characteristics irreversibly with increasing temperature. and thus its maturity is a candidate of a reliable thermal index for estimating E_H.

CM is a photosynthesis-derived insoluble organic matter that exists in fault rocks (e.g., Kuo et al., 2014) and in the seafloor sediments (Premuzic et al., 1982), and is enriched in plate-subduction zones (≥1 wt.%; see Figure 6.1). CM changes its organochemical characteristics, including elemental composition (C, H, O, N, and S) and molecule structure, in response to the ambient temperature (e.g., Schito et al., 2017). The degree of its maturity can be

determined by reflectance measurements (e.g., O'Hara, 2004), spectroscopies (e.g., Beyssac et al., 2002), and GC/MS analyses (e.g., Polissar et al., 2011), and thus CM is often used to evaluate paleo-temperatures experienced by sedimentary and metamorphic rocks (e.g., Beyssac et al., 2002; Kouketsu et al., 2014). Importantly, CM reactions are sensitive to short-term flash heating during earthquakes (e.g., O'Hara et al., 2006), suggesting that CM may be a strong proxy for estimating earthquake-related maximum temperature of fault rocks. However, studies focusing on earthquake-induced CM reactions have been hardly reported, and thus, for assessing the potential of CM being a reliable indicator to detect heat associated with earthquake, further investigations from both natural and experimental approaches are required.

Another important factor when considering earthquake dynamics is the frictional strength of fault rocks. Typical friction coefficient μ of crust-forming rocks, such as granite and sandstone, ranges from 0.65–0.80 at slow slip velocity (Byerlee, 1978). On the other hand, at fast slip velocity in order of 10^{-1}–10^{0} m s^{-1}, friction coefficient of rocks shows dynamic weakening trend and become 0.1–0.4 at final stage of slip (Di Toro et al., 2011). Although these trends can be basically applicable for various rocks regardless of rock types, however, existence of frictionally weak materials in fault rocks can reduce fault strength below these typical values. For example, frictionally weak smectite, which is a common material in shallow part of plate-subduction zones (e.g., Chester et al., 2013), can dramatically reduce frictional strength of quartz gouge with bulk concentration of ≥10 wt.% (Oohashi et al., 2015). In the case of pure CM, its friction coefficient shows relatively lower value (μ of ~0.5) compared to typical rocks at slow slip velocity (Oohashi et al., 2011). Furthermore, fully matured CM (graphite) shows significantly low frictional resistance (μ of ~0.1) at both slow and fast slip velocities, suggesting that CM maturation can affect its frictional resistance and thus may play an important role in earthquake dynamics of CM-bearing faults in plate-subduction zones. However, there is currently no systematic trial examining frictional strength of CM with increasing maturity and its relation to earthquake dynamics.

On the basis of these problems and backgrounds, in this thesis, I aim (1) to assess the potential of earthquake-related CM reactions as a new proxy for detecting frictional heat, and

(2) to investigate the effects of CM reactions on earthquake dynamics in plate-subduction zones. The resultant data and its implications in this thesis can provide a new insight into the earthquake-related CM reactions and its possible relation to earthquake dynamics in plate-subduction zones.

References

Abercrombie, R.E. & Rice, J.R. (2005). Can observations of earthquake scaling constrain slip weakening? *Geophys. J. Int.* **162**, 406–424.

Beyssac, O., Goffé, B., Chopin, C. & Rouzaud, J.N. (2002). Raman spectra of carbonaceous material in metasediments: a new geothermometer. *J. Metamorph. Geol.* **20**, 859–871.

Brantut, N., Schubnel, A., Rouzaud, J.-N., Brunet, F. & Shimamoto, T. (2008). High-velocity frictional properties of a clay-bearing fault gouge and implications for earthquake mechanics. *J. Geophys. Res.* **113**, B10401.

Brantut, N., Schubnel, A., Corvisier, J. & Sarout, J. (2010). Thermochemical pressurization of faults during coseismic slip. *J. Geophys. Res.* **115**, B05314.

Byerlee, J. (1978). Friction of rocks. *Pure Appl. Geophys.* **116**, 615–626.

Chester, F.M. *et al*. (2013). Structure and composition of the plate-boundary slip zone for the 2011 Tohoku-Oki earthquake. *Science* **342**, 1208–1211.

Chester, J.S., Chester, F.M. & Kronenberg, A.K. (2005). Fracture surface energy of the Punchbowl fault, San Andreas system. *Nature* **437**, 133–136.

Cowan, D.S. (1999). Do faults preserve a record of seismic slip? A field geologist's opinion. *J. Struct. Geol.* **21**, 995–1001.

Di Toro, G., Han, R., Hirose, T., De Paola, N., Nielsen, S., Mizoguchi, K., Ferri, F., Cocco, M. & Shimamoto, T. (2011). Fault lubrication during earthquakes. *Nature* **471**, 494–498.

Evans, J.P., Prante, M.R., Janecke, S.U., Ault, A.K. & Newell, D.L. (2014). Hot faults: Iridescent slip surfaces with metallic luster document high-temperature ancient seismicity in the Wasatch fault zone, Utah, USA. *Geology* **42**, 623–626.

Guha-Sapir, D., Hoyois, P. & Below, R. (2016). *Annual Disaster Statistical Review 2016: The Numbers and Trends*. Brussels: Creed.

Han, R., Shimamoto, T., Hirose, T., Ree, J.-H. & Ando, J. (2007). Ultralow friction of carbonate faults caused by thermal decomposition. *Science* **316**, 878–881.

Hirono, T. *et al*. (2008). Clay mineral reactions caused by frictional heating during an earthquake: An example from the Taiwan Chelungpu fault. *Geophys. Res. Lett.* **35**, L16303.

Hirose, T. & Shimamoto, T. (2005). Growth of molten zone as a mechanism of slip weakening of simulated faults in gabbro during frictional melting. *J. Geophys. Res.* **110**, B05202.

Ishikawa, T. *et al*. (2008). Coseismic fluid–rock interactions at high temperatures in the Chelungpu fault. *Nat. Geosci.* **1**, 679–683.

Kouketsu, Y., Mizukami, T., Mori, H., Endo, S., Aoya, M., Hara, H., Nakamura, D. & Wallis, S. (2014). A new approach to develop the Raman carbonaceous material geothermometer for low-grade metamorphism using peak width. *Island Arc* **23**, 33–50.

Kuo, L.-W. *et al*. (2014). Gouge graphitization and dynamic fault weakening during the 2008 Mw 7.9 Wenchuan earthquake. *Geology* **42**, 4570–4573.

Mishima, T., Hirono, T., Nakamura, N., Tanikawa, W., Soh, W. & Song, S.-R. (2009). Changes to magnetic minerals caused by frictional heating during the 1999 Taiwan Chi-Chi earthquake. *Earth Planets Space* **61**, 797–801.

O'Hara, K. (2004). Paleo-stress estimates on ancient seismogenic faults based on frictional heating of coal. *Geophys. Res. Lett.* **31**, L03601.

O'Hara, K., Mizoguchi, K., Shimamoto, T. & Hower, J.C. (2006). Experimental frictional heating of coal gouge at seismic slip rate: Evidence for devolatilization and thermal pressurization of gouge fluids. *Tectonophysics* **424**, 109–118.

Olgaard, D.L. & Brace, W.F. (1983). The microstructure of gouge from a mining-induced seismic shear zone. *Int. J. Rock Mech. Mining Sci.* **20**, 11–19.

Oohashi, K., Hirose, T. & Shimamoto, T. (2011). Shear-induced graphitization of carbonaceous materials during seismic fault motion: Experiments and possible implications for fault

mechanics. *J. Struct. Geol.* **33**, 1122–1134.

Oohashi, K., Hirose, T., Takahashi, M. & Tanikawa, W. (2015). Dynamic weakening of smectite-bearing faults at intermediate velocities: Implications for subduction zone earthquakes. *J. Geophys. Res.* **120**, 1572–1586.

Rice, J.R. (2006). Heating and weakening of faults during earthquake slip. *J. Geophys. Res.* **111**, B05311.

Pittarello, L., Di Toro, G., Bizzarri, A., Pennacchioni, G., Hadizadeh, J. & Cocco, M. (2008). Energy partitioning during seismic slip in pseudotachylyte-bearing faults (Gole Larghe Fault, Adamello, Italy). *Earth Planet. Sci. Lett.* **269**, 131–139.

Polissar, P.J., Savage, H.M. & Broadsky, E.E. (2011). Extractable organic material in fault zones as a tool to investigate frictional stress. *Earth Planet. Sci. Lett.* **311**, 439–447.

Reches, Z. & Lockner, D.A. (2010). Fault weakening and earthquake instability by powder lubrication. *Nature* **467**, 452–455.

Rowe, C. & Griffith, W.A. (2015). Do faults preserve a record of seismic slip: A second opinion. *J. Struct. Geol.* **78**, 1–26.

Premuzic, E.T., Benkovitz, C.M., Gaffney, J.S. & Walsh, J.J. (1982). The nature and distribution of organic matter in the surface sediments of world oceans and seas. *Org. Geochem.* **4**, 63–77.

Schleicher, A.M., Boles, A. & van der Pluijm, B.A. (2015). Response of natural smectite to seismogenic heating and potential implications for the 2011 Tohoku earthquake in the Japan Trench. *Geology* **43**, 755–758.

Scholz, C.H. (2002) *The Mechanics of Earthquakes and Faulting* (Cambridge Univ. Press).

Sibson, R.H. (1973). Interactions between temperature and pore-fluid pressure during earthquake faulting and a mechanism for partial or total stress relief. *Nature* **243**, 66–68.

Sibson, R.H. (1975). Generation of pseudotachylyte by ancient seismic faulting. *Geophys. J. Int.* **43**, 775–794.

Tanikawa, W., Ishikawa, T., Honda, G., Hirono, T. & Tadai, O. (2015). Trace element anomaly in fault rock induced by coseismic hydrothermal reactions reproduced in laboratory

friction experiments. *Geophys. Res. Lett.* **42**, 3210–3217.

Togo, T. & Shimamoto, T. (2012). Energy partition for grain crushing in quartz gouge during subseismic to seismic fault motion: An experimental study. *J. Struct. Geol.* **38**, 139–155.

Venkataraman, A. & Kanamori, H. (2004). Observational constraints on the fracture energy of subduction zone earthquakes. *J. Geophys. Res.* **109**, B05302.

Yamada, T., Mori, J.J., Ide, S., Abercrombie, R.E., Kawakata, H., Nakatani, M., Iio, Y. & Ogasawara, H. (2007). Stress drops and radiated seismic energies of microearthquakes in a South African gold mine. *J. Geophys. Res.* **112**, B03305.

Yoshioka, N. (1986). Fracture energy and the variation of gouge and surface roughness during frictional sliding of rocks. *J. Phys. Earth* **34**, 335–355.

Chapter 2

Blackening of fault gouge by comminution and pyrolysis of carbonaceous materials during earthquake slip

Reprinted from *Tectonophysics* **677–678**, 160–170. Kaneki, S. & Hirono, T. (2016). Blackening of fault gouge by comminution and pyrolysis of carbonaceous materials during earthquake slip, with permission from Elsevier.

Abstract

Black fault gouges sometimes develop, mainly in sedimentary rocks, but the cause of the color transformation is not well understood. Here we demonstrated the blackening of synthetic mixtures of montmorillonite and bituminous coal and of montmorillonite and magnetite in milling, heating, and friction experiments. Mixed samples with a higher volume fraction of coal or magnetite before the experiments showed lower L* values (lightness index; lower values indicate darker blacks), because coal and magnetite are intrinsically black. The milling and heating experiments showed that the L* values of mixed samples of montmorillonite and coal drastically decreased with longer milling times and higher temperatures. The L* values of mixed samples of montmorillonite and magnetite also decreased with longer milling times, but no notable change was observed in the samples after the heating experiments. Because comminution by milling induces granulation of the constituent materials, blackening of the experimental samples was primarily caused by dispersal through the sample of fine black particles such as coal and magnetite, but it could be strengthened by adsorption onto host particles of organic gases produced by pyrolysis of carbonaceous material (CM) at high temperature. The friction experiment with mixed samples of montmorillonite and coal produced the remarkably low L* values. Friction induces both comminution and heating of samples, so the blackening could be greater than after either milling or heating alone. Therefore, relatively black fault gouges, compared with the surrounding host rocks, might have experienced comminution and heating, probably related to earthquake slip. Thus, black coloration could be one of the important information on fieldwork.

2.1. Introduction

Fault gouges often differ in color from the surrounding host rock, and when the host rock is of sedimentary origin, relatively black fault gouges are often observed (e.g., Manatchal, 1999; Tsutsumi et al., 2004; Buatier et al., 2012; Yao et al., 2013; Balsamo et al., 2014). The main damage zone of the Chelungpu fault, which slipped during the 1999 Taiwan Chi-Chi

earthquake, is very black (Hirono et al., 2006, 2007a). High magnetic susceptibility in this zone has been attributed to the new formation of magnetic minerals such as magnetite and maghemite at high temperatures induced by friction (Hirono et al., 2006; Mishima et al., 2009; Chou et al., 2012). Tanikawa et al. (2008) experimentally reproduced the blackening of fault gouge by subjecting a host-rock sample to high-velocity (on the order of 1 m s^{-1}) friction, and they suggested that the color change resulted from the new formation of black magnetic minerals. However, the small amount of magnetic minerals (<1 wt.%) in the black gouge of the Chelungpu fault zone (Hirono et al., 2014) would be unlikely to affect the color of the bulk rock.

Because determination of the peak temperature reached during slip is crucial for identifying the faulting mechanism of an earthquake, various temperature proxies have been proposed, for example, magnetite formation at high temperature (≥400 °C) (Mishima et al., 2009; Chou et al., 2012); anomalies in the concentrations of fluid-mobile trace elements (Sr, Cs, Rb, and Li) and in the Sr isotope ratios, indicating the presence of high-temperature (≥350 °C) fluid (Ishikawa et al., 2008); dehydroxylation of clay minerals (Hirono et al., 2008); thermal decomposition of carbonate minerals (Han et al., 2007; Hirono et al., 2007b); and thermal maturation of carbonaceous material (CM), as indicated by vitrinite reflectance (O'Hara et al., 2006; Sakaguchi et al., 2007; Maekawa et al., 2014) and by infrared and Raman spectroscopy (Hirono et al., 2015). However, these proxies require sophisticated laboratory analyses; an easy method for preliminary detection of a record of high temperature in the field is needed.

In this study, we used a high-velocity friction apparatus, a thermogravimetric (TG)–differential scanning calorimeter (DSC), and a milling machine to produce blackening in synthetic fault samples, and we used color digital spectrophotometry and pyrolysis–gas chromatography–mass spectrometry (py-GC/MS) to evaluate color changes and the organic chemical properties of the samples. We then considered how comminution and pyrolysis of CMs contributed to the blackening.

2.2. Materials and methods

2.2.1. Samples

As analogues of fault gouge components, we used Na-rich montmorillonite (Crook County, Wyoming, USA; SWy-2 supplied from The Clay Minerals Society) and bituminous coal (Ashibetsu, Hokkaido, Japan). We also used magnetite (Diamantina, Minas Gerais, Brazil), because the color change in the Chelungpu fault was ascribed to black magnetic minerals (Tanikawa et al., 2008). Their reported grain densities are 2800, 1300, and 5200 kg m^{-3}, respectively (Meyers, 1983; Schön, 2004; Holmboe et al., 2012). We investigated the process and mechanism of the color transition caused by the effects of high-velocity friction, milling, and heating on montmorillonite samples and on mixtures of montmorillonite and coal in three series of experiments. We also examined color changes in mixtures of montmorillonite and magnetite in milling and heating experiments. All samples were dried at 50 °C for several hours just before each experiment.

Before the experiments, we characterized the Ashibetsu bituminous coal thermochemically by using a TG-DSC apparatus (STA 449 C Jupiter balance, Netzsch) to heat the coal to 800 °C at a rate of 10 °C min^{-1} under an Ar atmosphere; the resultant TG profile indicated a weight loss was started at approximately 150 °C and a large amount of weight loss occurred above approximately 400 °C (Figure 2.1).

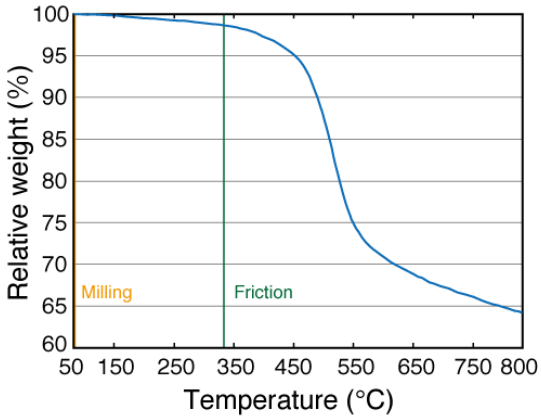

Figure 2.1. Thermogravimetric curve of the Ashibetsu bituminous coal. Maximum temperatures reached during the friction and milling experiments were approximately 330 and 40 °C, respectively.

We analyzed the bituminous coal on the molecular level by py-GC/MS, using a pyrolyzer (Py-3030D, Frontier Lab; furnace temperature 700 °C, interface temperature 330 °C) directly coupled to a gas chromatograph–mass spectrometer (GCMS-QP2010 Ultra, Shimadzu) equipped with a DB-5MS column (length 30 m, inner diameter 0.25 mm, film thickness 0.25 μm; Agilent J&W). Approximately 1 mg of the coal sample was heated from 100 to 330 °C at a rate of 50 °C min^{-1} under vacuum, and the gas-phase pyrolysates that were collected in a cryotrap were analyzed by GC/MS. In the GC/MS analysis, helium was used as the carrier gas at a flow rate of 1 mL min^{-1}, and the split ratio was 50. The injection temperature was 300 °C, and the column temperature program was as follows: hold at 40 °C for 2 min, heat to 310 °C at 15 °C min^{-1}, and hold at 310 °C for 10 min. The mass spectrometer was operated in the electron ionization mode (70 eV, scan range m/z 35–600, scan interval 0.2 s), and the ion source temperature was kept at 230 °C. The pyrolysates were identified by comparing their mass spectra with the reported spectra of standards in the library of the National Institute of Standards and Technology. The resultant pyrogram of the Ashibetsu bituminous coal showed abundant naphthalene and normal chain aliphatic hydrocarbons (Figure 2.2).

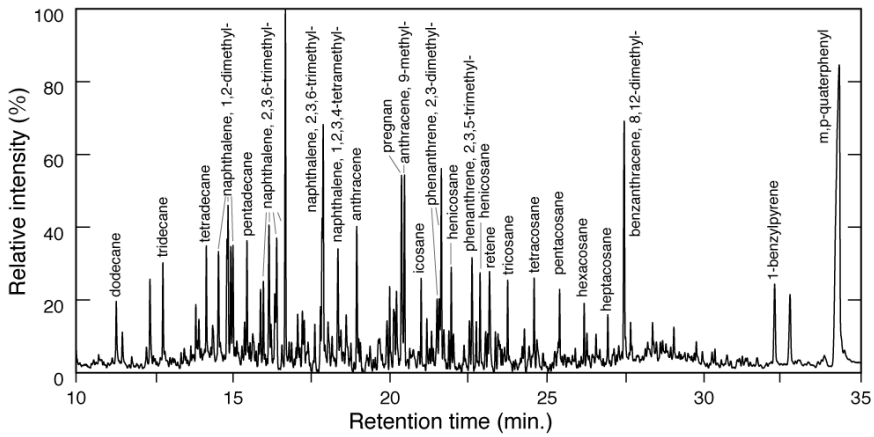

Figure 2.2. Pyrogram of the Ashibetsu bituminous coal obtained by heating a sample from 100 to 330 °C.

2.2.2. Experiments

2.2.2.1. Mixing procedure

Before the friction, milling, and heating experiments, we examined the color differences due to different initial concentrations of coal and magnetite particles. Mixed samples of 99.99 wt.% montmorillonite + 0.01 wt.% coal, 99.9 wt.% montmorillonite + 0.1 wt.% coal, 99 wt.% montmorillonite + 1 wt.% coal, 97.3 wt.% montmorillonite + 2.7 wt.% coal, 90 wt.% montmorillonite + 10 wt.% coal, 99.99 wt.% montmorillonite + 0.01 wt.% magnetite, 99.9 wt.% montmorillonite + 0.1 wt.% magnetite, 99 wt.% montmorillonite + 1 wt.% magnetite, 96.1 wt.% montmorillonite + 3.9 wt.% magnetite, 90 wt.% montmorillonite + 10 wt.% magnetite, and 69.2 wt.% montmorillonite + 30.8 wt.% magnetite were prepared (Table 2.1). The samples were manually mixed in an agate mortar.

Table 2.1. Results of color measurements of all the samples before and after the experiments.

Experiment	Status	Average*			Standard deviation*		
		L*	a*	b*	L*	a*	b*
Mixing	Montmorillonite 100 wt.%	81.330	-0.548	5.870	0.000	0.002	0.000
	Montmorillonite + coal 0.01 wt.%	82.430	-0.584	5.866	0.000	0.002	0.002
	Montmorillonite + coal 0.1 wt.%	82.026	-0.578	5.934	0.002	0.002	0.002
	Montmorillonite + coal 1 wt.%	80.732	-0.514	5.436	0.002	0.002	0.005
	Montmorillonite + coal 2.7 wt.%	80.400	-0.572	5.054	0.000	0.002	0.002
	Montmorillonite + coal 10 wt.%	71.602	-0.428	2.392	0.002	0.002	0.004
	Montmorillonite + magnetite 0.01 wt.%	82.120	-0.480	5.760	0.003	0.004	0.003
	Montmorillonite + magnetite 0.1 wt.%	81.712	-0.560	5.974	0.002	0.000	0.002
	Montmorillonite + magnetite 1 wt.%	81.176	-0.544	5.596	0.002	0.004	0.002
	Montmorillonite + magnetite 3.9 wt.%	80.172	-0.574	4.770	0.002	0.004	0.003
	Montmorillonite + magnetite 10 wt.%	76.762	-0.538	3.448	0.006	0.002	0.002
	Montmorillonite + magnetite 30.8 wt.%	66.610	0.044	1.044	0.000	0.002	0.005
Friction	Montmorillonite 100 wt.%	83.300	-0.168	4.732	0.000	0.002	0.002
	Montmorillonite + coal 0.1 wt.%	75.260	0.600	4.820	0.000	0.003	0.003
	Montmorillonite + coal 1 wt.%	64.730	0.846	4.914	0.000	0.002	0.004
Milling	Montmorillonite 100 wt.% after 1-h milling	84.438	0.102	5.230	0.002	0.002	0.003
	Montmorillonite 100 wt.% after 2-h milling	84.112	0.168	5.270	0.002	0.002	0.003
	Montmorillonite 100 wt.% after 4-h milling	82.554	0.292	5.082	0.002	0.004	0.002
	Montmorillonite 100 wt.% after 6-h milling	81.220	0.440	6.150	0.000	0.000	0.000
	Montmorillonite + coal 1 wt.% after 1-h milling	75.500	0.678	4.536	0.000	0.002	0.002
	Montmorillonite + coal 1 wt.% after 2-h milling	73.632	0.862	5.000	0.002	0.002	0.003
	Montmorillonite + coal 1 wt.% after 4-h milling	68.026	1.102	5.172	0.002	0.002	0.002
	Montmorillonite + coal 1 wt.% after 6-h milling	63.812	1.338	5.420	0.004	0.002	0.003
	Montmorillonite + magnetite 1 wt.% after 1-h milling	81.724	-0.146	3.588	0.005	0.002	0.004
	Montmorillonite + magnetite 1 wt.% after 2-h milling	81.012	-0.160	2.728	0.007	0.003	0.002
	Montmorillonite + magnetite 1 wt.% after 4-h milling	78.562	-0.110	2.594	0.002	0.000	0.002
	Montmorillonite + magnetite 1 wt.% after 6-h milling	77.114	0.010	2.996	0.002	0.003	0.002
	Montmorillonite + magnetite 3.9 wt.% after 1-h milling	77.716	-0.218	1.570	0.002	0.002	0.003
	Montmorillonite + magnetite 3.9 wt.% after 2-h milling	76.040	-0.266	0.680	0.000	0.004	0.000
	Montmorillonite + magnetite 3.9 wt.% after 4-h milling	72.946	-0.252	0.040	0.004	0.004	0.004
	Montmorillonite + magnetite 3.9 wt.% after 6-h milling	71.660	-0.180	0.012	0.007	0.003	0.002
Heating	Montmorillonite 100 wt.% after 200 °C heating	81.304	-0.374	5.514	0.002	0.002	0.004
	Montmorillonite 100 wt.% after 400 °C heating	77.128	0.120	4.598	0.002	0.003	0.002
	Montmorillonite 100 wt.% after 600 °C heating	74.248	0.116	6.288	0.002	0.002	0.002
	Montmorillonite + coal 1 wt.% after 200 °C heating	80.412	-0.362	5.022	0.002	0.002	0.002
	Montmorillonite + coal 1 wt.% after 400 °C heating	65.174	-0.614	1.464	0.002	0.004	0.005
	Montmorillonite + coal 1 wt.% after 600 °C heating	50.214	-0.134	1.736	0.002	0.002	0.002
	Montmorillonite + magnetite 1 wt.% after 200 °C heating	81.098	-0.470	5.376	0.002	0.000	0.002
	Montmorillonite + magnetite 1 wt.% after 400 °C heating	76.400	0.302	4.470	0.000	0.004	0.003
	Montmorillonite + magnetite 1 wt.% after 600 °C heating	73.250	0.094	5.136	0.000	0.002	0.002
	Montmorillonite + magnetite 3.9 wt.% after 200 °C heating	80.016	-0.366	4.690	0.040	0.002	0.009
	Montmorillonite + magnetite 3.9 wt.% after 400 °C heating	74.624	0.122	3.024	0.002	0.004	0.002
	Montmorillonite + magnetite 3.9 wt.% after 600 °C heating	72.428	0.294	5.082	0.002	0.002	0.004

*Average and standard deviation are obrained from five measurements for each sample.

2.2.2.2. Friction experiment

For the friction experiments we used a high-velocity rotary shear apparatus to examine the effects of mechanical damage and frictional heat on synthetic fault samples (Figure 2.3a). In this series of experiments, we placed approximately 500 mg of dry powdered sample, consisting of (1) montmorillonite (100 wt.%), (2) montmorillonite (99.9 wt.%) + coal (0.1 wt.%), or (3) montmorillonite (99 wt.%) + coal (1 wt.%), between the ends of two gabbro cylinders (25-mm diameter) and then sealed the cylinders within a polytetrafluoroethylene (Teflon) sleeve to prevent leaks (Figure 2.3b). Because in the Chelungpu fault example the concentration of CM in the black gouge and the surrounding rocks was reported to be approximately 0.27 ± 0.09 wt.%

(Ikehara et al., 2007), we adopted coal concentrations of 0.1 and 1 wt.% for our friction experiments. The experiments were carried out at a velocity of 1 m s^{-1} with 10 m of displacement under 1 MPa of normal stress under a dry Ar atmosphere; the resultant friction data are shown in Supporting Information Figure S2.1. The temperature distribution within the sample during the experiments was estimated by using an axisymmetric 2-D model based on the finite-element method, in which the highest temperature was approximately 330 °C (Supporting Information Figure S2.2). After the friction experiments, damaged powder from the outer 6.0–12.5 mm of the sample was collected for analysis.

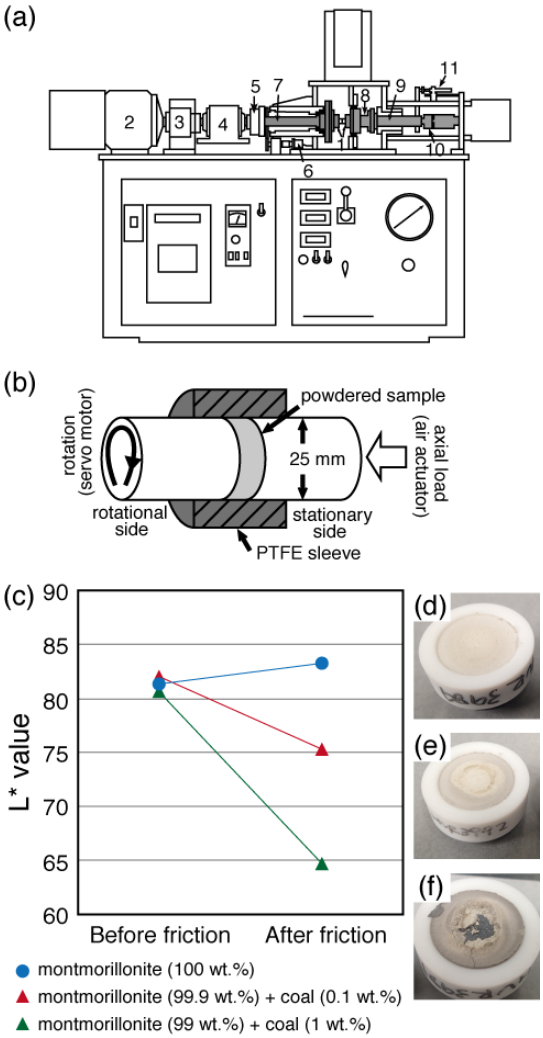

Figure 2.3. (a) Simplified sketch of the high-velocity friction testing apparatus. 1, sample holder; 2, motor; 3, torque limiter; 4, torque gauge; 5, electromagnetic clutch; 6, rotary encoder; 7, rotary column; 8, torque-axial force gauge; 9, spline; 10, axial force gauge; 11, displacement transducer. Modified from Mizoguchi et al. (2009). (b) Schematic illustration of the sample assembly. (c) Changes of the L* value before and after the friction experiment. (d–f) Photographs of samples after the friction experiment: (d) montmorillonite (100 wt.%); (e) mixture of montmorillonite 99.9 wt.% and coal 0.1 wt.%; (f) mixture of montmorillonite 99 wt.% and coal 1 wt.%.

2.2.2.3. Milling experiment

For the comminution experiments, a laboratory planetary mill (Pulverisette 6, Fritsch) was used to grind samples for 1, 2, 4, or 6 h at 600 rpm. Grinding was suspended for 5 minutes after each 20 minutes of milling to prevent the sample temperature from rising; thus, the temperature at the end of each experiment, measured by using a needle probe thermometer, was only slightly higher than room temperature (approximately 40 °C). In this series of experiments, we used (1) mixed samples of 99 wt.% montmorillonite + 1 wt.% coal, (2) 99 wt.% montmorillonite + 1 wt.% magnetite, (3) 96.1 wt.% montmorillonite + 3.9 wt.% magnetite, and (4) samples consisting only of montmorillonite (100 wt.%).

2.2.2.4. Heating experiment

For the heating experiments, we used the TG-DSC apparatus to heat (1) mixed samples of 99 wt.% montmorillonite + 1 wt.% coal, (2) 99 wt.% montmorillonite + 1 wt.% magnetite, (3) 96.1 wt.% montmorillonite + 3.9 wt.% magnetite, and (4) samples consisting only of montmorillonite (100 wt.%). Approximately 30 mg of sample was placed in a covered Pt90Rh10 crucible and heated from room temperature to a target temperature of 200, 400, or 600 °C at a rate of 20 °C min^{-1} under a flow of Ar gas (50 mL min^{-1}).

2.2.3. Color measurement

An ultraviolet-visible spectrophotometer (V-750, Jasco) was used for quantitative evaluation of the color of the samples before and after the experiments. Powdered sample material was placed in a cylindrical cell with a transparent quartz window. Because the degree of compaction of a sample can affect its color, the porosity of each sample was manually controlled to 39.7 ± 2.1%. Five spectra from each sample were acquired in the range of 800–350 nm^{-1} at a scan rate of 1000 nm min^{-1}, a spectral bandwidth of 1 nm and a spot size of 3 mm in diameter. The spectra were converted into L*a*b* color values, where L* indicates brightness

(black, L* = 0; white, L* = 100), and a* and b* are values along red–green (+a* = more reddish, –a* = more greenish) and yellow–blue (+b* = more yellowish, –b* = more bluish) axes, respectively. Because moisture absorbed by the surface of the sample could affect the color (mainly reducing the brightness value), we dried all samples at 50 °C for several hours just before the color measurements.

2.2.4. Microscopic observation

To investigate the mechanical damage that occurred during the friction and milling experiments, we observed the microstructure of mixed samples (montmorillonite 99 wt.% + coal 1 wt.% and montmorillonite 99 wt.% + magnetite 1 wt.%) after the experiments by using a field-emission scanning electron microscope (JSM-6500, JEOL) operated at an acceleration voltage of 10 or 12 kV attached with energy dispersive X-ray spectrometry (JED-2300F, JEOL). Initial montmorillonite, coal, and magnetite particles before the experiments were also observed.

2.3. Results

2.3.1. Color transitions

We first examined the initial color change in mixtures with different ratios of coal or magnetite to montmorillonite, and then, after all experiments were completed, we determined the degree of blackening of each sample from the change in its L* value. All color measurement data (L*, a*, and b*) are shown in Table 2.1, and all photo images of the samples are shown in Supporting Information Figure S2.3.

The initial L* values of mixed samples with higher weight fractions of coal or magnetite were lower (Figure 2.4a and b, respectively) than those with lower weight fractions. Comparison of L* values among mixed samples with 0.1, 1, and 10 wt.% of coal or magnetite showed that the L* values of samples containing coal were lower than samples containing the

same proportion of magnetite by weight. However, when the volume fraction of coal or magnetite relative to bulk volume, calculated from sample density and the controlled porosity, was taken into consideration, the L* values of magnetite mixtures were lower than those of the corresponding coal mixtures (Figure 2.4c: 1 wt.% coal and 3.9 wt.% magnetite correspond to 1.3 vol.%; 2.7 wt.% coal and 10 wt.% magnetite to 3.4 vol.%; and 10 wt.% coal and 30.8 wt.% magnetite to 11.6 vol.%). These values reflect the intrinsic blackness of each material.

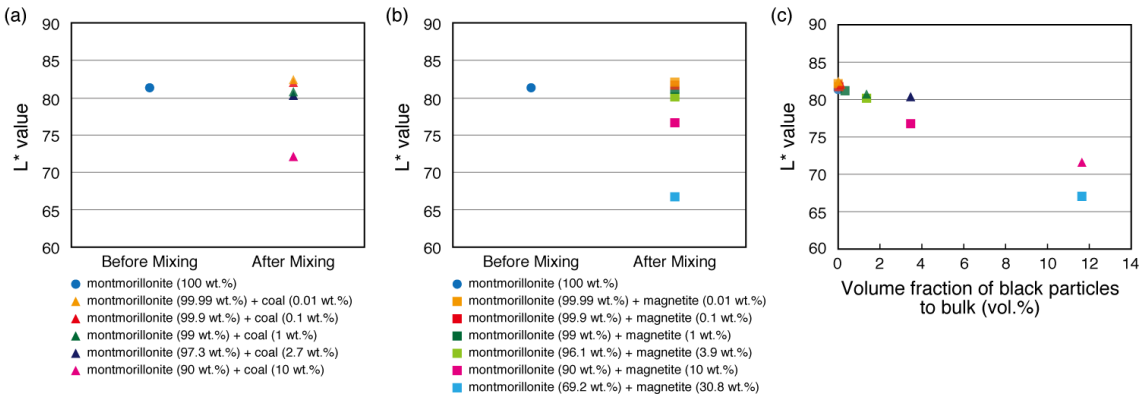

Figure 2.4. Initial L* value changes in admixtures of (a) coal and (b) magnetite particles in montmorillonite samples. (c) Relationship between L* value and the volume fraction of black particles.

After the friction experiments (Figure 2.3c), montmorillonite (100 wt.%) became slightly whiter (Figure 2.3d), but mixtures of montmorillonite and coal (0.1 or 1 wt.%) were considerably blackened (Figure 2.3e and f, respectively), and the L* value was lower when the coal content was higher.

The milling experiment results showed that the L* value of montmorillonite (100 wt.%) remained roughly constant regardless of milling time, whereas the L* value of the mixture of montmorillonite and coal (1 wt.%) decreased with milling time (Figure 2.5). L* values of mixtures of montmorillonite and magnetite (1 wt.% or 3.9 wt.%) also decreased with milling time. Although 1 wt.% coal and 3.9 wt.% magnetite mixtures have the same volume fraction to bulk (1.3 vol.%), the L* value of the former was lower than that of the latter regardless of the

milling time.

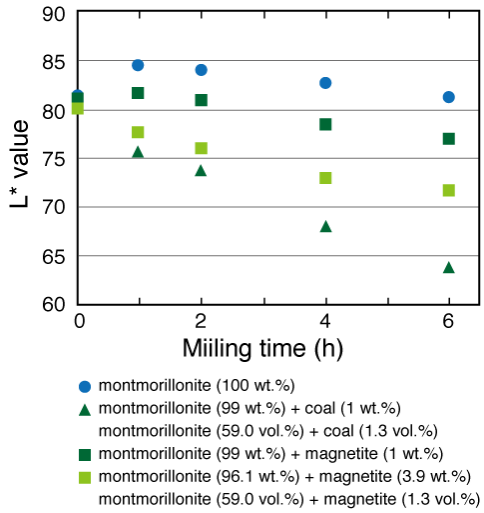

Figure 2.5. L* value changes in pure montmorillonite and mixtures of montmorillonite and coal (1 wt.%) and of montmorillonite and magnetite (1 and 3.9 wt.%) caused by milling.

In the heating experiment results, the L* value of montmorillonite (100 wt.%) decreased slightly with increases in temperature, whereas the L* values of the mixture of montmorillonite and coal (1 wt.%) were much lower at temperatures ≥ 400 °C (Figure 2.6). The L* values of mixtures of montmorillonite and magnetite (1 wt.% and 3.9 wt.%) were nearly the same as the L* value of 100 wt.% montmorillonite (Figure 2.6) at all heating temperatures.

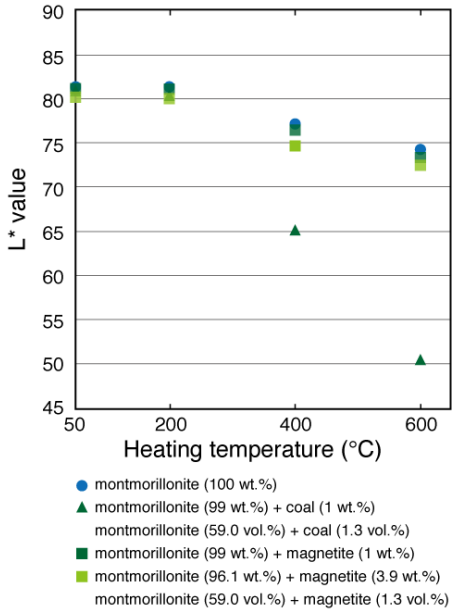

Figure 2.6. L* value changes in pure montmorillonite and mixtures of montmorillonite and coal (1 wt.%) and of montmorillonite and magnetite (1 and 3.9 wt.%) caused by heating.

The other color index values, a* and b* values, of all samples are shown in Figure 2.7. The starting mixtures were slightly greenish (negative a* value) and yellowish (positive b* value), and the values of mixtures with 10 wt.% coal and 10 and 30.8 wt.% magnetite approached zero (Figure 2.7a). In the milling experiments, the a* values of 100 wt.% montmorillonite and of the coal mixtures increased with milling time, but those of the magnetite mixtures did not show any systematic change. The b* values of 100 wt.% montmorillonite and of the coal mixtures did not show any notable change, but those of the magnetite mixtures decreased with milling time (Figure 2.7b). In the heating experiments, the a* values of 100 wt.% montmorillonite and of the magnetite mixtures increased at high temperatures, but those of the coal mixtures did not show any systematic change. The b* values of 100 wt.% montmorillonite and of the magnetite mixtures generally decreased with increasing temperature, but at 600 °C they increased (Figure 2.7c). In the friction experiments, the a* values of 100 wt.% montmorillonite and of the coal mixtures increased, and their b* values slightly decreased (Figure 2.7d). Overall, changes in the a* and b* values of the samples were not larger than those

of the L* values.

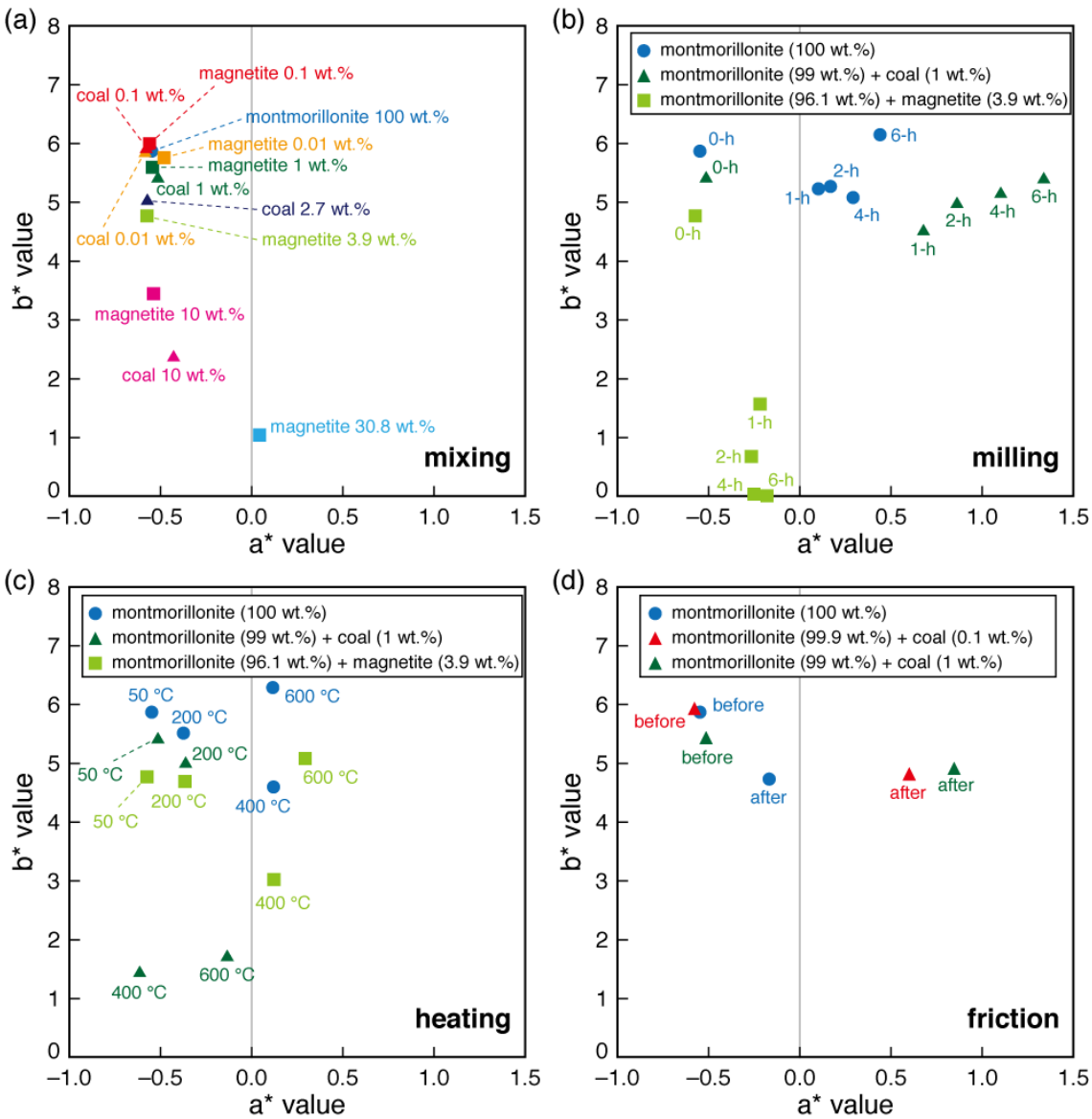

Figure 2.7. Changes of a* and b* values in pure montmorillonite, mixtures of montmorillonite and coal, and mixtures of montmorillonite and magnetite after (a) mixing and after (b) milling, (c) heating, and (d) friction experiments.

2.3.2. Microstructures

Scanning electron microscope images of the montmorillonite and coal used for the

experiments (Figure 2.8a and b, respectively) show that initially the grains were approximately 10–100 μm in diameter. After the milling experiments, the mixture of montmorillonite and coal (1 wt.%) showed a drastic reduction of particle size (Figure 2.8c–f), and the damaged samples included large amounts of ultrafine particles, from submicrometer-sized particles to ones several tens of nanometers in size, with well-rounded spheroidal shapes (Figure 2.8d–f). Aggregations of ultrafine particles were also observed in the damaged samples. However, after the friction experiment, the samples included only small amounts of such ultrafine particles (Figure 2.8g), apparently similar to the amount in samples after a milling time of 2 h (Figure 2.8d).

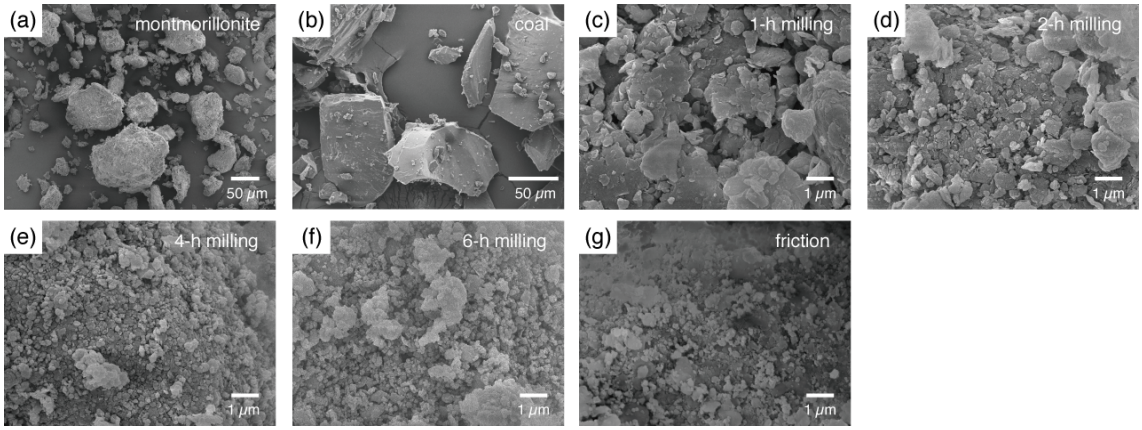

Figure 2.8. Scanning electron microscopy images of the starting samples of (a) montmorillonite and (b) coal and of mixtures of montmorillonite 99 wt.% and coal 1 wt.% after milling for (c) 1, (d) 2, (e) 4, and (f) 6 h; and (g) after the friction experiment.

Scanning electron microscope images of the magnetite used for the experiments show that initially the grains were approximately 10–200 μm in diameter (Figure 2.9a). After the milling experiments, the mixed samples of montmorillonite and magnetite (1 wt.%) also showed a drastic reduction of particle size and the development of aggregations of ultrafine particles (Figure 2.9b–e).

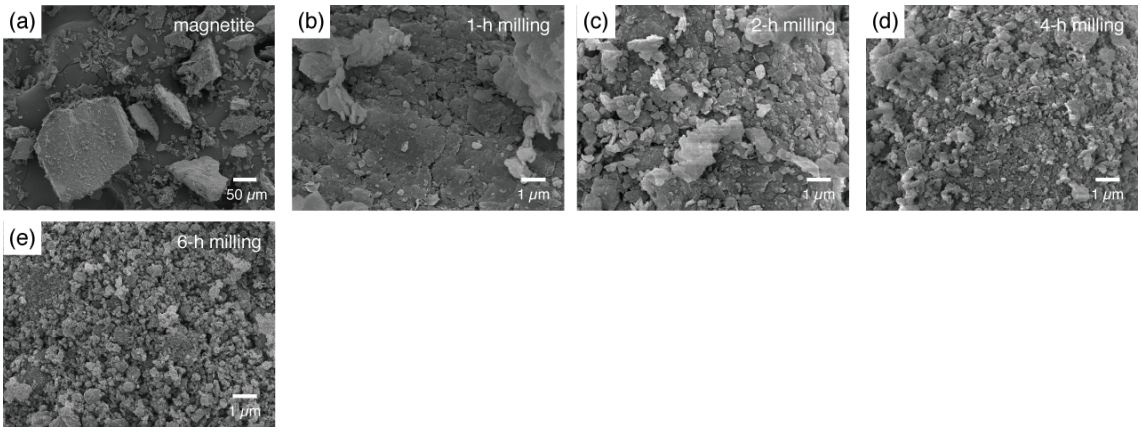

Figure 2.9. Scanning electron microscopy images (a) of the starting sample of magnetite and of mixtures of montmorillonite 99 wt.% and magnetite 1 wt.% after milling for (b) 1, (c) 2, (d) 4, and (e) 6 h.

The chemical compositions of particles (or particle aggregations) from the montmorillonite and coal (1 wt.%) or montmorillonite and magnetite (1 wt.%) mixtures after 1 or 6 h of milling are shown in Figure 2.10. Although the volume fraction of coal in the mixed sample (1.3 vol.%) was higher than the volume fraction of magnetite in the mixed sample (0.3 vol.%), after milling, no coal particles (zero intensity for carbon) were detected by energy dispersive X-ray spectrometry (Figure 2.10a–d). In contrast, magnetite particles (Fe peak) were detected, although only in the sample after 1 h of milling (Figure 2.10e and f).

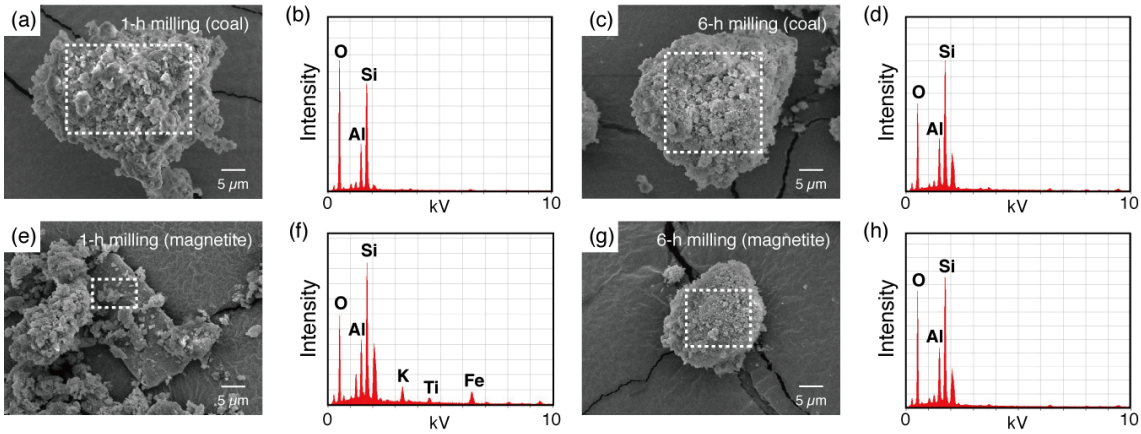

Figure 2.10. Micro-scale chemical compositions of experimental samples analyzed by energy dispersive X-ray spectrometry: Mixture of montmorillonite 99 wt.% and coal 1 wt.% after milling for (a, b) 1 and (c, d) 6 h; mixture of montmorillonite 99 wt.% and magnetite 1 wt.% after milling for (e, f) 1 and (g, h) 6 h. The area within the dotted rectangle in each scanning electron microscopy image (left column) corresponds to the analyzed area. The corresponding X-ray spectra are shown on the right.

2.4. Discussion and conclusions

The main question that we address here is the blackening effect of each experimental treatment. The initial mixed samples (montmorillonite + coal or magnetite) became blacker as the volume fraction of coal or magnetite was increased, and the magnetite mixtures were blacker than the coal mixtures, owing to differences in the intrinsic blackness of coal and magnetite.

The milling experiment reproduced the comminution and granulation that occurs during earthquake slip. Mixtures of coal or magnetite became blacker with longer milling times. Considerable numbers of fine particles (<1 μm) were observed in the samples after long milling times (Figure 2.8c–f and Figure 2.9b–e), but particles of coal could not be identified by energy dispersive X-ray spectrometry after milling, whereas particles of magnetite could be identified after 1 h of milling but not after 6 h (Figure 2.10), thus indicating that the coal and magnetite

particles were intensely comminuted and dispersed in the samples. Although the volume fractions relative to bulk (1.3 vol.%) of the mixtures of coal (1 wt.%) and magnetite (3.9 wt.%) were the same, the coal mixture was blacker than the magnetite mixture, probably owing to the relatively wider dispersion of finer coal particles, which are not as hard as magnetite particles (Mohs hardness: coal, 2.5; magnetite, 6; Hauserman, 1985).

The heating experiment reproduced the frictional heating during earthquake slip. The large decrease of the L* value of only coal mixtures at temperatures above 400 °C may reflect pyrolysis of the coal, because the TG curve of the intact coal sample showed that pyrolysis occurred around that temperature (Figure 2.1), releasing gases composed mainly of naphthalene and normal chain aliphatic hydrocarbons (Figure 2.2). These gaseous organics could adsorb onto the surfaces of the montmorillonite particles, because selective adsorption of organic gas onto clay minerals has been reported (e.g., Volzone et al., 1999; Cheng & Huang, 2004; Breus et al., 2008; Heller & Zoback, 2014). In addition, comminution induces not only wearing, breakage, and distortion of materials but also increases the surface area and causes chemical activation (e.g., Hirono et al., 2013). Such mechanochemically activated surfaces of clay minerals generally have high adsorptive capacity (e.g., Lapides et al., 2002). Thus, adsorption likely occurred during our heating experiments.

In friction experiments, the samples were both comminuted and heated, so after the experiments the mixed samples presumably exhibited the effects of both together. The highest temperature experienced during these experiments was estimated to be approximately 330 °C (Supporting Information Figure S2.2), which might not be high enough for high progress of pyrolysis of the coal and decrease the L* value (Figure 2.1 and 2.6, respectively). However, comminuted coal has more mechanochemically activated reactivity than intact coal particles, and pyrolysis of damaged coal, accompanied by the release of relatively large amounts of organic gases, can progress intensely at such low temperature (Zhang et al., 2007); thus, some organic gas could have been released by the mixed samples during the friction experiment. In fact, the microstructure of the mixed sample after the friction experiment resembled that of a mixed sample after a milling time of 2 h; moreover, the L* value of the former (64.730) was

considerably lower than L* value of the latter (73.632). These results suggest that both pyrolysis and adsorption occurred in the sample during the friction experiment. Therefore, the blackening observed after the friction experiment could have resulted from both comminution and pyrolysis effects; that is, fine coal particles became widely dispersed in the sample, and montmorillonite particles adsorbed organic gases produced by pyrolysis of the coal particles. Although Tanikawa et al. (2008), who conducted similar friction experiments, concluded that magnetic minerals dominantly control the blackening of fault-rock samples from the Chelungpu fault, we believe that the amount of magnetic minerals in the samples was too small (<1 wt.%) to account for the blackening (see Figure 2.4b and 2.5).

After the friction and milling experiments, samples of 100 wt.% montmorillonite showed slight increases of L* values (Figure 2.3c and 2.5), possibly caused by roughness of the particle surface. Not all incident light is reflected by a powdered sample because surface irregularities (roughness) cause diffuse reflection (e.g., Christidis et al., 2004). The slight decreases of the L* value at high temperatures (>400 °C) in the 100 wt.% montmorillonite sample might be related to changes in the intercrystalline structure, because dehydroxylation occurs at such temperatures (e.g., Malek et al., 1997).

Our experiments, which were carried out on synthetic mixtures of montmorillonite and bituminous coal and of montmorillonite and magnetite (Figure 2.11a), revealed that highly comminuted fine black particles were widely dispersed, and the surface area of black particles was probably also increased (Figure 2.11b). Such granulation is a characteristic feature of fault zones (e.g., Ben-Zion & Sammis, 2003), and the particles in fault gouge sometimes show a power law size distribution (Sammis et al., 1986). The presence of ultrafine particles, smaller than 10 nm, might also place constraints on the dynamic fields of the fault zone during a large earthquake (Sammis & Ben-Zion, 2008). In addition, a localized black slip zone composed of densely packed submicrometer-sized particles was produced in Pennsylvania slate and Rochester shale samples by friction generated at a low slip rate (~10–5 m s^{-1}) (Ikari, 2015). Although Ikari (2015) did not report the concentration of CMs in the samples, slate and shale generally contain CMs such as vitrinite and inertinite; thus, dispersal of finely comminuted CMs

might have caused the blackening during their experiments. Taking into consideration the fact that comminution always occurs during earthquake slip, whether slow or fast, fault rock containing merely 1.3 vol.% of CM or black minerals (not only magnetite but also other black minerals such as biotite and amphibole) might become blackened as a result of the wide dispersal of fine particles of these materials in the fault gouge. However, our results showed that mixtures of montmorillonite and coal were greatly blackened at high temperature (Figure 2.11d), whereas those of montmorillonite and magnetite were not (Figure 2.11c). Therefore, the frictional heating that occurs during slip might induce drastic blackening through the pyrolysis of CM and the adsorption of the resulting gases onto clay mineral particles. Thus, not only the dispersal of fine black particles but also the adsorption of organic gases produced by pyrolysis might intensify the blackening of bulk samples during earthquake slip (Figure 2.11e). This blackening process in a fault zone may be recognizable geological evidence for an earthquake slip, especially along faults developed in sedimentary rocks (which typically include CM).

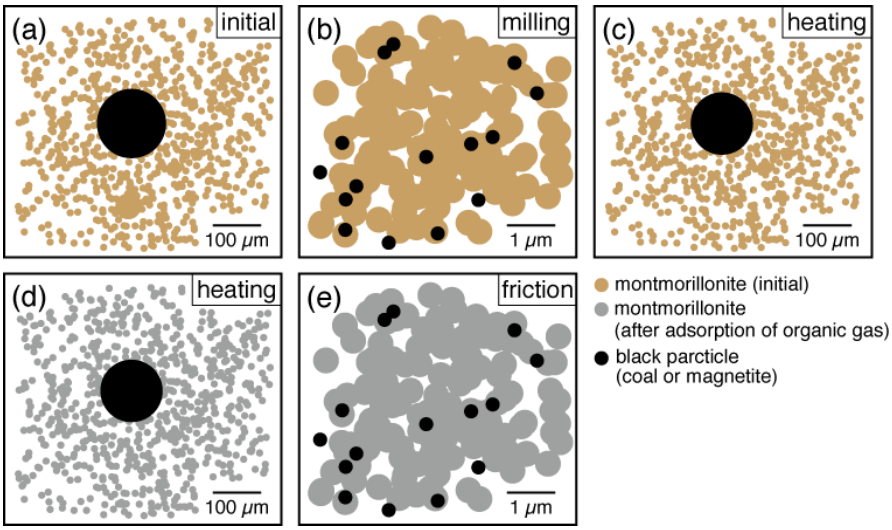

Figure 2.11. Schematic diagrams of particle sizes and distributions and color changes due to adsorption of organic gases onto montmorillonite particles. (a) Initial state of a mixture of montmorillonite and coal particles. (b) Mixture of montmorillonite and coal or magnetite particles after milling. (c) Mixture of montmorillonite and magnetite after heating. (d) Mixture of montmorillonite and coal after heating. (e) Mixture of montmorillonite and coal after the friction experiment.

Other black rocks that occur in fault zones are (1) pseudotachylyte, which is usually glassy and black, similar to obsidian in appearance, owing to the presence of iron and magnesium impurities (e.g., Petrik et al., 2003); (2) fault gouge and cataclasite developed in pelitic schist, such as in the Anko outcrop along the Median Tectonic Line, Japan (Jefferies et al., 2006); and (3) graphite-rich rocks, in which graphite is formed from gas-phase methane produced by the reaction of carbonate minerals with hydrogen under reducing conditions (Oohashi et al., 2014). In the second and third of these cases, the cause might be the mixing of black materials as demonstrated in our experiments. The alteration of minerals such as feldspar and clay minerals is often observed in fault gouges (e.g., Arancibia et al., 2014), but because CMs seldom undergo such secondary transformation, the record of blackening due to CMs should be preserved over a long geological period.

For quantitative evaluation of the degree of blackening (change of the L* value) related to slip parameters, more advanced friction experiments performed under various conditions are required. In addition, the kinetics of the pyrolysis reaction must be evaluated to determine whether the reaction can progress during a short rise time. Thus, more analyses of materials of various types, integrated with laboratory experiments and kinetic evaluations, are required to account for the physicochemical and thermomechanical processes and reactions that occur in a slip zone to improve our understanding of fault zone blackening during earthquake slip.

References

Arancibia, G., Fujita, K., Hoshino, K., Mitchell, T.M., Cembrano, J., Gomila, R., Morata, D., Faulkner, D.R. & Rempe, M. (2014). Hydrothermal alteration in an exhumed crustal fault zone: Testing geochemical mobility in the Caleta Coloso Fault, Atacama Fault System, Northern Chile. *Tectonophysics* **623**, 147–168.

Balsamo, F., Aldega, L., De Paola, N., Faoro, I. & Storti, F. (2014). The signature and mechanics of earthquake ruptures along shallow creeping faults in poorly lithified sediments. *Geology* **42**, 435–438.

Ben-Zion, Y. & Sammis, C.G. (2003). Characterization of fault zones. *Pure Appl. Geophys.* **160**, 677–715.

Breus, I., Denisova, A. & Nekljudov, S. (2008). Adsorption of volatile hydrocarbons on natural zeolite-clay material. *Adsorption* **14**, 509–523.

Buatier, M.D., Chauvet, A., Kanitpanyacharoen, W., Wenk, H.R., Ritz, J.F. & Jolivet, M. (2012). Origin and behavior of clay minerals in the Bogd fault gouge, Mongolia. *J. Struct. Geol.* **34**, 77–90.

Cheng, A.-L. & Huang, W.-L. (2004). Selective adsorption of hydrocarbon gases on clays and organic matter. *Org. Geochem.* **35**, 413–423.

Chou, Y.-M., Song, S-R., Aubourg, C., Lee, T-Q., Boullier, A.-M., Song, Y.-F., Yeh, E.-C., Kuo, L.-W. & Wang, C.-Y. (2012). An earthquake slip zone is a magnetic recorder, *Geology* **40**, 551–554.

Christidis, G.E., Makri, P. & Perdikatsis, V. (2004). Influence of grinding on the structure and colour properties of talc, bentonite and calcite white fillers. *Clay Minerals* **39**, 163–175.

Han, R., Shimamoto, T., Hirose, T., Ree, J.-H. & Ando, J. (2007). Ultralow friction of carbonate faults caused by thermal decomposition. *Science* **316**, 878–881.

Hauserman, W. B. (1985). Hardness of fine ground coals and mineral residues to predict slurry erosion. *Powder Tech.* **43**, 75–87.

Heller, R. & Zoback, M. (2014). Adsorption of methane and carbon dioxide on gas shale and pure mineral samples. *J. Unconvent. Oil Gas Resources* **8**, 14–24.

Hirono, T. *et al*. (2006). High magnetic susceptibility of fault gouge within Taiwan Chelungpu fault: Nondestructive continuous measurements of physical and chemical properties in fault rocks recovered from Hole B, TCDP. *Geophys. Res. Lett.* **33**, L15303.

Hirono, T. *et al*. (2007a). Nondestructive continuous physical property measurements of core samples recovered from hole B, Taiwan Chelungpu-Fault Drilling Project. *J. Geophys. Res.* **112**, B07404.

Hirono, T. *et al*. (2007b). A chemical kinetic approach to estimate dynamic shear stress during the 1999 Taiwan Chi-Chi earthquake. *Geophys. Res. Lett.* **34**, L19308 (Correction,

Geophys. Res. Lett. **35**, 2008).

Hirono, T. *et al*. (2008). Clay mineral reactions caused by frictional heating during an earthquake: An example from the Taiwan Chelungpu fault. *Geophys. Res. Lett.* **35**, L16303.

Hirono, T., Tanikawa, W., Honda, G., Kameda, J., Fukuda, J. & Ishikawa, T. (2013). Importance of mechanochemical effects on fault slip behavior during earthquakes. *Geophys. Res. Lett.* **40**, 2988–2992.

Hirono, T., Kameda, J., Kanda, H., Tanikawa, W. & Ishikawa, T. (2014). Mineral assemblage anomalies in the slip zone of the 1999 Taiwan Chi-Chi earthquake: Ultrafine particles preserved only in the latest slip zone. *Geophys. Res. Lett.* **41**, 3052–3059.

Hirono, T., Maekawa, Y. & Yabuta, H. (2015). Investigation of the records of earthquake slip in carbonaceous materials from the Taiwan Chelungpu fault by means of infrared and Raman spectroscopies. *Geochem. Geophys. Geosyst.* **16**, 1233–1253.

Holmboe, M., Wold, S. & Jonsson, M. (2012). Porosity investigation of compacted bentonite using XRD profile modeling. *J. Contaminant Hydrol.* **128**, 19–32.

Ikari, J. M. (2015). Principal slip zones: Precursors but not recorders of earthquake slip. *Geology* **43**, 955–958.

Ikehara, M. *et al*. (2007). Low total and inorganic carbon contents within the Chelungpu fault. *Geochem. J.* **41**, 391–396.

Ishikawa, T. *et al*. (2008). Coseismic fluid–rock interactions at high temperatures in the Chelungpu fault. *Nat. Geosci.* **1**, 679–683.

Jefferies, S.P., Holdsworth, R.E., Shimamoto, T., Takagi, H., Lloyd, G.E. & Spiers, C.J. (2006). Origin and mechanical significance of foliated cataclastic rocks in the cores of crustal-scale faults: Examples from the Median Tectonic Line, Japan. *J. Geophys. Res.* **111**, B12303.

Lapides, I., Yariv, S. & Goldnitsky, D. (2002). Simultaneous DTA-TG study of montmorillonite mechanochemically treated with crystal-violet. *J. Therm. Analy. Calorim.* **67**, 99–112.

Maekawa, Y., Hirono, T., Yabuta, H., Mukoyoshi, H., Kitamura, M., Ikehara, M., Tanikawa, W.

& Ishikawa, T. (2014). Estimation of slip parameters associated with frictional heating during the 1999 Taiwan Chi-Chi earthquake by vitrinite reflectance geothermometry. *Earth Planets Space* **66**, 28.

Malek, Z., Balek, V., Shweky, D.G. & Yariv, S. (1997). The study of the dehydration and dehydroxylation of smectites by emanation thermal analysis. *J. Therm. Analy.* **48**, 83–92.

Manatschal, G. (1999). Fluid- and reaction-assisted low-angle normal faulting: evidence from rift-related brittle fault rocks in the Alps (Err Nappe, eastern Switzerland). *J. Struct. Geol.* **21**, 777–793.

Meyers, R. A. (1982). *Coal Structure*. Academic Press, New York.

Mishima, T., Hirono, T., Nakamura, N., Tanikawa, W., Soh, W. & Song, S.-R. (2009). Changes to magnetic minerals caused by frictional heating during the 1999 Taiwan Chi-Chi earthquake. *Earth Planets Space* **61**, 797–801.

Mizoguchi, K., Hirose, T., Shimamoto, T. & Fukuyama, E. (2009). High-velocity frictional behavior and microstructure evolution of fault gouge obtained from Nojima fault, southwest Japan. *Tectonophysics* **471**, 285–296.

O'Hara, K., Mizoguchi, K., Shimamoto, T. & Hower, J. C. (2006). Experimental frictional heating of coal gouge at seismic slip rates: Evidence for devolatilization and thermal pressurization of gouge fluids. *Tectonophysics* **424**, 109–118.

Oohashi, K., Han, R., Hirose, T., Shimamoto, T., Omura, K. & Matsuda, T. (2014). Carbon-forming reactions under a reducing atmosphere during seismic fault slip. *Geology* **42**, 787–790.

Petrik, I., Nabelek, P.I., Janak, M. & Plasienka, D. (2003). Conditions of formation and crystallization kinetics of highly oxidized pseudotachylytes from the high Tatras (Slovakia). *J. Petrol.* **44**, 901–927.

Sakaguchi, A., Yanagihara, A., Ujiie, K., Tanaka, H. & Kameyama, M. (2007). Thermal maturity of a fold–thrust belt based on vitrinite reflectance analysis in the Western Foothills complex, western Taiwan. *Tectonophysics* **443**, 220–232.

Sammis, C.G. & Ben-Zion, Y. (2008). Mechanics of grain-size reduction in fault zones. *J. Geophys. Res.* **113**, B02306.

Sammis, C.G., Osborne, R.H., Anderson, J.L., Banerdt, M. & White, P. (1986). Self-similar cataclasis in the formation of fault gouge. *Pure Appl. Geophys.* **124**, 53–78.

Schön, J. H. (1996). *Physical Properties of Rocks: Fundamentals and Principles of Petrophysics.* Elsevier, Amsterdam.

Tanikawa, W., Mishima, T., Hirono, T., Soh, W. & Song, S.-R. (2008). High magnetic susceptibility produced by thermal decomposition of core samples from the Chelungpu fault in Taiwan. *Earth Planet. Sci. Lett.* **272**, 372–381.

Tsutsumi, A., Nishino, S., Mizoguchi, K., Hirose, T., Uehara, S., Sato, K., Tanikawa, W. & Shimamoto, T. (2004). Principal fault zone width and permeability of the active Neodani fault, Nobi fault system, Southwest Japan. *Tectonophysics* **379**, 93–108.

Volzone, C., Thompson, J.G., Melntchenko, A., Ortiga, J. & Palethorpe, S.R. (1999). Selective gas adsorption by amorphous clay-mineral derivatives. *Clays Clay Minerals* **47**, 647–657.

Yao, L., Ma, S., Shimamoto, T. & Togo, T. (2013). Structures and high-velocity frictional properties of the Pingxi fault zone in the Longmenshan fault system, Sichuan, China, activated during the 2008 Wenchuan earthquake. *Tectonophysics* **599**, 135–156.

Zhang, C., Jiang, X., Wei, L. & Wang, H. (2007). Research on pyrolysis characteristics and kinetics of super fine and conventional pulverized coal. *Energy Conv. Manage.* **48**, 797–802.

Supporting information

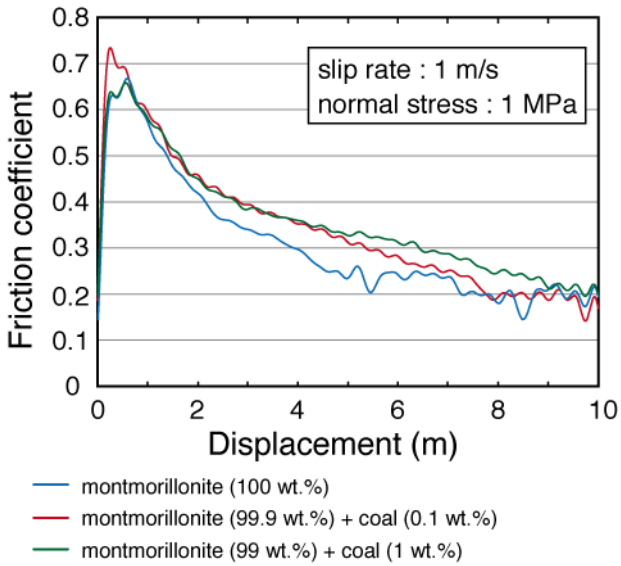

Figure S2.1. Changes in the friction coefficient with slip displacement.

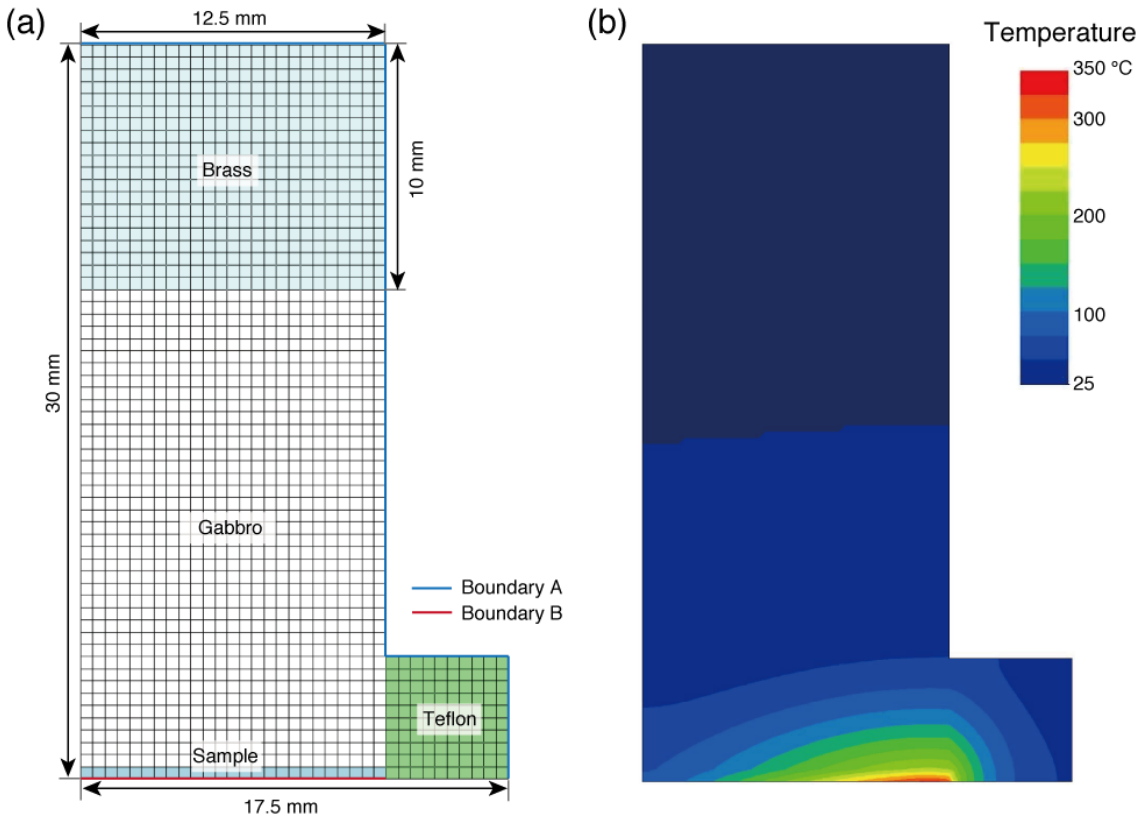

Figure S2.2. Temperature modeling during the friction experiment. (a) Sample column geometry used for calculation of the temperature distribution during the friction experiment. The specific heat capacities, thermal conductivities, and densities of brass, gabbro, Teflon, and sample used for the calculation are as follows: 385, 1000, 1000, and 1100 J kg^{-1} K^{-1}, respectively; 60, 3, 0.25, and 1.13 W m^{-1} K^{-1}, respectively; 8710, 2950, 220, and 2570 kg m^{-3}, respectively. (b) The calculated temperature distribution when the sample reached to maximum temperature.

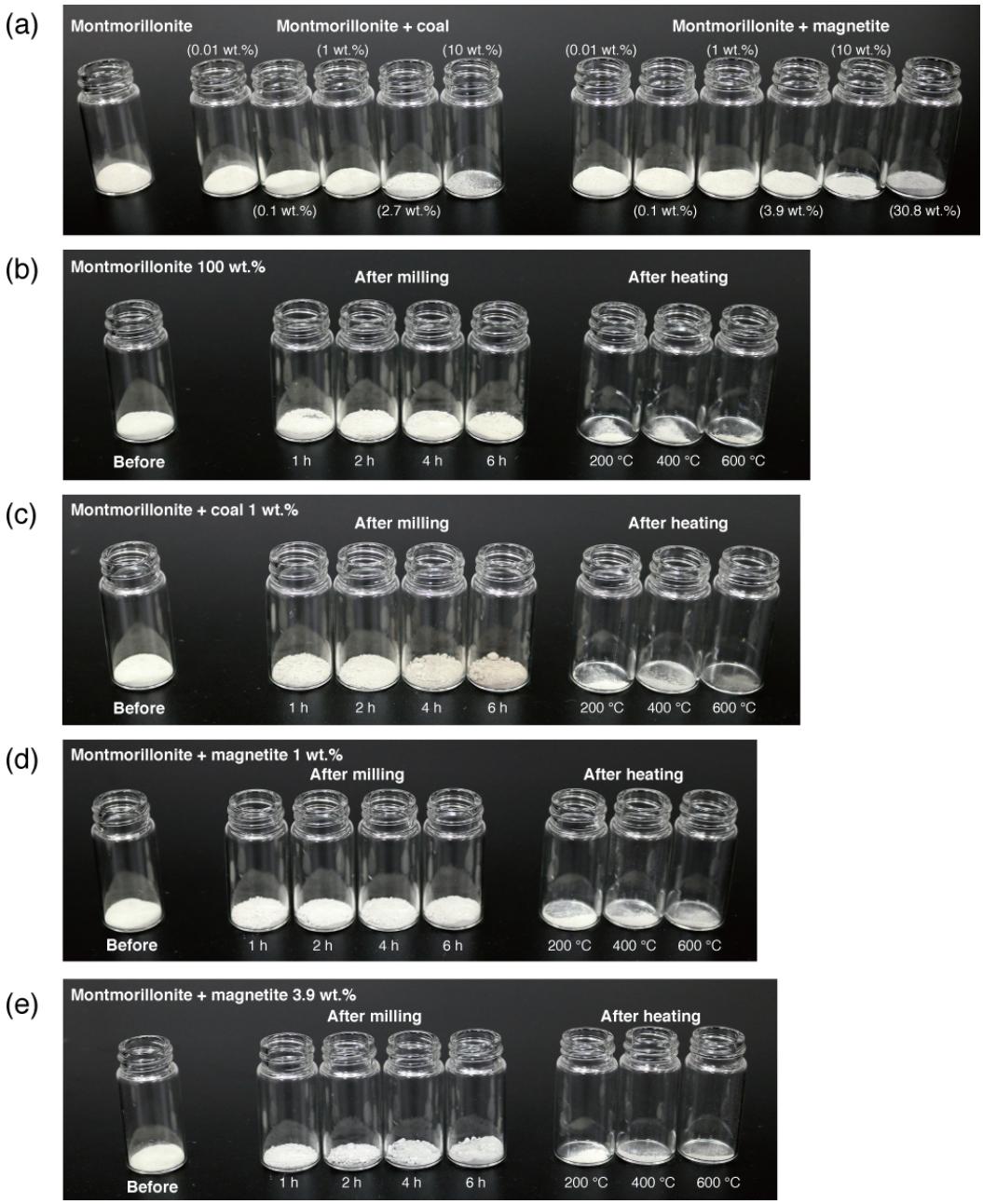

Figure S2.3. Photographs of all the samples before and after the experiments. (a) Pure montmorillonite and mixtures of montmorillonite and coal and of montmorillonite and magnetite. (b) Pure montmorillonite before and after milling and heating experiment. (c) Mixtures of montmorillonite and coal 1 wt.% before and after milling and heating experiment. (d) Mixtures of montmorillonite and magnetite 1 wt.% before and after milling and heating experiment. (e) Mixtures of montmorillonite and magnetite 3.9 wt.% before and after milling and heating experiment.

Chapter 3

Organochemical characteristics of carbonaceous materials as indicators of heat recorded on an ancient plate-subduction fault

Reprinted from *Geochemistry, Geophysics, Geosystems* **17**, 2855–2868. Kaneki, S., Hirono, T., Mukoyoshi, H., Sampei, Y. & Ikehara, M. (2016). Organochemical characteristics of carbonaceous materials as indicators of heat recorded on an ancient plate-subduction fault, with permission from John Wiley and Sons.

Abstract

Coseismic shear stress and slip distance affect subduction-related earthquake processes. They need to be understood to evaluate the earthquake's mechanism, and the tsunami generation potential near trenches. The amount of frictional heat generated depends on the shear stress and slip distance, which are therefore able to be derived from the temperature recorded in the fault. Here we developed a new temperature proxy for carbonaceous materials (CMs) by performing spectroscopic, thermogravimetric, and organic elemental analyses in conjunction with heating experiments. We found marked anomalies in the infrared (IR) and Raman spectra and atomic compositions of CMs retrieved from the slip zone of an ancient megasplay fault in the Cretaceous Shimanto accretionary complex, Japan: the IR spectra show extinction of aliphatic C–H bonding and very weak aromatic C=C bonding, and the Raman spectra show a slightly elevated ratio of disordered band intensity to graphitic band intensity and relatively low H/O and O/C ratios. These correlate well with the spectral features of host-rock CMs after heating to 600 °C. Thus, we conclude that the slip zone experienced a temperature of 600 °C during a past earthquake event, indicating coseismic slip of 2–9 m, which could have generated a large tsunami if the ruptures propagated to the seafloor.

3.1. Introduction

The largest earthquakes are usually generated in plate subduction zones, where most of the world's seismic moment release occurs (Scholz, 2002). The complicated tectonic structure of subduction zones includes the plate-boundary megathrust and décollement, frontal thrusts, and megasplay faults, which branch from the deep portion of the megathrust. Such structural features have been observed globally, including along the Nankai Trough (Tsuji et al., 2015), in Alaska (Plafker, 1972), along the Sunda margin (Kopp & Kukowski, 2003), and off Colombia (Collot et al., 2004). Importantly, not only the plate-boundary fault but also megasplay faults have the potential to trigger a gigantic tsunami if the rupture propagates to the seafloor (Park et al., 2002; Moore et al., 2007). To understand the mechanism of great subduction earthquakes,

geological studies of ancient seismogenic subduction faults exhumed in onland accretionary complexes such as the Shimanto and Alaska accretionary complexes have succeeded in providing important information about the characteristics of fault-zone materials (e.g. Rowe et al., 2009; Honda et al., 2011).

The maximum temperature recorded in the fault rock is key information for estimating the slip parameters during an earthquake, because the amount of heat produced by slip is directly related to shear stress and slip distance. Laboratory experiments and chemical kinetic evaluations, as reviewed by Rowe & Griffith (2015), have identified several proxies sensitive to frictional heat and coseismic slip. For example, thermal decomposition of carbonate minerals has been detected in both synthetic fault rocks produced by high-speed (on the order of a meter per second) friction experiments (Han et al., 2007) and natural fault gouges (Hirono et al., 2007), and the progress of dehydroxylation reactions of clay minerals during and after an earthquake has been determined by a kinetic evaluation (Hirono et al., 2008). However, some uncertainties are associated with the use of these reactions to estimate frictional heat because the actual reacted fraction due to earthquake slip is obscured by the reversibility of reactions through dissolution and recrystallization. Nonreversible proxies, such as the formation of magnetite by thermal decomposition of paramagnetic minerals and anomalies in the concentrations of fluid-mobile trace elements (Sr, Cs, Rb, and Li) and in Sr isotope ratios, have been applied to fault gouge from the Taiwan Chelungpu fault, which slipped during the 1999 Chi-Chi earthquake (Ishikawa et al., 2008; Mishima et al., 2009), but their utility is limited because they can only constrain the experienced temperature to ≥400 °C and ≥350 °C, respectively.

Therefore, we have studied nonreversible reactions of carbonaceous materials (CMs; insoluble organic matter) in relation to temperature, evaluating their potential as proxies for the heat record experienced by fault rocks during earthquake slip. Thermal maturation of organic materials has often been investigated to evaluate the temperature history associated with the burial of sedimentary rocks. In addition, vitrinite reflectance is a widely used geothermometer not only for burial processes occurring on a geological timescale (e.g., Underwood et al., 1993), but also for rapid heating due to frictional slip with a duration on the order of several tens of

seconds (e.g., Kitamura et al., 2012; Maekawa et al., 2014; Furuichi et al., 2015). Although Kitamura et al. (2012) suggested that, in addition to temperature, shear strain during high-velocity friction can affect reflectance changes of CMs, as had been indicated previously (e.g., Ross & Bustin, 1990; Wilks et al., 1993; Bustin et al., 1995), recent high-velocity friction experiments have shown that shear strain does not greatly enhance the maturation of CMs (Furuichi et al., 2015; Hirono et al., 2015). Therefore, we did not consider the effect of shear strain on the maturation of CMs in this study. Hirono et al. (2015) recently used Raman and infrared (IR) spectroscopy to examine the organochemical characteristics of CMs both in samples from the Chelungpu fault, Taiwan, and in products obtained by performing heating and friction experiments on host-rock samples. They detected marked anomalies in the Raman and IR spectra of the slip zone samples, and by comparing those anomalies with anomalies in the experimental products, they succeeded in estimating the temperature and slip parameters of the 1999 Chi-Chi earthquake.

In this study, we have examined the organochemical characteristics of CMs retrieved from an out-of-sequence thrust (OST) adjacent to the Kure Mélange (hereafter, the Kure OST) in the Shimanto accretionary complex. The Kure OST is considered to be an excellent analogue of megasplay faults observed at present in the Nankai subduction zone (Mukoyoshi et al., 2006). We used the results of multiple analyses, including Raman and IR spectroscopy, organic elemental analysis, pyrolysis–gas chromatography–mass spectrometry (py-CG/MS), and thermogravimetry (TG)–differential scanning calorimetry (DSC), in conjunction with heating experiments to estimate the maximum temperature experienced by the fault rock and the fault slip parameters. Then, from these estimates, we inferred the slip behavior that could explain them and, thus, the fault's tsunamigenic potential.

3.2. Materials and methods

3.2.1. Geological background

Several OSTs are developed in and around the Cretaceous Nonokawa Formation and the

Kure Mélange in the Shimanto accretionary complex, southwest Japan (Figure 3.1a). The deformed zone (~500 mm thick) of a representative OST exhibits several structural components: an outer fracture-damaged zone, cataclasite, and a narrow, black shear-localized slip zone 0.5–10 mm thick (Figure 3.1b). The formation depth of the slip zone has been estimated from vitrinite reflectance data to be 2.5–5.5 km (Mukoyoshi et al., 2006). The slip zone is composed of ultracataclasite and an opaque black material that under the microscope can be seen to contain microlites, vesicles, and plagioclase and K-feldspar embayment structures; thus, it is composed partly of a former friction melt, or pseudotachylyte (Mukoyoshi et al., 2006). The hanging wall and footwall are composed of greenish shale and sandstone of the Nonokawa Formation, respectively. Honda et al. (2011) reported geochemical evidence that frictional heating in the slip zone was ≥350 °C, but the upper limit of the temperature experienced could not be constrained by the method/analyses they used.

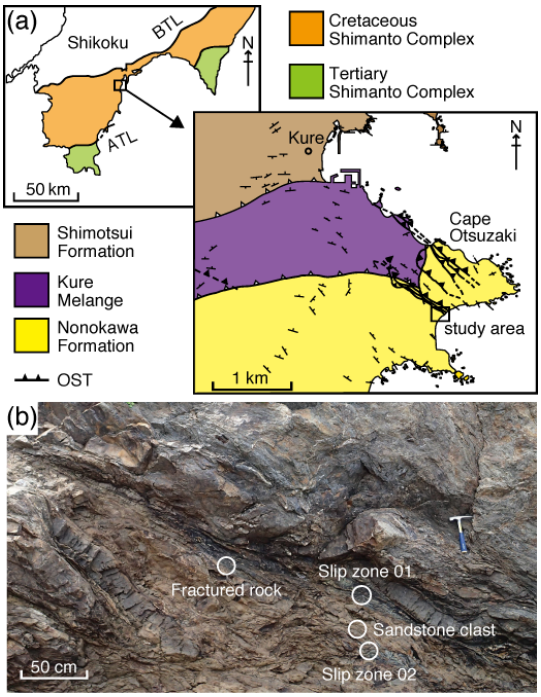

Figure 3.1. (a) Index map and simplified structural map of the area around the Kure OSTs, modified from Honda et al. (2011). ATL, Aki Tectonic Line; BTL, Butuzo Tectonic Line. (b) Photograph of the deformed zone of a representative OST showing the sampling points of our study. The host rock is not shown in this photograph.

We collected five samples from the slip zone and the surrounding deformed and host rocks from which to extract CMs for analysis of their organochemical characteristics (Figure 3.1b); two samples (SZ01 and SZ02) were collected from the slip zone, one from the fracture-damaged zone, one from a lenticular sandstone clast within the deformed zone, and one from the footwall host rock. The collected slip-zone samples were bulk samples, so they were not representative of small areas within the slip zone.

3.2.2. Extraction of CMs

CMs in the rock samples were extracted by the following HCl-HF method. The rock samples were first treated with 6 N HCl for a few days to remove metals, sulfides, and carbonates. The treated samples were allowed to settle for one day, and then the supernatant liquid was removed, and the precipitates were rinsed with distilled water several times. Next, the precipitates were treated with 27 N HF for several days to remove silicates, and then again with 6 N HCl to remove fluoride by-products. The final solid residues, corresponding to the insoluble CMs, were dried at 50 °C. The concentrations of CMs in the bulk samples were 0.02–1.96 wt.%.

3.2.3. Heating experiment

To reproduce heating during earthquake slip, we heated CMs retrieved from the host rock in the TG-DSC apparatus to target temperatures of 100, 200, 300, 400, 500, 600, 700, 800, 900, and 1000 °C. Although the rate of temperature rise during an earthquake is generally several tens to several hundreds of degrees per second, we adopted a heating rate of 50 °C min^{-1} in our experiments owing to a limitation of the apparatus. An Ar gas atmosphere was adopted because the natural condition of faults at depth is expected to be anoxic (e.g. Wakita et al., 1980). Although the thermal diffusivities of the bulk rock and CM differed, the difference in their temperature profiles during the heating experiment was only several tens of degrees

(Supporting Information Figure S3.1), which, because it is much smaller than the temperature step, did not affect interpretation of the heating experiment results.

3.2.4. Characterization of the host-rock CM by TG-DSC and py-GC/MS

Baseline thermo- and organochemical information, that is, TG-DSC curves and pyrograms, about the CM in the surrounding host rock is required to evaluate the changes that may have been induced by heating in the slip zone.

Approximately 20 mg of the host-rock CM was heated from room temperature to 1000 °C at a rate of 20 °C min^{-1} in an Ar atmosphere. The resultant TG curve showed a mass loss that started at 100 °C, became more rapid at 450–550 °C, and reached 16 wt.% at 1000 °C, whereas the DSC curve showed three endothermic peaks, at 100, 350, and 500 °C, and an exothermic peak at around 850 °C (Figure 3.2a).

To analyze the thermo- and organochemical properties on a molecular level, we used a py-GC/MS system consisting of a pyrolyzer (EGA/PY-3030D, Frontier Lab) directly coupled to a gas chromatograph–mass spectrometer (GCMS-QP2010 SE, Shimadzu) equipped with an UltraALLOY-5 column (30 m length, 0.25 mm inner diameter, 0.25 μm film thickness). Approximately 3 mg of the CM was heated from 100 to 400 °C at a rate of 50 °C min^{-1} and held at 400 °C for 1 min under vacuum, and the gas-phase pyrolysate was collected in a cryotrap and analyzed by GC/MS. We also prepared CM that was pre-heated to 400 °C using the TG-DSC apparatus. Then, approximately 3 mg of the pre-heated sample was heated from 400 to 1000 °C at the rate of 50 °C min^{-1} and held at 1000 °C for 1 min. The gas-phase pyrolysate released from the sample was also analyzed by GC/MS. For our GC/MS analysis, helium was adopted as the carrier gas at a flow rate of 1 mL min^{-1} and a split rate of 50 (where a higher split rate means a lower concentration of organic gas injected into the GC/MS system). The injection temperature was 300 °C, and the column temperature program was as follows: hold at 40 °C for 2 min, heat to 310 °C at 15 °C min^{-1}, and hold at 310 °C for 10 min. The mass spectrometer was operated in electron ionization mode (70 eV, scan range m/z 35–600), and the ion source temperature was

maintained at 230 °C. The pyrolysates were identified by comparing their mass spectra with the reported spectra of standards in the library of the National Institute of Standards and Technology. The pyrolysate produced at 100–400 °C was composed mainly of cycloalkanes and bicyclic or polycyclic aromatic molecules such as phenanthrene, naphthalene, and fluorene (Figure 3.2b), whereas that emitted at 400–1000 °C was dominated by single-ring aromatic molecules such as benzene, toluene, and phenol (Figure 3.2c). No peaks of n-alkanes or other aliphatic hydrocarbonyl chain molecules were detected on either pyrogram (Figure 3.2b and c).

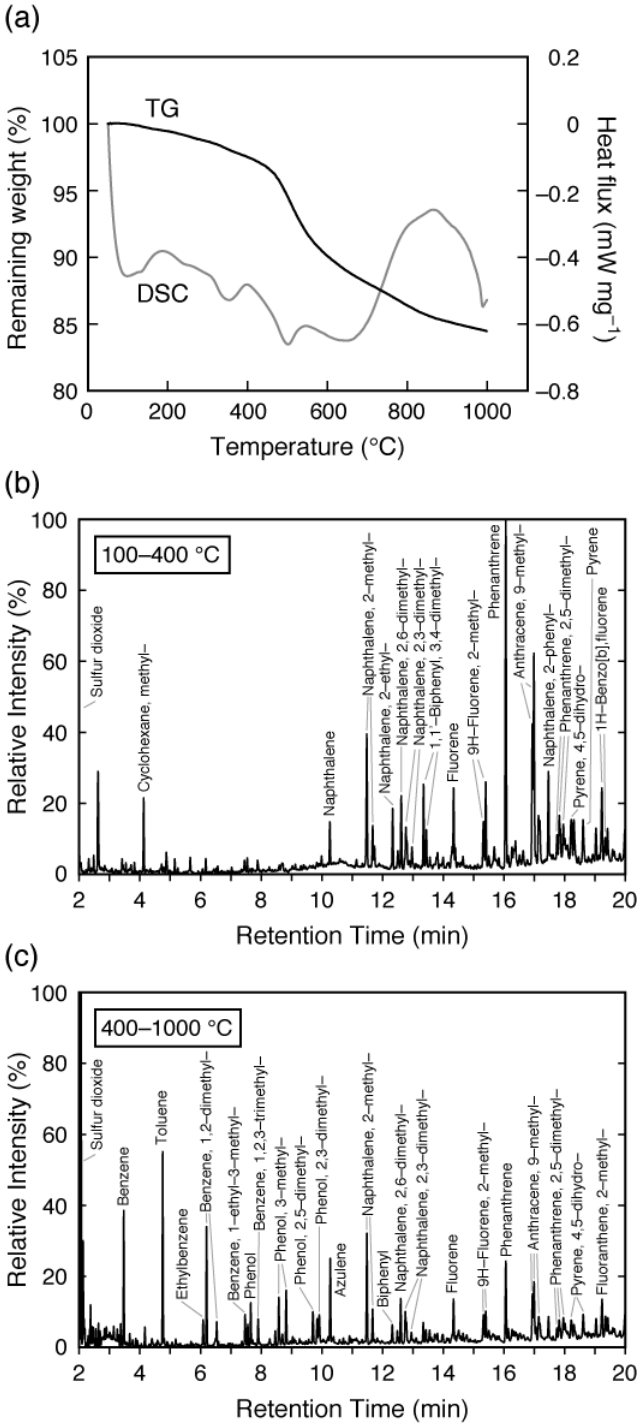

Figure 3.2. Thermogravimetric profile and gas chromatographs of CMs from host rock: (a) thermogravimetric (TG) and differential scanning calorimetric (DSC) curves in the 50–1000 °C temperature range. (b) Pyrogram obtained by heating the sample from 100 to 400 °C. (c) Pyrogram obtained by heating the sample from 400 to 1000 °C.

3.2.5. IR spectroscopy

IR spectroscopy has been traditionally used for organochemical characterization of CMs (e.g., Bent & Brown, 1961), and representative IR absorptions of CMs have been well reported (e.g., Stuart, 2004): a broad band at around 3400 cm^{-1} is attributable to O–H stretching of adsorbed water and O–H stretching of phenol; sharp peaks at around 2960, 2930, and 2860 cm^{-1} are attributable to asymmetric aliphatic CH_3 stretching, asymmetric aliphatic CH_2 stretching, and symmetric aliphatic CH_2 stretching vibrations, respectively; a small peak at around 1680 cm^{-1} is attributable to C=O stretching of carbonyl groups; a sharp peak at around 1600 cm^{-1} is attributable to aromatic C=C stretching vibration; and sharp peaks at around 1455 and 1375 cm^{-1} are attributable to asymmetric aliphatic CH_3 bending and symmetric aliphatic CH_3 bending vibrations, respectively.

We used a Fourier transform IR spectrometer (FT/IR-4700, Jasco) equipped with an IR microscope (IRT-5200, Jasco) to obtain IR absorption spectra of both the CMs retrieved from the slip zone and surrounding host-rock samples, as well as the products of the heating experiments. The samples were hand-pressed to avoid saturation of IR transmission spectra and placed on a CaF_2 plate. Before the IR analyses, all samples and plates were dried at 50 °C for several hours, because adsorbed water on the targeted surface affects the IR spectra (because the water can be released at the analysis temperature). To acquire one IR spectrum, one hundred spectra were accumulated under the following measurement conditions: wavenumber resolution of 4 cm^{-1}; wavenumber range of 4000–1000 cm^{-1}; 50 x 50 μm^2 aperture size; and removal of the background by a blank CaF_2 plate. Because, in accordance with the Lambert-Beer law, IR absorbance depends on the sample thickness and the concentration of the target substance, sample thickness was roughly controlled to several tens of micrometers.

3.2.6. Raman spectroscopy

Raman spectroscopy is widely used for the characterization of CMs: recent progress is well reviewed by Potgieter-Vermaak et al. (2010). The Raman spectrum of CM generally

includes disordered (D, 1355–1380 cm^{-1}) and graphite (G, 1575–1620 cm^{-1}) bands (Tuinstra & Koenig, 1970). The intensity ratio of the D and G bands (I_D/I_G) and the ratio of the D band area (A_D) to the total area of all bands (including the G band) of CMs increase with pyrolysis temperature (Wopenka & Pasteris, 1993; Li et al., 2006).

Although some studies have adopted a complicated waveform separation of four sub-peaks at around 1350–1700 cm^{-1} (e.g., Beyssac et al., 2002; Furuichi et al., 2015), the attribution of the sub-peaks at the molecular level is not based on complete physicochemical understanding. Therefore, we used only the D and G bands for our spectroscopic analysis. We used a Raman microspectrometer equipped with a 532 nm laser (XploRa, Horiba Jobin Yvon) for both the CMs retrieved from the slip zone and surrounding host rocks and the products of the heating experiments. All samples were dried at 50 °C for several hours just before the measurements. The spectra were measured for each point with exposure time of 10 s, a laser spot size of 5 μm, and laser power of 0.13 mW on the targeted surface. The intensities and areas of the D and G bands were determined by using PeakFit 3.0 software (Systat Software) after a baseline correction to remove fluorescence interference. A representative combination of observed and fitted spectra for each sample is shown in Supporting Information Figure S3.2. For each sample, spectra were obtained from 10 points, and the average values of I_D/I_G and A_D/A_G at the 10 points were adopted.

3.2.7 Organic elemental analysis

Organic materials are classified according to their organochemical composition (Tissot & Welte, 1984). CMs such as coal and kerogen are mainly composed of carbon (C), hydrogen (H), oxygen (O), sulfur (S), and nitrogen (N) (e.g., Hatcher & Breger, 1982), and the content of each component depends on the original source (e.g. marine or terrestrial) and the degree of maturation (e.g., Behar & Vandenbroucke, 1987). Laboratory heating experiments have demonstrated systematic changes in the elemental composition of organic materials with increasing temperature (e.g., Schnitzer & Hoffman, 1965). The atomic ratios of elements

composing the materials have also been used as maturation indices of CMs: Sawada et al. (2000) demonstrated experimentally that the H/C ratio of carbonized wood decreases with increasing temperature, and Spokas (2010) confirmed the systematic correlation between pyrolytic temperature and the O/C ratio of various CMs. A van Krevelen diagram (on which the atomic O/C ratio is plotted on the X-axis and the atomic H/C ratio on the Y-axis) is an accepted method of evaluating the degree of maturation (van Krevelen, 1961).

Elemental compositions of both the CMs retrieved from the slip zone and surrounding host rocks and the products of the heating experiments were measured with an elemental analyzer (Flash EA 1112, Thermo Finnigan). Approximately 1 mg of dried sample wrapped with tin (Sn) film was first heated to 1000 °C to dissolve the film and then combusted at 1800 °C in a quartz column. In the CHNS measurement mode, N_2, SO_2, CO_2, and H_2O from the heated sample were separated in a quartz tube filled with copper oxide as an oxidant and with reduced copper as a reductant. Helium was adopted as both the carrier and reference gas at flow rates of 130 and 100 ml min^{-1}, respectively. In the O measurement mode, a carbon nickel plate, quartz turning, soda lime, and magnesium perchlorate in the quartz tube were used to extract CO gases from the pyrolysates. Flow rates of helium, used as both the carrier and reference gas, were 130 and 100 ml min^{-1}, respectively. The concentration of each separated gas was measured by the analyzer. Sulfanilamide (C, 41.84 wt.%; H, 4.68 wt.%; N, 16.27 wt.%; S, 18.62 wt.%; O, 18.58 wt.%) was used as a standard substance to obtain a calibration curve for each element, and the resultant accuracies of the H/C and O/C ratios were within 0.001.

3.3. Results

3.3.1. IR spectra of CMs of the Kure OST and surrounding rocks

The IR spectra of the CMs from all samples except SZ02 exhibited sharp absorbance peaks at around 2960, 2930, and 2860 cm^{-1}, which were attributed to asymmetric aliphatic CH_3 stretching, asymmetric aliphatic CH_2 stretching, and symmetric aliphatic CH_2 stretching vibrations, respectively. In contrast, these peaks were hardly detectable in SZ02 (Figure 3.3a).

Weak peaks at around 1455 and 1375 cm^{-1}, attributed to asymmetric aliphatic CH_3 bending and symmetric aliphatic CH_3 bending vibration, respectively, were also observed in SZ01 and the host-rock and fractured zone samples but not in SZ02 or the sandstone clast sample. All samples exhibited peaks at around 1600 cm^{-1}, attributed to aromatic C=C stretching vibration, but in SZ02 and the sandstone clast, this peak was relatively broad and weak. All samples exhibited small peaks at around 3050 cm^{-1}, attributed to aromatic C–H stretching vibration, but the peak in SZ02 was much weaker than in the other samples.

3.3.2. Raman spectra of CMs of the Kure OST and surrounding rocks

All samples showed broad bands at around 1355 cm^{-1} (D band) and 1600 cm^{-1} (G band) (Figure 3.3b). The peak intensity ratios (I_D/I_G) and the band area ratios (A_D/A_G) are given in Table 1. The I_D/I_G ratio of SZ02 and fractured rock is 0.622 ± 0.010 and 0.617 ± 0.011, respectively, whereas the ratios of SZ01, the host rock, and the sandstone clast are relatively low (0.587 ± 0.007, 0.575 ± 0.007, and 0.580 ± 0.008, respectively). A_D/A_G ratio in the slip zones (SZ01 and SZ02) are 1.618 ± 0.114 and 1.586 ± 0.064, respectively, whereas the ratio in the surrounding host/deformed rocks is slightly lower: 1.322 ± 0.072, 1.500 ± 0.061, and 1.458 ± 0.066 for host rock, fractured zone, and sandstone clast, respectively.

Table 3.1. Raman spectra D and G band ratios (mean ± *SD*, n = 10) and organic elemental components of the CMs retrieved from the Kure OST and the surrounding deformed rocks and host rock.

Structure	Raman spectra		Organic elements and atomic ratios				
	I_D/I_G	A_D/A_G	C (mol/100 g)	H (mol/100 g)	O (mol/100 g)	H/C	O/C
Slip zone 01	0.587 ± 0.007	1.618 ± 0.114	5.849	3.481	0.367	0.595	0.063
Slip zone 02	0.622 ± 0.010	1.586 ± 0.064	5.245	2.274	0.221	0.434	0.042
Sandstone clast	0.580 ± 0.008	1.458 ± 0.066	6.736	4.920	0.219	0.730	0.033
Fractured rock	0.617 ± 0.011	1.500 ± 0.061	6.317	4.464	0.392	0.707	0.062
Host rock	0.575 ± 0.007	1.322 ± 0.072	4.406	4.458	0.359	1.012	0.082

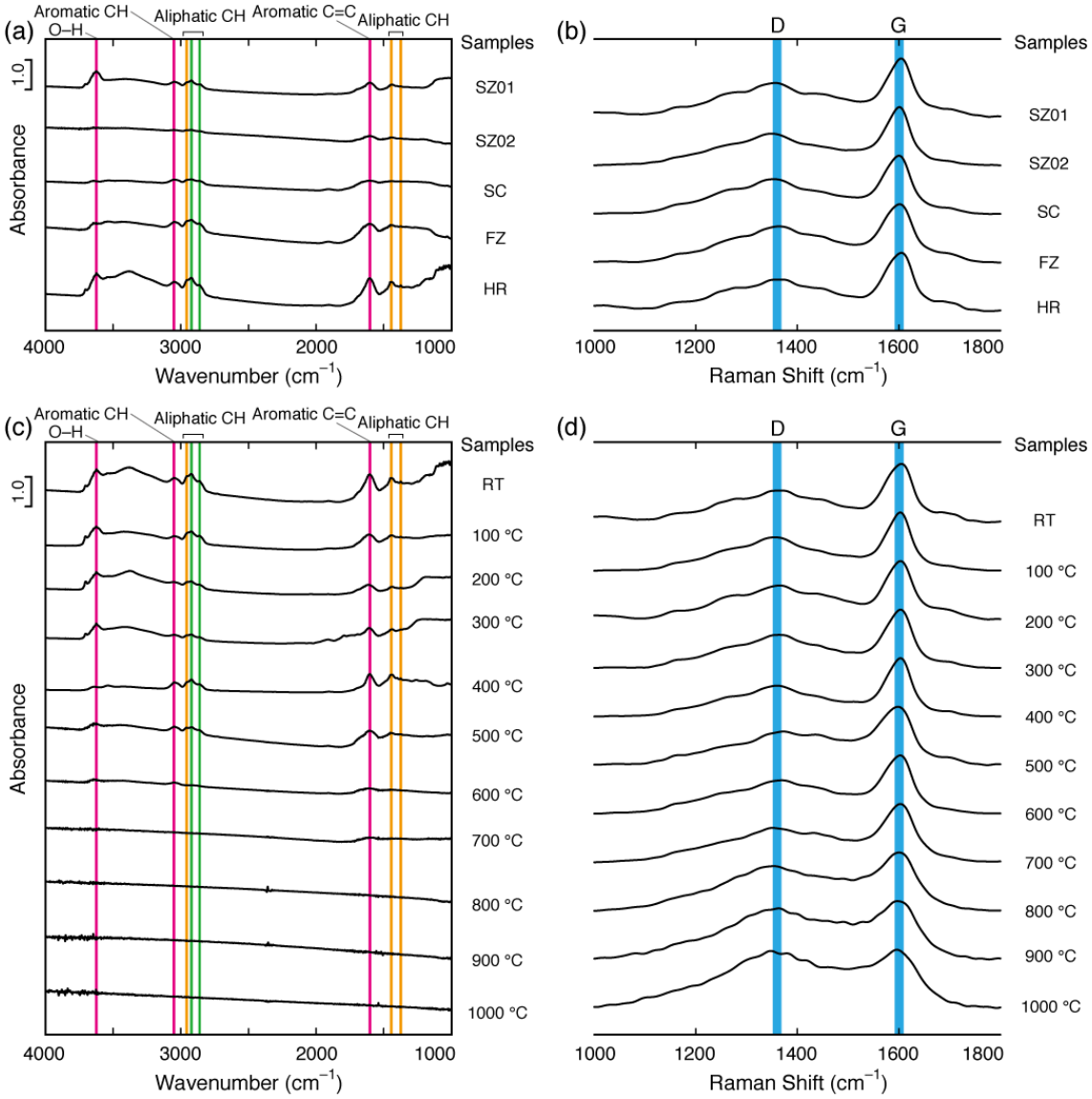

Figure 3.3. IR and Raman spectra of the CMs from the Kure OST and of the products resulting from heating host-rock CMs in a series of heating experiments. (a) IR spectra and (b) Raman spectra of CMs from the Kure OST and surrounding deformed and host rocks. (c) IR spectra and (d) Raman spectra of the products obtained by heating the host-rock CMs to the indicated temperatures. SZ, slip zone; SC, sandstone clast; FR, fractured rock; HR, host rock; RT, room temperature.

3.3.3. Organic elemental compositions of CMs of the Kure OST and surrounding rocks

The elemental compositions (concentrations of C, H, and O) and the atomic ratios of H/C and O/C of all samples are given in Table 1. Although no systematic differences in the C or O content were detected among the samples, the H concentration in the slip zone (SZ01, 3.481; SZ02, 2.274) is low compared with that in the other samples (range, 4.458–4.920). The H/C ratios in the slip zone (SZ01, 0.595; SZ02, 0.434) are lower than the ratios in the host and deformed rocks (range, 0.707–1.012). The highest O/C ratio was observed in the host rock (0.082); in the slip zone and deformed zone, the ratio ranged from 0.033 to 0.063.

3.3.4. IR spectra of host-rock CMs after heating

The IR spectra of the host-rock CMs after heating are shown in Figure 3.3c. The absorbance peaks due to aliphatic components (2960, 2930, 2860, 1455, and 1375 cm^{-1}) disappear after heating to 600 °C. The sharp peak of aromatic C=C at 1600 cm^{-1} becomes weak after heating to 600 °C and disappears when the materials were heated to 800 °C; the aromatic C–H peak at 3050 cm^{-1} also becomes weak after heating to 600 °C and almost completely disappears after heating to 700 °C.

3.3.5. Raman spectra of host-rock CMs after heating

The Raman spectra of the products of the heating experiments are shown in Figure 3.3d. All heated products exhibit D and G bands (1355 and 1600 cm^{-1}), but the intensity of the D band relative to that of the G band increases with increasing temperature. The intensity ratio (I_D/I_G) and band area ratio (A_D/A_G) of all products and the starting CM are summarized in Table 2. The I_D/I_G ratio increased slightly when the temperature was elevated to 400 °C (from 0.575 ± 0.007 to 0.595 ± 0.008), and it increased drastically with heating to 500 °C and higher, reaching 1.166 ± 0.014 at 1000 °C. In contrast, the A_D/A_G ratio did not show any systematic change below 700 °C (ranging from 1.400 ± 0.076 to 1.672 ± 0.026), but it increased greatly as the temperature was elevated to 800 °C and above, reaching 2.418 ± 0.245 at 1000 °C. We compare

these changes with temperature to the ratios obtained for the host-rock (starting CM) and slip-zone samples (Figure 3.4).

Table 3.2. Raman spectra D and G band ratios (mean ± *SD*, *n* = 10) and organic elemental components of products obtained by heating the host-rock CMs.

Heating temperature (°C)	Raman spectra		Organic elements and atomic ratios				
	I_D/I_G	A_D/A_G	C (mol/100 g)	H (mol/100 g)	O (mol/100 g)	H/C	O/C
RT	0.575 ± 0.007	1.322 ± 0.072	4.406	4.458	0.359	1.012	0.082
100	0.583 ± 0.008	1.553 ± 0.092	4.072	3.355	0.374	0.824	0.092
200	0.579 ± 0.008	1.497 ± 0.051	4.440	3.555	0.321	0.801	0.072
300	0.590 ± 0.006	1.400 ± 0.076	4.130	3.095	0.337	0.749	0.082
400	0.595 ± 0.008	1.479 ± 0.042	3.761	2.263	0.364	0.602	0.097
500	0.606 ± 0.007	1.510 ± 0.047	4.378	2.489	0.268	0.568	0.061
600	0.638 ± 0.007	1.672 ± 0.026	4.691	1.660	0.192	0.354	0.041
700	0.695 ± 0.012	1.553 ± 0.073	4.546	0.554	0.148	0.122	0.033
800	0.890 ± 0.012	1.713 ± 0.021	4.546	0.674	0.122	0.148	0.027
900	1.046 ± 0.018	2.119 ± 0.201	3.985	0.278	0.085	0.070	0.021
1000	1.166 ± 0.014	2.418 ± 0.245	4.872	0.240	0.108	0.049	0.022

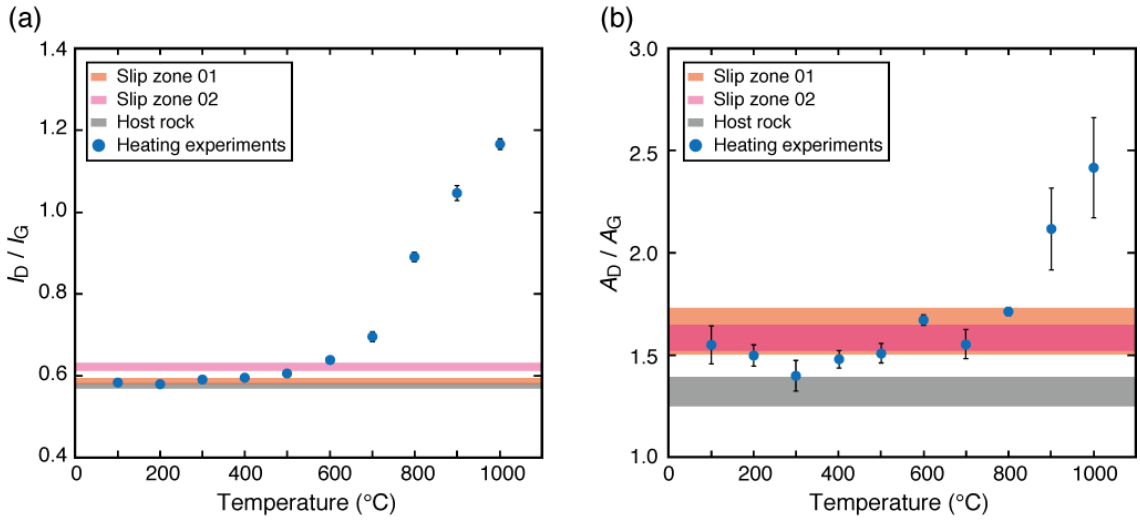

Figure 3.4. Temperature dependences of Raman spectral parameters. (a) I_D/I_G ratios and (b) A_D/A_G ratios of the CMs from the Kure OST samples and of the products obtained by heating the host-rock CMs.

3.3.6. Organic elemental compositions of host-rock CMs after heating

The elemental compositions and the atomic ratios of H/C and O/C in the host-rock CMs after heating are summarized in Table 2. Although the C content did not show any remarkable change with temperature, the H and O contents tended to decrease with increasing temperature. The H/C ratio decreased systematically with increasing temperature, and it decreased sharply from 500 to 700 °C. The O/C ratio did not show any systematic change below 400 °C, but above that, it decreased significantly. We compared the changes in the H/C and O/C ratios with temperature to those in the host-rock (starting CM) and slip-zone samples (Figure 3.5a and b, respectively).

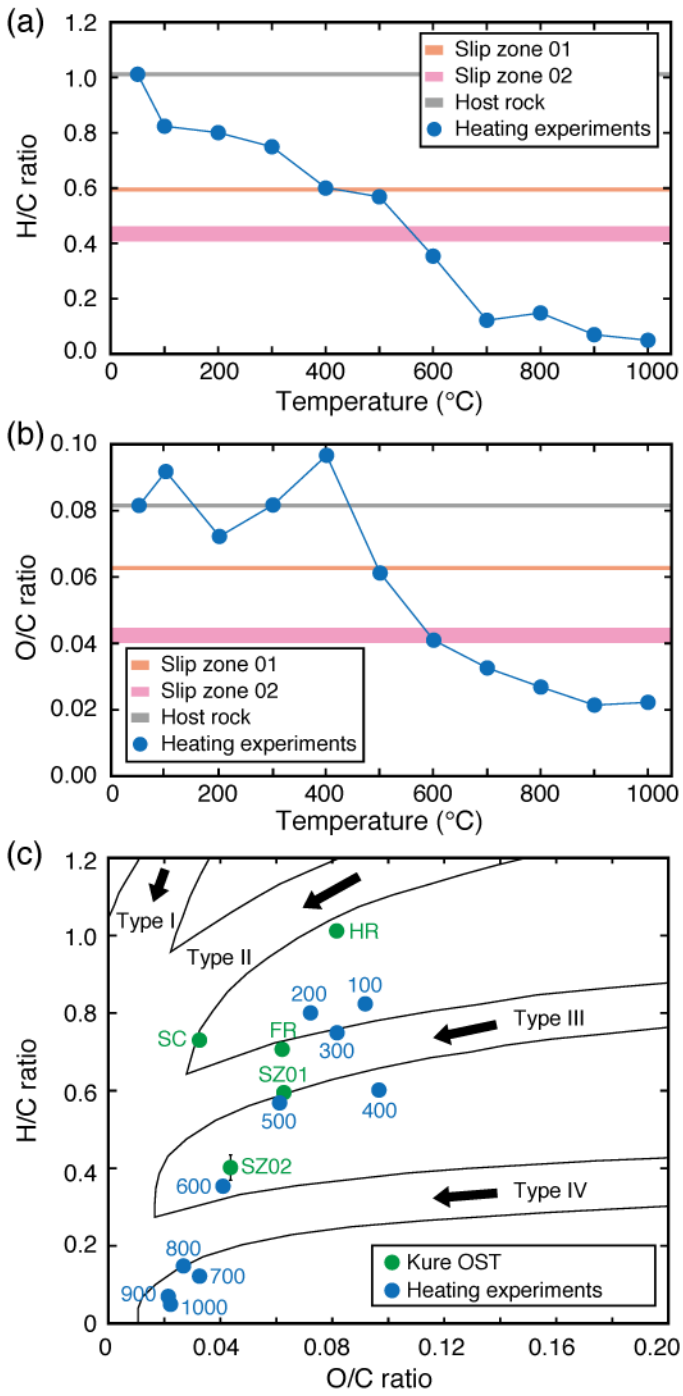

Figure 3.5. Organic elemental compositional data of the CMs from the Kure OST samples and of the products obtained by heating the host-rock CMs. (a) H/C ratio. (b) O/C ratio. (c) The results plotted on a van Krevelen diagram together with information on kerogen types. Large black arrows indicate the trend of thermal maturation.

3.4. Discussion

3.4.1. Characterization of CMs from the host rock

Because the chemical structure of a CM dramatically affects the maturation (also graphitization) process (e.g., Oberlin, 1984), we first discuss the thermo- and organochemical characteristics of the CM retrieved from the host rock and used in the heating experiments. The H/C and O/C atomic ratios of the unheated material (1.012 and 0.082, respectively) corresponds to those of Type II kerogen, which is derived mainly from marine muddy sediments (Hunt, 1995) (Figure 3.5c). These ratios are the characteristics of high-volatile bituminous coal (Hatcher & Breger, 1982).

Bituminous coal is generally composed of massive aromatic nuclei, and these aromatic aggregations are linked by aliphatic hydrocarbon chains (e.g., Mathews & Chaffee, 2012). Diagenesis on a geological timescale induces breakage of weak bonds, aromatization, and structural rearrangement (Behar & Vandenbroucke, 1987). Conversely, rapid heating triggers pyrolysis together with the release of a gas-phase volatile fraction composed mainly of various low-molecular-weight hydrocarbons (e.g., Lievens et al., 2013).

The host-rock CM in this study showed a large weight loss and endothermic peaks on the TG-DSC curves, clearly indicating that heating causes pyrolysis of these materials (Figure 3.2a). In the 100–400 °C temperature range, thermal breakage of weak aliphatic chains is the dominant process (e.g., Xu et al., 2014), and it is accompanied by the release of low-molecular-weight organic gases. These processes are reflected in the 100–400 °C pyrogram, on which peaks of bicyclic and polycyclic aromatics such as phenanthrene, naphthalene, and fluorene are prominent (Figure 3.2b), as well as endothermic peak with a little weight loss at around 350 °C (Figure 3.2a). Gasthauer et al. (2008) demonstrated that polycyclic aromatic compounds with more than two aromatic rings can be released from asphalt at ≥160 °C, which supports our observation that such aromatic compounds are subject to decomposition in the 100–400 °C temperature range due to thermal breakage of aliphatic C–H chains. The decomposition of aromatic nuclei occurs dominantly at around the 450–500 °C temperature range (e.g., Peuravuori et al., 1999), which could account for the endothermic peak at around

500 °C in DSC curve (Figure 3.2a). In actuality, the volatile fractions released at over 400 °C were composed mainly of benzene, phenol, and toluene, and were much greater compared with those released due to thermal breakage of aliphatic C–H chains (Figure 3.2c), indicating that not only breakage of aliphatic C–H chains but also decomposition of aromatic nuclei could contribute to a large weight loss at around 500 °C (Figure 3.2a). We attribute the sharp exothermic peak at 850 °C on the DSC curve to the growth of aromatic rings (Figure 3.2a).

3.4.2. Changes in spectroscopic characteristics of CMs from the host rock after heating and from the slip zone

The disappearance of the absorbance peaks of aliphatic CH_2 and CH_3 at 2960, 2930, and 2860 cm^{-1} at 600 °C may have been caused by the extinction of aliphatic C–H bonding. The disappearance of the aromatic C=C (1600 cm^{-1}) and C–H (3050 cm^{-1}) peaks at 600 °C may have been caused by thermal decomposition of aromatic components, and it coincided with the large endothermic weight loss on the TG-DSC curves at the 450–550 °C temperature range and the release of gas-phase toluene and other methyl aromatic compounds on the 400–1000 °C pyrograms.

The large increase in the I_D/I_G ratio above 600 °C together with the exotherm peak can be attributed to the growth of aromatic rings and the formation of stronger C–C bonds, that is, aromatization. The A_D/A_G ratio showed no systematic change at ≤700 °C but increased at ≥800 °C, probably also a result of aromatization.

In the CMs from slip zone sample SZ02, no or very weak aliphatic peaks were observed but slight aromatic peaks were detected on the IR spectrum. Comparison of that spectrum with the results of the heating experiments suggests that the slip-zone materials may correspond to the product obtained after heating host-rock materials to 600 °C. This correspondence is supported by the I_D/I_G ratio of SZ02, which roughly coincided with that of 600 °C heated product. The spectra of the other slip zone sample (SZ01) and its I_D/I_G and A_D/A_G ratios were similar to those of the product after 500 °C heating.

3.4.3. Changes in organic elemental compositions of CMs from the host rock after heating and from the slip zone

On the van Krevelen diagram (Figure 3.5c), the H/C ratios of the heated CMs retrieved from the host rock systematically decreased with increasing temperature, as did the O/C ratios, although less systematically. These trends basically coincide with those of maturation through diagenesis, but the rapid heating at 50 °C min–1 in our study demonstrated that large shifts due to the thermal breaking of aliphatic C–H bonds, decomposition of some aromatic components and subsequent aromatization, observed in the spectroscopic and thermochemical results, can also occur.

On the diagram, the slip zone samples SZ01 and SZ02 plot near the 500 and 600 °C heated products, respectively, and the fractured rock plot close to the 200 and 300 °C heated product, but the sandstone clast plot away from the trend line of the heated product.

3.4.4. Maximum temperature experienced by the Kure OST and constraints on slip parameters

Our analyses, in which IR and Raman spectroscopic and organic elemental analyses were integrated with a heating treatment, revealed that the Kure OST slip zone experienced high temperatures of 500 °C (SZ01) and 600 °C (SZ02): The IR spectra of SZ01 show sharp aliphatic CH_2 and CH_3 peaks and aromatic C=C and C–H peaks, indicating that SZ01 had not experienced high temperatures of ≥600 °C. Moreover, the Raman spectral parameters and elemental compositions of SZ01 were similar to those produced by heating CM extracted from host-rock samples up to 500 °C. In contrast, the IR spectra of SZ02 showed no aliphatic CH_2 and CH_3 peaks and weak aromatic C=C and C–H peaks, indicating that SZ02 had experienced high temperatures of ≥600 °C. In addition, the Raman spectral parameters and elemental compositions of SZ02 were similar to those produced by heating CM extracted from host-rock samples up to 600 °C. Thus, despite the presence of microstructures such as microlites and quartz embayment structures, suggesting pseudotachylyte with maximum temperature of 650–

1100 °C, as previously reported in the same fault zone (Mukoyoshi et al., 2006), we concluded that the slip zone had experienced temperatures of 500–600 °C. The inconsistency between these temperatures and the temperature suggested by the presence of pseudotachylyte might be explained by flash heating occurring at microscale, which might have generated temperatures high enough to induce localized melting. The maturation process by heating could be attributed mainly to thermal breakage of aliphatic C–H chains and of aromatic C=C and C–H bonds.

Next, we estimated the slip parameters of the Kure OST on the basis of these experienced temperatures. The change in temperature in a slip zone can be expressed by the following one-dimensional heat and thermal diffusion equation:

$$\frac{\partial T}{\partial t} - \frac{\partial}{\partial x}\left(\kappa \frac{\partial T}{\partial x}\right) - \frac{\partial}{\partial t}\left(\frac{\tau D}{w C_p \rho}\right) = 0 \tag{3.1}$$

where T is temperature (K), t is elapsed time after the beginning of slip (t = 0) (s), κ is thermal diffusivity ($m^2\ s^{-1}$), x is the distance from the center of the slip zone (x = 0) (m), τ is shear stress (Pa), D is slip distance (m), w is slip-zone thickness (m), C_p is specific heat capacity ($J\ kg^{-1}\ K^{-1}$), and ρ is density ($kg\ m^{-3}$). For simplicity, convective heat transfer, endothermic processes, slip plane roughness (flash heating), and dynamic fault weakening are ignored. For κ and C_p, we used the values $4.0 \times 10^{-7}\ m^2\ s^{-1}$ and $1750\ J\ kg^{-1}\ K^{-1}$, respectively, obtained from a sample retrieved from a modern megasplay fault in the Nankai Trough (Hirono et al., 2009). The actual thickness, 1 cm, of the localized shear zone was adopted, and the density was assumed to be 1850 kg m–3, as reported from a modern megasplay fault in Nankai Trough (Kinoshita et al., 2009). If it is assumed that the stress normal to the fault was equal to a hydrostatic stress state, in which horizontal stress is equal to the vertical stress, then the amount of frictional heat produced during slip is directly related to the product of the friction coefficient (μ), vertical stress, and slip distance. However, the friction coefficient of the slip zone in the Kure OST is not known, and the burial depth of the rocks around the OST ranged from 2.5 to 5.5 km, as estimated by a vitrinite reflectance analysis (Mukoyoshi et al., 2006); therefore, we used three typical values of μ (0.1, 0.3, and 0.5) and depths of 3, 4, and 5 km. The slip rate during past Nankai earthquakes is also an unknown parameter, so we adopted three values (0.1, 0.5, and 1.0 $m\ s^{-1}$). We also assumed a seafloor temperature of 4 °C and a geothermal gradient of 50 °C km^{-1}.

By numerically solving equation (1) using a 0.1 s time increment, a 0.5 mm grid size, and a constant temperature at x = 200 mm as the boundary condition, we obtained values for the slip necessary to achieve temperatures of 500 and 600 °C for each combination of μ, depth, and slip rate (Figure 3.6).

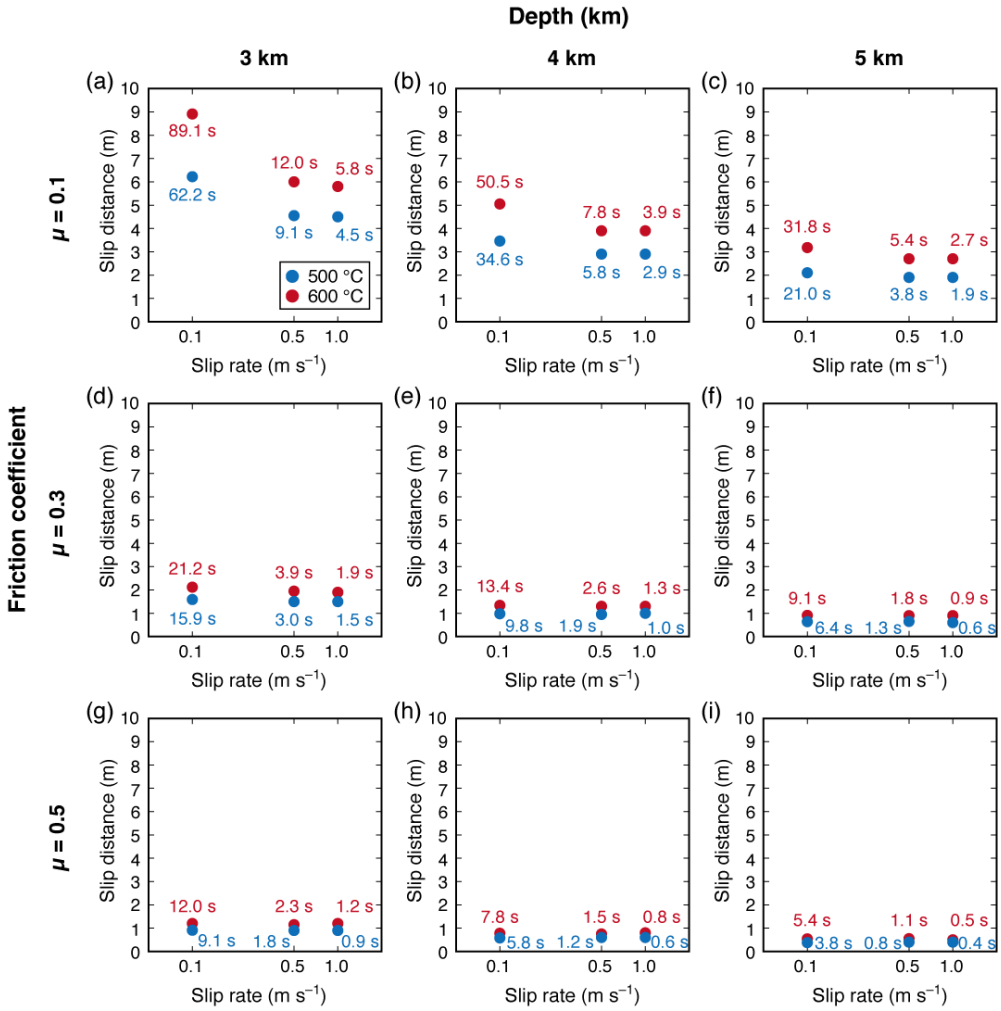

Figure 3.6. Results of numerical simulations showing the relationship between slip rate and displacement at three different depths and for three different values of the friction coefficient (μ): (a) 3 km depth, μ = 0.1; (b) 4 km depth, μ = 0.1; (c) 5 km depth, μ = 0.1; (d) 3 km depth, μ = 0.3; (e) 4 km depth, μ = 0.3; (f) 4 km depth, μ = 0.4: (g) 3 km depth, μ = 0.5; (h) 4 km depth, μ = 0.5; and (i) 5 km depth, μ = 0.5.

High values of μ restrain the amount of slip distance, but recent high-speed friction

experiments have revealed very low friction, μ of ~0.1, for various rocks (e.g. Di Toro et al., 2011); therefore, μ = 0.1 is likely during earthquakes. Thus, a single earthquake event could potentially produce 2–9 m slip distance (Figure 3.6a–c). A slip distance of this magnitude is consistent with historical records of large tsunamis generated by earthquakes (Ando, 1975; Furumura et al., 2011).

Numerous branching faults developed around the Kure OST show a large cumulative slip distance of 2.5–8.5 km (Mukoyoshi et al., 2006), and our targeted slip zone might have contributed to the large accumulation of slip. Thus, a localized slip zone might not have experienced multiple earthquake events. The branching system around the subduction boundary may play an important role not only in the evolution of the accretionary prism but also in rupture propagation from the deep portion of the plate interface and thus in generation of a large tsunami in the case that such a large slip propagates to the seafloor and uplifts the sea surface.

3.5. Conclusions

We performed multiple analyses, including IR and Raman spectroscopy, organic elemental analysis, TG-DSC, and py-GC/MS, of CMs to determine the heating recorded in an ancient megasplay fault and succeeded in estimating a maximum temperature of 600 °C. Here, we emphasize the importance of performing multiple analyses and of taking into consideration how the organochemical characteristics of the materials change with increasing temperature. We also suggest caution because of the uncertainty of a maximum temperature estimated by using a single method such as vitrinite reflectance or Raman spectrum intensity ratios. The temperature dependence of organochemical changes is complex and probably depends on the initial molecular structure of the materials, which is related to their degree of maturation (Hirono et al., 2015); therefore, a complete understanding of that temperature dependence and the final estimation of the maximum temperature experienced in a slip zone require the application of multiple approaches as in this study.

References

Ando, M. (1975). Source mechanisms and tectonic significance of historical earthquakes along the Nankai Trough, Japan. *Tectonophysics* **27**, 119–140.

Behar, F. & Vandenbroucke, M. (1987). Chemical modelling of kerogens. *Org. Geochem.* **11**, 15–24.

Bent, R. & Brown, J.K. (1961). The infra-red spectra of macerals. *Fuel* **40**, 47–56.

Beyssac, O., Goffé, B., Chopin, C. & Rouzaud, J.N. (2002). Raman spectra of carbonaceous material in metasediments: a new geothermometer. *J. Metamorphic Geol.* **20**, 859–871.

Bustin, R.M., Ross, J.V. & Rouzaud, J.-N. (1995). Mechanisms of graphite formation from kerogen: experimental evidence. *Int. J. Coal Geol.* **28**, 1–36.

Collot, J.-Y., Marcaillou, B., Sage, F., Michaud, F., Agudelo, W., Charvis, P., Graindorge, D., Gutscher, M.-A. & Spence, G. (2004). Are rupture zone limits of great subduction earthquakes controlled by upper plate structures? Evidence from multichannel seismic reflection data acquired across the northern Ecuador–southwest Colombia margin. *J. Geophys. Res.* **109**, B11103.

Di Toro, G., Han, R., Hirose, T., De Paola, N., Nielsen, S., Mizoguchi, K., Ferri, F., Cocco, M. & Shimamoto, T. (2011). Fault lubrication during earthquakes. *Nature* **471**, 494–498.

Furuichi, H., Ujiie, K., Kouketsu, Y., Saito, T., Tsutsumi, A. & Wallis, S. (2015). Vitrinite reflectance and Raman spectra of carbonaceous material as indicators of frictional heating on faults: Constraints from friction experiments. *Earth Planet. Sci. Lett.* **424**, 191–200.

Furumura, T., Imai, K. & Maeda, T. (2011). A revised tsunami source model for the 1707 Hoei earthquake and simulation of tsunami inundation of Ryujin Lake, Kyushu, Japan. *J. Geophys. Res.* **116**, B02308.

Gasthauer, E., Mazé, M., Marchand, J.P. & Amouroux, J. (2008). Characterization of asphalt fume composition by GC/MS and effect of temperature. *Fuel* **87**, 1428–1434.

Han, R., Shimamoto, T., Hirose, T., Ree, J.-H. & Ando, J. (2007). Ultralow friction of carbonate faults caused by thermal decomposition. *Science* **316**, 878–881.

Hatcher, P.G. & Breger, I.A. (1982). Nuclear magnetic resonance studies of ancient buried wood–II. Observations on the origin of coal from lignite to bituminous coal. *Org. Geochem.* **4**, 9–18.

Hirono, T. *et al*. (2007). A chemical kinetic approach to estimate dynamic shear stress during the 1999 Taiwan Chi-Chi earthquake. *Geophys. Res. Lett.* **34**, L19308.

Hirono, T. *et al*. (2008). Clay mineral reactions caused by frictional heating during an earthquake: An example from the Taiwan Chelungpu fault. *Geophys. Res. Lett.* **35**, L16303.

Hirono, T., Ujiie, K., Ishikawa, T., Mishima, T., Hamada, Y., Tanimizu, M., Soh, W. & Kinoshita, M. (2009). Estimation of temperature rise in a shallow slip zone of the megasplay fault in the Nankai Trough. *Tectonophysics* **478**, 215–220.

Hirono, T., Maekawa, Y. & Yabuta, H. (2015). Investigation of the records of earthquake slip in carbonaceous materials from the Taiwan Chelungpu fault by means of infrared and Raman spectroscopies. *Geochem. Geophys. Geosyst.* **16**, 1233–1253.

Honda, G., Ishikawa, T., Hirono, T. & Mukoyoshi, H. (2011). Geochemical signals for determining the slip–weakening mechanism of an ancient megasplay fault in the Shimanto accretionary complex. *Geophys. Res. Lett.* **38**, L06310.

Hunt, J. (1995). *Petroleum Geochemistry and Geology*. W. H. Freeman, New York, 743 pp.

Ishikawa, T. *et al*. (2008). Coseismic fluid–rock interactions at high temperatures in the Chelungpu fault. *Nat. Geosci.* **1**, 679–683.

Kinoshita, M. *et al*. (2009). Expedition 316 Site C0004. *Proc. Integr. Ocean Drill. Program* **314/315/316**, Integrated Ocean Drill. Program, College Station, Tex.

Kitamura, M., Mukoyoshi, H., Fulton, P.M. & Hirose, T. (2012). Coal maturation by frictional heat during rapid fault slip. *Geophys. Res. Lett.* **39**, L16302.

Kopp, H. & Kukowski, N. (2003). Backstop geometry and accretionary mechanics of the Sunda margin. *Tectonics* **22**, 1072.

Li, X., Hayashi, J. & Li, C.-Z. (2006). FT-Raman spectroscopic study of the evolution of char structure during the pyrolysis of a Victorian brown coal. *Fuel* **85**, 1700–1707.

Lievens, C., Ci, D., Bai, Y., Ma, L., Zhang, R., Chen, J.Y., Gai, Q., Long, Y. & Guo, X. (2013). A study of slow pyrolysis of one low rank coal via pyrolysis–GC/MS. *Fuel Process. Technol.* **116**, 85–93.

Maekawa, Y., Hirono, T., Yabuta, H., Mukoyoshi, H., Kitamura, M., Ikehara, M., Tanikawa, W. & Ishikawa, T. (2014). Estimation of slip parameters associated with frictional heating during the 1999 Taiwan Chi-Chi earthquake by vitrinite reflectance geothermometry. *Earth Planets Space* **66**, 28.

Mathews, J. & Chaffee, A.L. (2012). The molecular representations of coal–A review. *Fuel* **96**, 1–14.

Mishima, T., Hirono, T., Nakamura, N., Tanikawa, W., Soh, W. & Song, S.-R. (2009). Changes to magnetic minerals caused by frictional heating during the 1999 Taiwan Chi-Chi earthquake. *Earth Planets Space* **61**, 797–801.

Moore, G.F., Bangs, N.L., Taira, A., Kuramoto, S., Pangborn, E. & Tobin, H.J. (2007). Three-dimensional splay fault geometry and implications for tsunami generation. *Science* **318**, 1128–1131.

Mukoyoshi, H., Sakaguchi, A., Otsuki, K., Hirono, T. & Soh, W. (2006). Co-seismic frictional melting along an out-of-sequence thrust in the Shimanto accretionary complex. Implications on the tsunamigenic potential of splay faults in modern subduction zones. *Earth Planet. Sci. Lett.* **245**, 330–343.

Oberlin, A. (1984). Carbonization and graphitization. *Carbon* **22**, 521–541.

Park, J.-O., Tsuru, T., Kodaira, S., Cummins, P.R. & Kaneda, Y. (2002). Splay fault branching along the Nankai subduction zone. *Science* **297**, 1157–1160.

Peuravuori, J., Passo, N. & Pihlaja, K. (1999). Kinetic study of the thermal degradation of lake aquatic humic matter by thermogravimetric analysis. **Thermochim. Acta** *325*, 181–193.

Plafker, G. (1972). Alaskan earthquake of 1964 and Chilean earthquake of 1960: Implications for arc tectonics. *J. Geophys. Res.* **77**, 901–925.

Potgieter-Vermaak, S., Maledi, N., Wagner, N., Van Heerden, J.H.P., Van Grieken, R. & Potgieter, J.H. (2010). Raman spectroscopy for the analysis of coal: a review. *J. Raman*

Spectrosc. **42**, 123–129.

Ross, J.V. & Bustin, R.M. (1990). The role of strain energy in creep graphitization of anthracite. *Nature* **343**, 58–60.

Rowe, C. & Griffith, W.A. (2015). Do faults preserve a record of seismic slip: A second opinion. *J. Struct. Geol.* **78**, 1–26.

Rowe, C.D., Meneghini, F. & Moore, J.C. (2009). Fluid-rich damage zone of an ancient out-of-sequence thrust, Kodiak Islands, Alaska. *Tectonics* **28**, TC1006.

Sawada, Y., Sampei, Y., Hyodo, M., Yagami, T. & Fukue, M. (2000). Estimation of emplacement temperatures of pyroclastic flows using H/C ratios of carbonized wood. *J. Volcanol. Geotherm. Res.* **104**, 1–20.

Schnitzer, M. & Hoffman, I. (1965). Thermogravimetry of soil humic compounds. *Geochim. Cosmochim. Acta* **29**, 859–870.

Scholz, C.H. (2002). *The Mechanics of Earthquakes and Faulting*. 2nd ed, Cambridge University Press, Cambridge, 496 pp.

Spokas, K.A. (2010). Review of the stability of biochar in soils: predictability of O:C molar ratios. *Carbon Management* **1**, 289–303.

Stuart, B. (2004). *Infrared Spectrometry: Fundamentals and Applications*. John Wily, Chichester, England, U.K., 244 pp.

Tissot, B.P. & Welte, D.H. (1984). *Petroleum formation and occurrence*. Springer, Berlin, 699 pp.

Tsuji, T., Ashi, J., Strasser, M. & Kimura, G. (2015). Identification of the static backstop and its influence on the evolution of the accretionary prism in the Nankai Trough. *Earth Planet. Sci. Lett.* **431**, 15–25.

Tuinstra, F. & Koenig, J.L. (1970). Raman spectrum of graphite. *J. Chem. Phys.* **53**, 1126–1130.

Underwood, M.B., Hibbard, J.P. & Ditullio, L. (1993). Geologic summary and conceptual framework for the study of thermal maturity within the Eocene–Miocene Shimanto Belt, Shikoku Japan. *Spec. Paper Geol. Soc. Am.* **273**, 1–24.

Van Krevelen, D.W. (1961). *Coal*. Elsevier, Amsterdam, 514 pp.

Wakita, H., Nakamura, Y., Kita, I., Fujii, N. & Notsu, K. (1980). Hydrogen release: New indicator of fault activity. *Science* **210**, 188–190.

Wilks, K.R., Mastalerz, M., Bustin, R.M. & Ross, J.V. (1993). The role of shear strain in the graphitization of a high-volatile bituminous and an anthracitic coal. *Int. J. Coal Geol.* **22**, 247–277.

Wopenka, B. & Pasteris, J.D. (1993). Structural characterization of kerogens to granulite-facies graphite: Applicability of Raman microprobe spectroscopy. *Am. Mineral.* **78**, 533–557.

Xu, T., Shi, H., Wang, H. & Huang, X. (2014). Dynamic evolution of emitted volatiles from thermal decomposed bituminous materials. *Constr. Build. Mater.* **64**, 47–53.

Supporting information

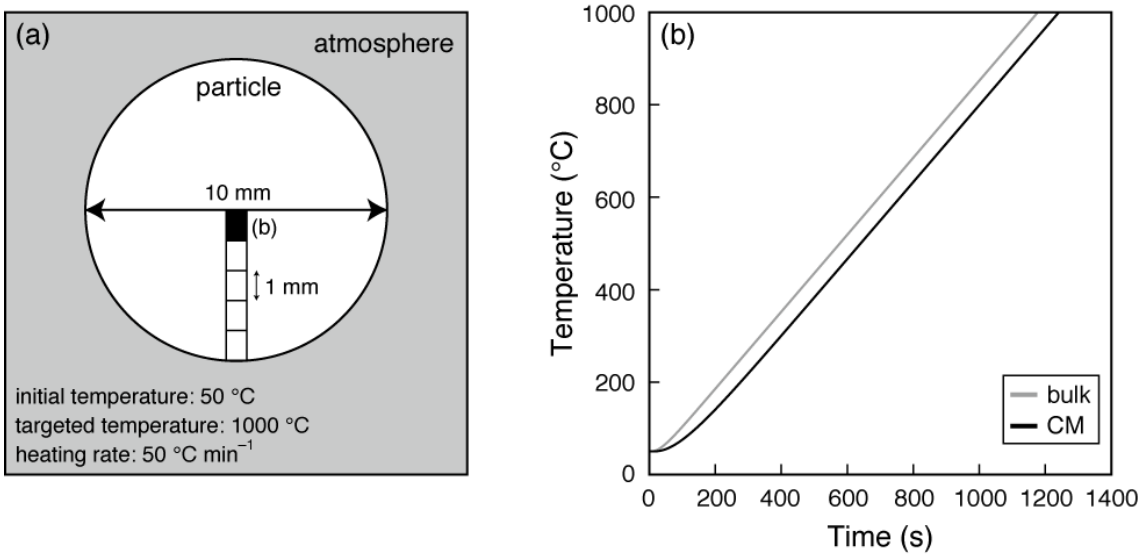

Figure S3.1. Simulation of thermal conduction during heating experiments. (a) Spherical particle of CM or a bulk rock sample modeled in our one-dimensional thermal diffusion simulation. The diameter is 10 mm, and the grid size is 1 mm. The time increment is 0.1 s, the initial temperature is 50 °C, the heating rate is 50 °C min^{-1}, and the final targeted temperature is 1000 °C. The thermal diffusivities of the bulk sample and pure CM were assumed to be 4.0 x 10^{-7} and 1.5 x 10^{-7} m^2 s^{-1}, respectively. (b) Changes with time of the temperature at the center of the bulk sample and pure CM.

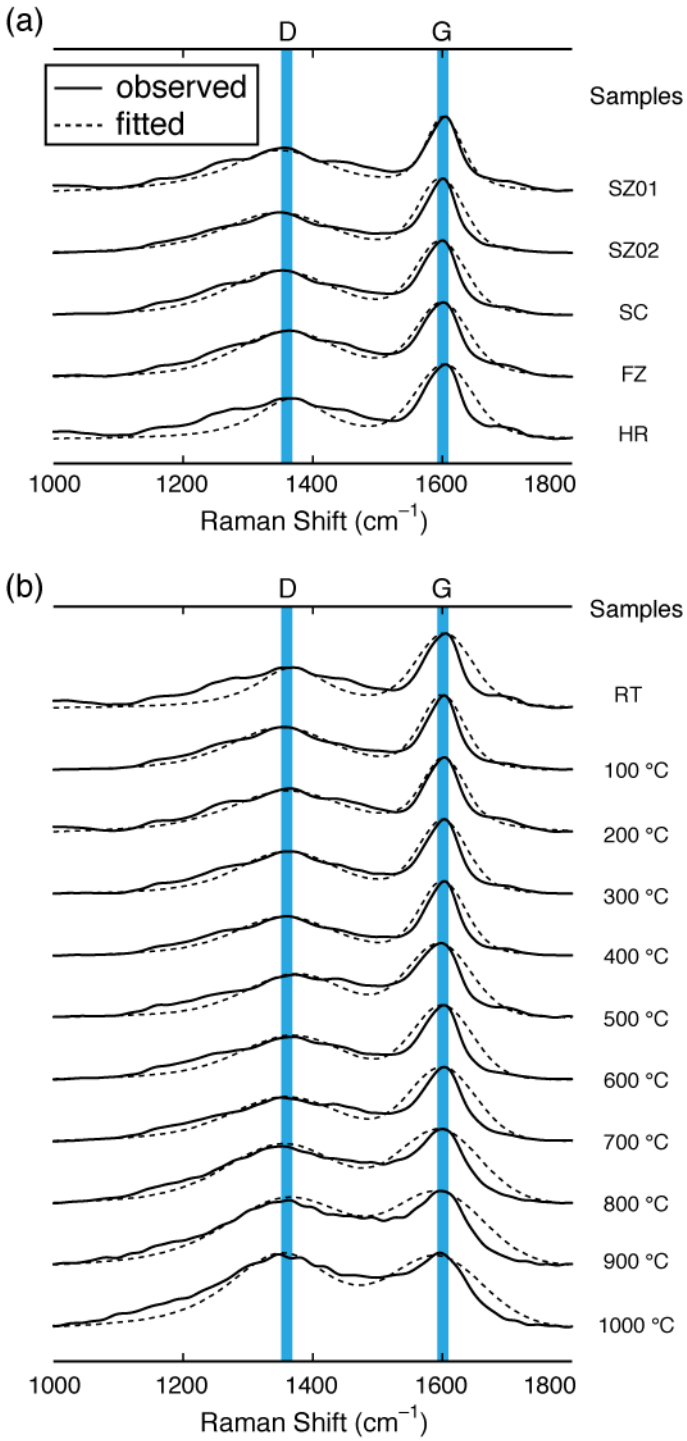

Figure S3.2. Observed and fitted Raman spectra of (a) CMs from the Kure OST and (b) products obtained by heating host-rock CMs in a series of heating experiments.

Chapter 4

Mechanochemical effect on maturation of carbonaceous material: implications for thermal maturity as a proxy for temperature in estimation of coseismic slip parameters

Reprinted from *Geophysical Research Letters* **45**, 2248–2256. Kaneki, S., Ichiba, T. & Hirono, T. (2018). Mechanochemical effect on maturation of carbonaceous material: implications for thermal maturity as a proxy for temperature in estimation of coseismic slip parameters, with permission from John and Wiley Sons.

Abstract

Because shear stress in a fault is directly related to the frictional heat generated during slip, the thermal maturity of carbonaceous material (CM) has been used as a proxy for fault-rock temperature. We used infrared (IR) and Raman spectroscopic analyses and friction and heating experiments to investigate enhancement of the maturation of lignite by shear damage (the mechanochemical effect) and explored the resultant implications for the use of the thermal maturity of lignite as a proxy for temperature. We showed that higher shear stress applied to lignite samples resulted in greater progression of the thermal destruction of aliphatic C–H chains and the survival of the stronger C–C bonds. Thus, we demonstrated that shear damage during earthquake slip causes mechanochemical enhancement of organochemical reactions related to the aromatization of lignite. Our results suggest that shear stress estimated from Raman spectroscopic analyses in previous studies might have been overestimated.

4.1. Introduction

Estimation of seismic slip parameters, such as shear stress and slip distance, is of major importance for understanding earthquake dynamics. The increase of temperature in a fault during an earthquake is a function of such seismic parameters, so in situ borehole measurements of temperature in a fault immediately after an earthquake can be used to estimate the residual heat caused by earthquake slip. Such measurements and analyses were undertaken on the Taiwan Chelungpu fault after the 1999 Chi-Chi earthquake (Kano et al., 2006) and in the Japan Trench after the 2011 Tohoku-oki earthquake (Fulton et al., 2013). However, opportunities to measure residual heat in fault rocks immediately after an earthquake are few and far between. Consequently, several proxies have been used to attempt to detect frictional heat recorded in fault rocks in various regions of the world. They include the generation of frictional melt (pseudotachylyte) during slip (Di Toro et al., 2005), formation of magnetite by thermal decomposition of paramagnetic minerals (Mishima et al., 2006), thermal decomposition of carbonate minerals (Han et al., 2007; Hirono et al., 2007), dehydroxylation reactions of clay

minerals (Hirono et al., 2008), anomalous concentrations of fluid-mobile elements (Ishikawa et al., 2008; Honda et al., 2011), and biomarker indexes (e.g., Savage et al., 2014).

The reflectance of vitrinite, a maceral derived from the burial of woody material, has often been used as a temperature proxy to determine the frictional heat recorded in faults (O'Hara, 2004; Sakaguchi et al., 2011; Maekawa et al., 2014; Furuichi et al., 2015). The reflectance of vitrinite increases irreversibly when it is exposed to high temperatures (e.g., Sweeney & Burnham, 1990). Friction experiments conducted on carbonaceous materials (CM; coal and vitrinite) by using slip velocities on the order of meters per second to simulate the rapid heating that occurs during earthquake slip have demonstrated that vitrinite reflectance increased even by heating of less than 10 s duration (O'Hara et al., 2006; Kitamura et al., 2012; Furuichi et al., 2015). Raman spectra of CM have also been used as a proxy for graphitization and aromatization of CM at high temperatures (Kuo et al., 2014, 2017; Oohashi et al., 2014; Hirono et al., 2015; Kaneki et al., 2016; Ito et al., 2017).

Some prior studies suggested that shear strain might affect the maturity of CM (e.g., Mastalerz et al., 1993; Kitamura et al., 2012). This phenomenon could be considered to be a mechanochemical effect, in that friction causes mechanical damage to molecular and crystal structures, which in turn enhances chemical reactions at relatively low temperatures (e.g., Lenhardt et al., 2010). Similar experimental investigations of this effect for the dehydroxylation reaction of illite, a common mineral in fault rocks, showed a decrease in activation energy (142.3 to 97.0 kJ mol^{-1}) during simulated earthquake slip (Hirono et al., 2013). However, such a mechanochemical effect on the maturation of CM has not been investigated. Here, we present quantitative experimental evidence of the mechanochemical effect on maturation of CM during faulting by using infrared (IR) and Raman spectroscopic analyses of sheared and intact CMs, and reconsider the use of the thermal maturity of CM as a proxy for the temperature of fault rocks during earthquake rupture.

4.2. Materials and methods

4.2.1. Characteristics of CMs used in this study

We prepared a mixture of 90 wt.% quartz (Wako Pure Chemical Industries) and 10 wt.% lignite (Mizunami city, Gifu Prefecture, Japan) as a simulated fault gouge. For analysis of the lignite at the molecular level, we determine the composition and thermal maturity by using an elemental analyzer (Flash EA 1112, Thermo Finnigan) and a py-GC/MS system (EGA/PY-3030D, Frontier Lab; GCMS-QP2010 SE, Shimadzu). The pyrolysate from the first phase of heating (100–400 °C) was dominated by toluene and phenols (Figure 4.1a), whereas that from the second phase (400–1000 °C) was dominated by benzene, toluene, phenols, and other aromatic compounds (Figure 4.1b). Thus, the lignite used in this study was typical immature kerogen composed of mostly aromatic compounds. Details of this methodological procedure of the py-GC/MS system are also described in Supporting Information Text S4.1.

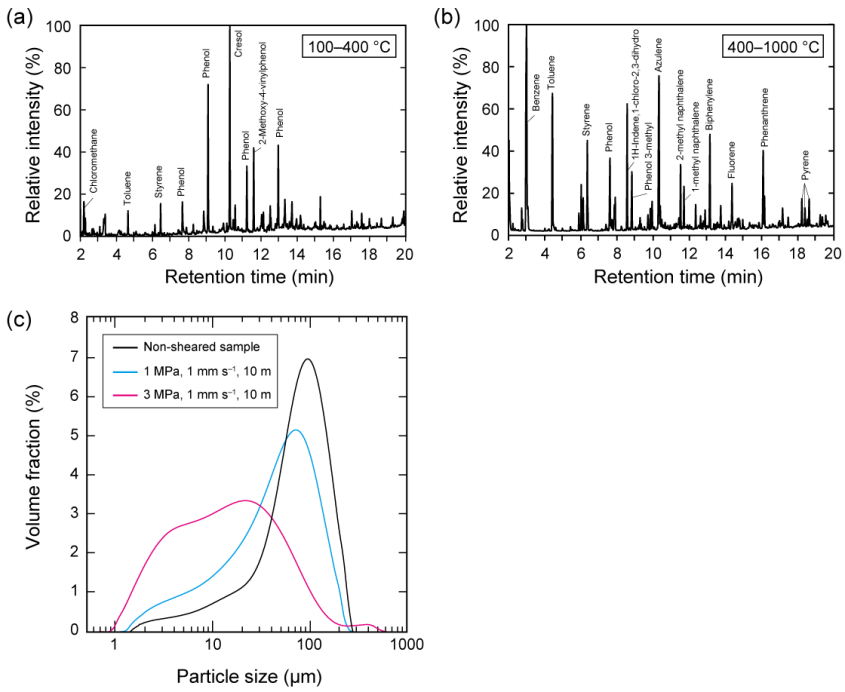

Figure 4.1. Pyrograms obtained by heating the non-sheared sample of lignite mixed with quartz from (a) 100 to 400 °C and (b) 400 to 1000 °C. (c) Particle size distributions of samples before and after friction experiments. Samples were sheared at a slip rate of 1 mm s^{-1} for a slip distance of 10 m under normal stresses of 1 and 3 MPa.

We used a van Krevelen diagram to evaluate the maturity of the lignite (van Krevelen, 1961). By using the elemental analyzer (Flash EA 1112, Thermo Finnigan), we determined that the lignite had O/C and H/C atomic ratios of 0.292 ± 0.013 and 0.431 ± 0.031, respectively, corresponding to an immature type-IV kerogen derived mainly from oxidized and charred wood (Hunt, 1995).

4.2.2. Experimental and analytical procedures

For investigating the mechanochemical effect on maturation of CM, we prepared the damaged mixture samples of CMs by using a rotary-shear friction apparatus and then heated the samples to demonstrate frictional heating during earthquakes. We applied IR and Raman spectroscopies to analyze the CMs before and after not only shearing but also heating on the molecule level.

4.2.3. Rotary-shear friction experiment

To replicate the mechanical damage caused by fault slip, samples were sheared in a rotary-shear friction apparatus (Hirose & Shimamoto, 2005). Approximately 0.8 mm-thick dry powdered sample was placed between the ends of two cylinders of gabbro (25 mm diameter). To prevent leaks during experiments, the sample and cylinders were sealed in a polytetrafluoroethylene sleeve. We performed the experiments at room humidity at an equivalent slip rate of 0.001 m s^{-1} (Hirose & Shimamoto, 2005) for 10 m of displacement at normal stresses of 1 and 3 MPa under air condition. After shearing, the innermost sample material (within 6 mm of the cylinder axes) was discarded because of the relatively small slip distance and low mechanical damage there. Temperature during the experiment was measured with a K-type thermocouple positioned in the stationary cylinder with its tip exposed between the sample and the cylinder about 9 mm from the cylinder axis.

Shear stress as a function of slip distance is shown in Supporting Information Figure

S4.1a. The temperature of the sample during shearing under 1.0 MPa normal stress increased from 29.3 to 32.5 °C (Supporting Information Figure S4.1b), thus indicating only a small temperature increase during shearing.

4.2.4. Heating experiment

To replicate heating during earthquake slip, we heated both non-sheared and sheared samples in a simultaneous thermogravimetry–differential scanning calorimetry apparatus (STA 449 C Jupiter balance, Netzsch) to temperatures from 100 to 1000 °C at 100 °C intervals. We used tube furnace apparatus to heat the samples to temperatures from 1100 to 1300 °C. Although the temperature rise during an earthquake is considered to several tens to several hundreds of degrees per second, we adopted heating rates of 50 and 15 °C min^{-1} for former and latter apparatuses, respectively, owing to their limitations. We conducted our experiment in an Ar gas atmosphere or under vacuum condition because the natural conditions for faults at depth would be anoxic (e.g., Wakita et al., 1980). Details of our heating experiments are described in Supporting Information Text S4.2.

4.2.5. IR spectroscopic analysis

IR spectra of CM show some absorbance peaks related to organochemical characteristics (e.g., Bent & Brown, 1961; Stuart, 2004); for example, a sharp peak at about 2930 cm^{-1} has been attributed to asymmetric aliphatic CH_2 stretching and another at about 1600 cm^{-1} to aromatic C=C stretching vibration.

We used a Fourier transform IR spectrometer (FT/IR-4700, Jasco Analytical Instruments, Inc.) equipped with an IR microscope (IRT-5200, Jasco Analytical Instruments, Inc.) to obtain IR absorption spectra of intact and sheared lignite samples before and after our heating experiments. To acquire one IR spectrum, 100 spectra were accumulated under the following measurement conditions: wavenumber resolution 4 cm^{-1}; wavenumber range 4000–

1000 cm^{-1}; and 40 x 40 μm^2 aperture size. IR absorption by a chemical species is dependent on both the concentration of the species and the sample thickness (according to the Lambert–Beer law); we kept sample thicknesses roughly consistent in our analyses. The intensities of the aliphatic CH_2 and aromatic C=C absorbance peaks (2930 and 1600 cm^{-1}, respectively) were determined by using PeakFit 3.0 software with a Voigt function (Systat Software, Inc.) after a linear baseline correction (3000–2800 cm^{-1} and 1800–1500 cm^{-1} for CH_2 and C=C peaks, respectively) before calculation of the CH_2/C=C intensity ratios ($I_{CH_2}/I_{C=C}$). Examples of peak decomposition in the IR spectrum are shown in Supporting Information Figure S4.2.

Because CM within sedimentary rock consists of heterogeneous cross-linked networks of organic macromolecules (e.g., Poutsma, 1987; Mathews & Chaffee, 2012), the number of spectroscopic analysis points is crucial to ensure that representative IR spectra are obtained. Moreover, there must be sufficient analyses to determine average intensities that are meaningful and directly related to the value of the standard deviation (*SD*):

$$SD = \sqrt{\frac{1}{n}\sum_{i=1}^{n}(x_i - \bar{x})^2} \tag{4.1}$$

where n is the number of observations in the sample, xi is the observed values of the sample, and $\bar{x}$ is the mean value of these observations. If $\sqrt{\sum_{i=1}^{n}(x_i - \bar{x})^2}$ equals to 0.1 (roughly corresponding to the obtained value in our Raman analysis), for n = 5 to 20, *SD*s drastically decrease from 0.141 and 0.071 (Supporting Information Figure S4.3). However, for n = 30, *SD* becomes sufficiently small to be 0.058, so we adopted the acquirement from 30 points for each sample.

4.2.6. Raman spectroscopic analysis

Raman spectra of CM generally include disordered (D, 1355–1380 cm^{-1}) and graphite (G, 1575–1620 cm^{-1}) bands (Tuinstra & Koenig, 1970). Recent studies have identified a complicated waveform in Raman spectra of CM, with four sub-peaks (D1, D2, D3, and D4) between about 1200 and 1650 cm^{-1} (e.g., Beyssac et al., 2002; Furuichi et al., 2015; Ito et al., 2017), and we followed their peak decomposition method in our analysis (Supporting

Information Figure S4.4).

We used a Raman microspectrometer equipped with a 532 nm laser (XploRa, Horiba Jobin Yvon, Inc.) for intact and sheared lignite samples before and after heating experiments. For each analysis point, the spectra were measured with a laser spot size of 5 μm, an exposure time of 10 s, and laser power of 0.01–0.13 mW on the targeted surface. Representative raw spectra are shown in Supporting Information Figure S4.5. The intensity of a Raman spectrum of CM is not simply a function of sample thickness, chemical species concentrations, and Raman scattering characteristics; it also depends on other analysis conditions (e.g., orientation of the sample). Thus, we manually normalized the intensities of spectra, after smoothing processing, for all samples to have similar heights. After a linear baseline correction (1000–1800 cm^{-1}) to remove fluorescence interference, the intensities of the four bands were evaluated by using PeakFit 3.0 software with a Voigt function (Systat Software, Inc.) and the I_{D1}/I_{D2} ratios were then calculated. As was the case for IR spectral analyses, Raman spectra were obtained at 30 points per sample, and the mean values and *SD*s were calculated.

4.3. Results

Shearing of our samples caused considerable reduction in particle size (Figure 4.1c), which we measured by the laser diffraction and scattering method with a particle-size analyzer (Mastersizer 2000, Malvern Instruments, Ltd). The modal particle size of the intact (not sheared) sample was 100.2 μm. The modal particle size of the sample sheared under 1 MPa normal stress was 71.0 μm. The sample sheared under 3 MPa normal stress showed a bimodal particle size distribution with peaks at 15.3 and 27.2 μm. These results indicate that frictional shearing caused comminution of the samples.

Figure 4.2 show representative IR and Raman spectra of CMs for each experimental condition. For all samples, the IR absorbance peaks of aliphatic CH_2 at 2930 cm^{-1} and of aromatic C=C at 1600 cm^{-1} became weak at temperatures greater than 600 °C and 800 °C, respectively (Figure 4.2a). The sheared samples showed slightly lower absorbance of aliphatic

CH_2 and distinctly lower absorbance of aromatic C=C than did the non-sheared samples. For all samples, Raman spectra acquired from room temperature to 300 °C showed the four bands to be weak to absent, whereas these bands were clearly evident at temperatures above 400 °C (Figure 4.2b). The intensity of the D1 band increased gradually with increasing temperature above 400 °C, whereas the intensity of the D2 band increased markedly from 400 to 500 °C and then changed little at higher temperatures. However, because we normalized the intensities of the Raman spectra that we obtained, we considered only the relative intensities of these bands.

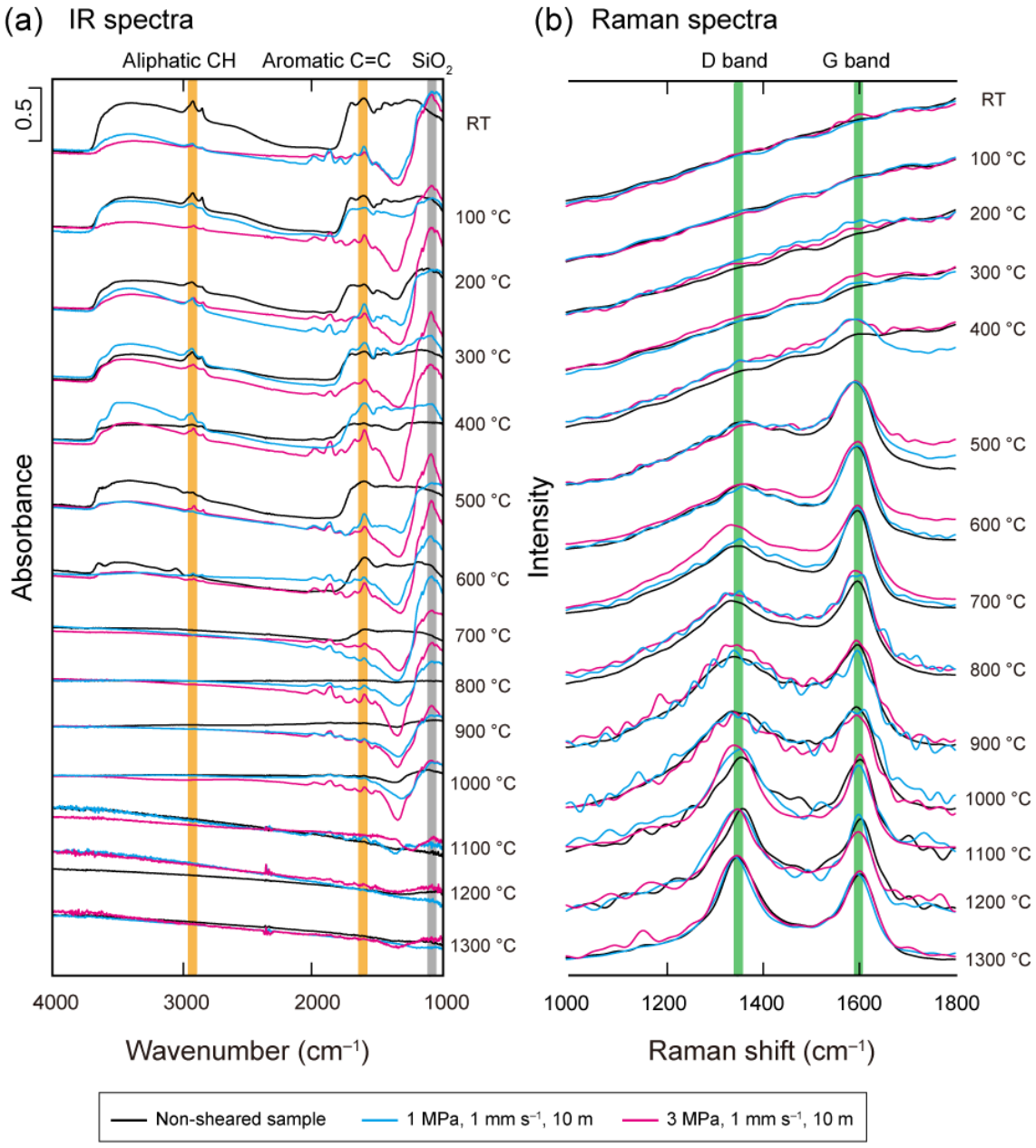

Figure 4.2. Spectra of products of heating experiments on samples of lignite mixed with quartz. (a) IR spectra and (b) Raman spectra. Slip rate, slip distance, and normal stresses as in Figure 4.1. RT = room temperature.

Figure 4.3 show calculated $I_{CH_2}/I_{C=C}$ and I_{D1}/I_{D2} ratios of CMs for each experimental condition. $I_{CH_2}/I_{C=C}$ ratios of CM are sensitive to high temperature, because the breakdown of aliphatic chains occurs at relatively low temperatures, whereas aromatic rings (C=C) are stable

at high temperatures (up to 800 °C). For example, immature kerogen from middle Holocene peat strata (Zhanjian, Guangdong Province, China) showed a decrease of the $I_{CH_2}/I_{C=C}$ ratio at high temperatures ≥350 °C (Zeng & Wu, 2007). However, our intact lignite samples showed no systematic change of $I_{CH_2}/I_{C=C}$ ratio with temperature (Figure 4.3a), although the $I_{CH_2}/I_{C=C}$ ratios of the sheared samples were lower than those of the non-sheared sample. The I_{D1}/I_{D2} ratio of CM is known to increase with increasing pyrolysis temperature (Wopenka & Pasteris, 1993; Li et al., 2006), as did the I_{D1}/I_{D2} ratios in all our samples (sheared and non-sheared) (Figure 4.3b), although the ratios in the sheared samples were higher. For example, at 800 °C, the I_{D1}/I_{D2} ratio for the non-sheared sample was 0.855 ± 0.020, whereas those for the two sheared samples were 0.892 ± 0.080 (sheared at 1 MPa normal stress) and 0.908 ± 0.072 (sheared at 3 MPa normal stress).

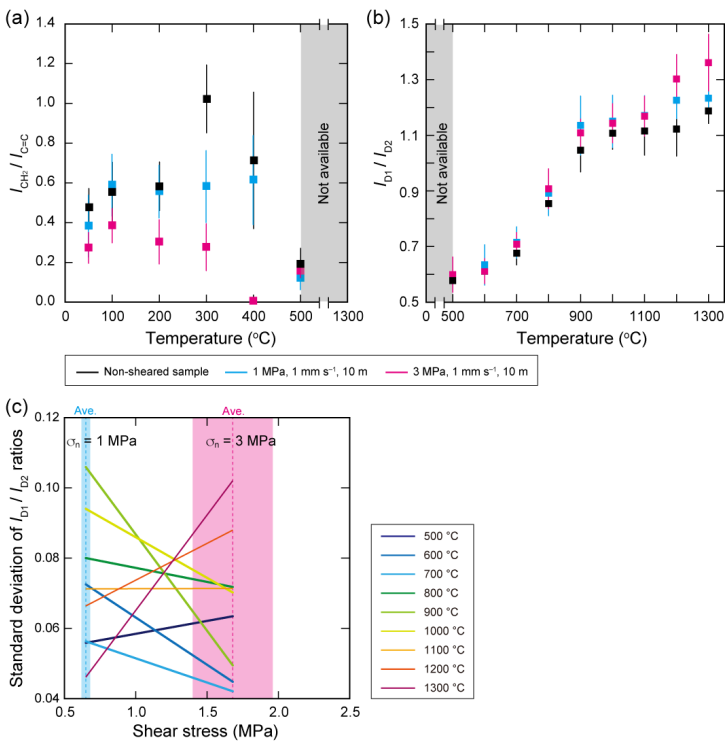

Figure 4.3. Temperature dependencies of IR and Raman spectral parameters (a) $I_{CH_2}/I_{C=C}$ ratios and (b) I_{D1}/I_{D2} ratios of products of heating experiments on samples of lignite mixed with quartz. (c) Relationship between standard deviation of I_{D1}/I_{D2} ratio and shear stress during friction experiments. Ave. = average shear stress.

4.4. Discussion and conclusions

CM is generally composed of massive aromatic nuclei linked by aliphatic hydrocarbon chains (e.g., Mathews & Chaffee, 2012). High temperatures of CM achieved on a geological timescale as a result of diagenesis, or achieved rapidly by frictional heating due to fault slip during earthquakes, induce pyrolysis, which breaks weak chemical bonds, releases volatiles, and causes carbonization, structural rearrangement, and aromatization (e.g., Lievens et al., 2013). The lignite we used in our experiments was composed of aromatic compounds linked by aliphatic chains (Figure 4.1a and b); our IR spectra showed that the aliphatic CH_2 (peak at 2930 cm^{-1}) disappeared at 600 °C (Figure 4.2a) as a result of thermal breakage of C–H chains. An increase of the I_{D1}/I_{D2} ratio above 600 °C on the Raman spectra (Figure 4.2b) likely reflects the survival during pyrolysis of the stronger C–C bonds within a graphitic structure.

Combustion including oxidation is another central reaction in CM for conflagration and power plant. However, in our study, CMs were heated under Ar gas or vacuum condition, so the oxidation never occurred. Although CMs suffered shear damage under air condition, small amount of temperature rise (Δ3.2 °C) by slow-rate friction might not activate the oxidation. CM adsorbs various gases including oxygen onto its surface (e.g., Wang et al., 2003; Fitzgerald et al., 2005), but the increase in O/C ratio was estimated 0.011 (Furuichi et al., 1974) that is less than the *SD* of 0.013 in our lignite. Thus we could ignore the effects by oxidation and adsorption of oxygen on our spectroscopic analysis.

The *SD*s of I_{D1}/I_{D2} ratios determined from Raman spectra of CM in pseudotachylytes have recently been trialed as a quantitative indicator of shear stress (Ito et al., 2017). To examine the applicability, we plotted values of *SD*s of I_{D1}/I_{D2} ratios as a function of average shear stress during friction experiments for each heating temperatures (Figure 4.3c). Because the shear stresses during the rotary-shear friction experiments conducted by Ito et al. (2017) fluctuated considerably, ranging from 1 to 11 MPa, they calculated average shear stress from total frictional work, slip duration, and equivalent slip rate. The shear stress during our friction experiments also fluctuated considerably, and we calculated average shear stress by following their method; under 1 MPa normal stress, average shear stress was 0.65 ± 0.03 MPa, and under

3 MPa normal stress that was 1.68 ± 0.28 MPa. For our lignite samples, the *SD*s of I_{D1}/I_{D2} ratios showed a general decrease with increasing shear stress at temperatures of ≤1000 °C, which is consistent with the results of Ito et al. (2017), but exhibited opposite trend at temperatures of ≥1100 °C (Figure 4.3c). If we calculate average shear stress from *SD*s by using their equation, calculated shear stress completely differs from average shear stress during our friction experiments at any temperatures of ≥500 °C: for example, with normal stress of 1 MPa and heating temperature of 1300 °C, acquired average shear stress was 0.65 ± 0.03 MPa whereas the average shear stress calculated by using their equation was 9.86 MPa. Thus, their determination of average shear stress is not applicable in our case. Another critical problem is the number of spectral analyses acquired for each of their samples (ranged from 26 to 30), and (as discussed in section 2.4) this number strongly affects the *SD*. Therefore, there are not only experimental but also theoretical uncertainties in the determination by Ito et al. (2017) of average shear stress as a function of the *SD* of I_{D1}/I_{D2} ratios determined from Raman spectral analyses.

On the basis of friction experiment results, Kitamura et al. (2012) attributed the maturation of coal not only to high temperatures but also to mechanochemical enhancement of chemical reactions in the CM. After heating, our lignite samples suffered higher shear stress and showed higher I_{D1}/I_{D2} ratios in Raman spectra (Figure 4.3b). Thus, our results clearly show that mechanochemical effects enhance various organochemical reactions. The breaking of aliphatic chains occurred not only at relatively low temperatures but also at room temperature (Figure 4.2a). High-rank coals such as bituminous and anthracite consist of relatively large cross-linked pericondensed aromatic and alicyclic components (Lazarov & Marinov, 1987) that ultimately form large aromatic sheets and stack the sheets, that is, graphitization (Nyathi et al., 2013), and recent friction experiments demonstrated shear-induced graphitization in a fault gouge (e.g., Oohashi et al., 2011; Kuo et al., 2014). However, lignite is the lowest rank of coal and consists of linked aromatic rings and cross-linked aliphatic side chains with a variety of functional groups such as alicyclic groups and carboxylic acid groups (e.g., Wender, 1976). Therefore, the main ogranochemical reaction in our lignite might be aromatization such as breaking of weak bonds and pyrolysis of functional groups with relatively low molecular weights.

Although the Raman spectral ratios of CM have been used as a proxy for temperature in several studies (e.g., Furuichi et al., 2015; Hirono et al., 2015; Kaneki et al., 2016), the mechanochemical effect should be taken into account in future estimates of the frictional heat generated during fault slip. For example, temperatures in an ancient megasplay fault in the Cretaceous Shimanto accretionary complex, Japan, were estimated by Kaneki et al. (2016) to have reached 600 °C on the basis of I_D/I_G ratios in Raman spectra of CM, and led them to conclude that there was 2.7–9.0 m of slip on the fault. However, had they taken the mechanochemical effect into consideration, the temperature reached and slip distance determined would have been 500 °C and 1.9–6.2 m, respectively.

The use of the thermal maturity of CM as a non-reversible temperature proxy for fault rock studies has considerable promise, but our study has clearly shown that physical damage caused by shearing during earthquake slip causes mechanochemical enhancement of organochemical reactions related to the aromatization of CM. To develop a more rigorous proxy for detecting heat signatures in faults, further spectroscopic analyses are needed of different types and grades of CM (e.g., other type of kerogen and higher grade bituminous coal), together with laboratory heating and friction experiments, and not only mechanochemical effects on the aromatization but also shear-induced graphitization must be taken into consideration.

References

Bent, R. & Brown, J.K. (1961). The infra-red spectra of macerals. *Fuel* **40**, 47–56.

Beyssac, O., Goffe, B., Chopin, C. & Rouzaud, J.N. (2002). Raman spectra of carbonaceous material in metasediments: A new geothermometer. *J. Metamorph. Geol.* **20**, 858–871.

Di Toro, G., Nielsen S. & Pennacchioni G. (2005). Earthquake rupture dynamics frozen in exhumed ancient faults. *Nature* **436**, 1009–1012.

Fitzgerald, J.E., Pan, Z., Sudibandriyo, M., Robinson Jr., R.L., Gasem, K.A.M. & Reeves, S. (2005). Adsorption of methane, nitrogen, carbon dioxide and their mixtures on wet Tiffany coal. *Fuel* **84**, 2351–2363.

Fulton, P.M. *et al*. (2013). Low coseismic friction on the Tohoku-oki fault determined from temperature measurements. *Science* **342**, 1214–1217.

Furuichi, H., Ujiie, K., Kouketsu, Y., Saito, T., Tsutsumi, A. & Wallis, S. (2015). Vitrinite reflectance and Raman spectra of carbonaceous material as indicators of frictional heating on faults: Constraints from friction experiments. *Earth Planet. Sci. Lett.* **424**, 191–200.

Furuichi, R., Kobayashi, H. & Okamoto, G. (1974). Oxygen adsorption on coals in the temperature range of 25–55 °C. *Bulletin of the Faculty of Engineering, Hokkaido University* **70**, 87–97 (in Japanese with English abstract).

Han, R., Shimamoto, T., Ando, J. & Ree, J. (2007). Seismic slip record in carbonate-bearing fault zones: An insight from high-velocity friction experiments on siderite gouge. *Geology* **35**, 1131–1134.

Hirono, T. *et al*. (2007). A chemical kinetic approach to estimate dynamic shear stress during the 1999 Taiwan Chi-Chi earthquake. *Geophys. Res. Lett.* **34**, L19308 (Correction, *Geophys. Res. Lett.* **35**, 2008).

Hirono, T. *et al*. (2008). Clay mineral reactions caused by frictional heating during an earthquake: An example from the Taiwan Chelungpu fault. *Geophys. Res. Lett.* **35**, L16303.

Hirono, T., Tanikawa, W., Honda, G., Kameda, J., Fukuda, J.-I. & Ishikawa, T. (2013). Importance of mechanochemical effects on fault slip behavior during earthquakes. *Geophys. Res. Lett.* **40**, 2988–2992.

Hirono, T., Maekawa, Y. & Yabuta, H. (2015). Investigation of the records of earthquake slip in carbonaceous materials from the Taiwan Chelungpu fault by means of infrared and Raman spectroscopies. *Geochem. Geophys. Geosyst.* **16**, 1233–1253.

Hirose, T. & Shimamoto, T. (2005). Growth of molten zone as a mechanism of slip weakening of simulated faults in gabbro during frictional melting. *J. Geophys. Res.* **110**, B05202.

Honda, G., Ishikawa, T., Hirono, T. & Mukoyoshi, H. (2011). Geochemical signals for determining the slip-weakening mechanism of an ancient megasplay fault in the

Shimanto accretionary complex. *Geophys. Res. Lett.* **38**, L06310.

Hunt, J. (1995). *Petroleum Geochemistry and Geology*. NY: W. H. Freeman.

Ishikawa, T. *et al*. (2008). Coseismic fluid–rock interactions at high temperatures in the Chelungpu fault. *Nat. Geosci.* **1**, 679–683.

Ito, K., Ujiie, K. & Kagi, H. (2017). Detection of increased heating and estimation of coseismic shear stress from Raman spectra of carbonaceous material in pseudotachylytes. *Geophys. Res. Lett.* **44**, 1749–1757.

Kaneki, S., Hirono, T., Mukoyoshi, H., Sampei, Y., & Ikehara, M. (2016). Organochemical characteristics of carbonaceous materials as indicators of heat recorded on an ancient plate subduction fault. *Geochem. Geophys. Geosyst.* **17**, 2855–2868.

Kano, Y., Mori, J., Fujio, R., Ito, H., Yanagidani, T., Nakao, S. & Ma, K. (2006). Heat signature on the Chelungpu fault associated with the 1999 Chi-Chi, Taiwan earthquake. *Geophys. Res. Lett.* **33**, L14306.

Kitamura, M., Mukoyoshi, H., Fulton, P.M. & Hirose, T. (2012). Coal maturation by frictional heat during rapid fault slip. *Geophys. Res. Lett.* **39**, L16302.

Kuo, L.-W., Li, H., Smith, S.A.F., Di Toro, G., Suppe, J., Song, S.-R., Nielsen, S., Sheu, H.-S. & Si, J. (2014). Gouge graphitization and dynamic fault weakening during the 2008 Mw 7.9 Wenchuan earthquake. *Geology* **42**, 47–50.

Kuo, L.-W. *et al*. (2017). Fault gouge graphitization as evidence of past seismic slip. *Geology* **45**, 979–982.

Lazarov L. & Marinov, S.P. (1987). Modelling the structure of a coking coal. *Fuel Process. Technol.* **15**, 411–422.

Lenhardt, J.M., Ong, M.T., Choe, R., Evenhuis, C.R., Martinez, T.J. & Craig, S.L. (2010). State by Mechanochemical Polymer Extension. *Science* **329**, 1057–1060.

Li, X., Hayashi, J. & Li, C.Z. (2006). FT-Raman spectroscopic study of the evolution of char structure during the pyrolysis of a Victorian brown coal. *Fuel* **85**, 1700–1707.

Lievens, C., Ci, D., Bai, Y., Ma, L., Zhang, R., Chen, J.Y., Gai, Q., Long, Y. & Guo, X. (2013). A study of slow pyrolysis of one low rank coal via pyrolysis-GC/MS, *Fuel Process.*

Technol. **116**, 85–93.

Maekawa, Y., Hirono, T., Yabuta, H., Mukoyoshi, H., Kitamura, M., Ikehara, M., Tanikawa, W. & Ishikawa, T. (2014). Estimation of slip parameters associated with frictional heating during the 1999 Taiwan Chi-Chi earthquake by vitrinite reflectance geothermometry. *Earth Planets Space* **66**, 28.

Mastalerz, M., Wilks, K.R., Bustin, R.M. & Ross, J.V. (1993). The effect of temperature, pressure and strain on carbonization in high-volatile bituminous and anthracitic coals. *Org. Geochem.* **20**, 315–325.

Mathews, J. & Chaffee, A.L. (2012). The molecular representations of coal–A review. *Fuel* **96**, 1–14.

Mishima, T. Hirono, T., Soh, W. & Song, S.-R. (2006). Thermal history estimation of the Taiwan Chelungpu fault using rock-magnetic methods. *Geophys. Res. Lett.* **33**, L23311.

Nyathi M.S., Clifford, C.B., & Schobert, H.H. (2013). Characterization of graphitic materials prepared from different rank, Pennsylvania anthracites. *Fuel* **114**, 244–250.

O'Hara, K. (2004). Paleo-stress estimates on ancient seismogenic faults based on frictional heating of coal. *Geophys. Res. Lett.* **31**, L03601.

O'Hara, K., Mizoguchi, K., Shimamoto, T. & Hower, J.C. (2006). Experimental frictional heating of coal gouge at seismic slip rate: Evidence for devolatilization and thermal pressurization of gouge fluids. *Tectonophysics* **424**, 109–118.

Oohashi, K., Hirose, T. & Shimamoto, T. (2011). Shear-induced graphitization of carbonaceous materials during seismic fault motion: Experiments and possible implications for fault mechanics. *J. Struct. Geol.* **33**, 1122–1134.

Oohashi, K., Han, R., Hirose, T., Shimamoto, T., Omura, K. & Matsuda, T. (2014). Carbon-forming reactions under a reducing atmosphere during seismic fault slip. *Geology* **42**, 787–790.

Poutsma, M.K. (1987). *A review of thermolysis studies of model compounds relevant to processing of coal*. Oak Ridge, Tenn: Oak Ridge Natl. Lab.

Sakaguchi A. *et al*. (2011). Seismic slip propagation to the updip end of plate boundary

subduction interface faults: Vitrinite reflectance geothermometry on Integrated Ocean Drilling Program NanTro SEIZE cores. *Geology* **39**, 395–398.

Savage, H.M., Polissar, P.J., Sheppard, R., Rowe, C.D. & Broadsky, E.E. (2014). Biomarkers heat up during earthquakes: New evidence of seismic slip in the rock record. *Geology* **42**, 99–102.

Stuart, B. (2004). *Infrared Spectrometry: Fundamentals and Applications*. Chichester, UK: John Wily.

Sweeney, J.J. & Burnham, A.K. (1990). Evaluation of a simple model of vitrinite reflectance based on chemical kinetics. *Am. Assoc. Petrol. Geol. Bull.* **74**, 1559–1570.

Tuinstra, F. & Koenig, J.L. (1970). Raman spectrum of graphite. *J. Chem. Phys.* **53**, 1126–1130.

Van Krevelen, D.W. (1961). *Coal*. Amsterdam: Elsevier.

Wakita, H., Nakamura, Y., Kita, I., Fujii, N. & Notsu, K. (1980). Hydrogen release: New indicator of fault activity. *Science* **210**, 188–190.

Wang, H., Dlugogorski, B.Z. & Kennedy, E.M. (2003). Coal oxidation at low temperatures: oxygen consumption, oxidation products, reaction mechanism and kinetic modelling. *Prog. Energy Combustion Sci.* **29**, 487–513.

Wender I. (1976). Catalytic synthesis of chemicals from coal. *Catal. Reviews–Sci. and Engineering* **14**, 97–129.

Wopenka, B. & Pasteris, J.D. (1993). Structural characterization of kerogens to granulite-facies graphite: Applicability of Raman microprobe spectroscopy. *Am. Mineral.* **78**, 533–557.

Zeng, Y. & Wu, C. (2007). Raman and infrared spectroscopic study of kerogen treated at elevated temperatures and pressures. *Fuel* **86**, 1192–1200.

Supporting information

Text S4.1.

Molecular compositions of intact lignite were determined by using a py-GC/MS system consisting of a pyrolyzer (EGA/PY-3030D, Frontier Lab) directly coupled to a gas chromatograph–mass spectrometer (GCMS-QP2010 SE, Shimadzu) equipped with an UltraALLOY-5 column (30 m length, 0.25 mm inner diameter, 0.25 μm film thickness). Approximately 3 mg of lignite was heated from 100 to 400 °C at 50 °C min^{-1} under vacuum, and gas-phase pyrolysates collected in a cryotrap were analyzed by GC/MS. The residue was again heated rapidly to 1000 °C, and the resulting pyrolysates were analyzed by GC/MS. For the CG/MS analysis, helium was used as the carrier gas at a flow rate of 1 mL min^{-1}, the split ratio was 50, and the injection temperature was 300 °C. The column temperature program was as follows: hold at 40 °C for 2 min, heat to 310 °C at 15 °C min^{-1}, and then hold at 310 °C for 10 min. The mass spectrometer was operated in electron ionization mode (70 eV, scan range m/z 35–600, scan interval 0.2 s), and the ion source temperature was kept at 230 °C. The pyrolysates were identified by comparing their mass spectra with those of standards in the library of the U.S. National Institute of Standards and Technology.

Text S4.2.

To reproduce frictional heating during earthquake slip, we used a thermogravimetry–differential scanning calorimetry apparatus (TG-DSC, STA 449 C Jupiter balance, Netzsch) to targeted temperatures of 100, 200, 300, 400, 500, 600, 700, 800, 900, and 1000 °C. Approximately 30 mg of both intact/sheared samples (90 wt.% quartz and 10 wt.% lignite) was placed in a covered $Pt_{90}Rh_{10}$ crucible, and then heated to the targeted temperatures at 50 °C min^{-1} heating rate under Argon gas flow. For heating sample to temperatures of 1100, 1200, and 1300 °C, we used tube furnace apparatus because TG-DSC can be used at temperatures of ≤1000 °C. Approximately 30 mg of sample was enclosed in a quartz tube (outer diameter, 8 mm; thickness, 1 mm; length, 25 cm) under vacuum ($\leq 10^{-5}$ Pa), and the tube was then inserted into tube furnace apparatus. Due to limitation of apparatus, heating rate was controlled to be 15 °C min^{-1}. For each heating experiment, we used different subsamples retrieved from intact/sheared samples. At all the experiments, we stopped to heat the samples immediately when the targeted temperature was achieved.

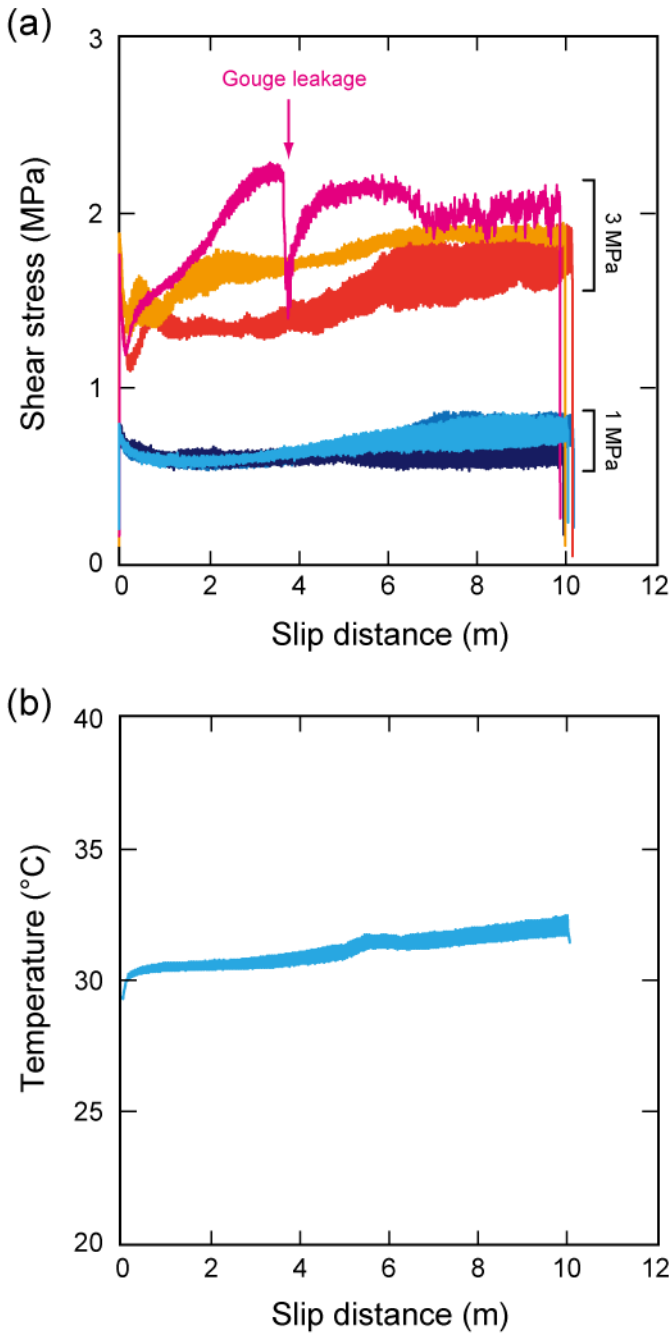

Figure S4.1. (a) Shear stress as a function of slip distance. Samples were sheared at a slip rate of 1 mm s^{-1} for a slip distance of 10 m under normal stresses of 1 and 3 MPa. The obtained steady-state shear stress in three experiments showed almost similar values for each normal stress condition. (b) Change in temperature as a function of slip distance during the friction experiment at 1 MPa normal stress.

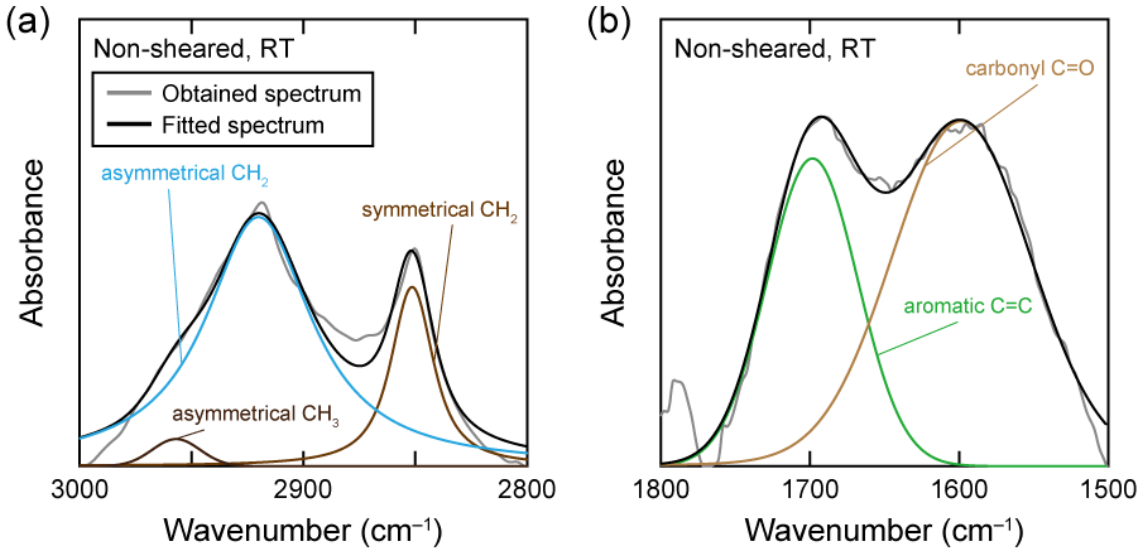

Figure S4.2. Representative IR spectra with decomposed peaks for determining intensities of (a) aliphatic CH_2 peak and (b) aromatic C=C peak.

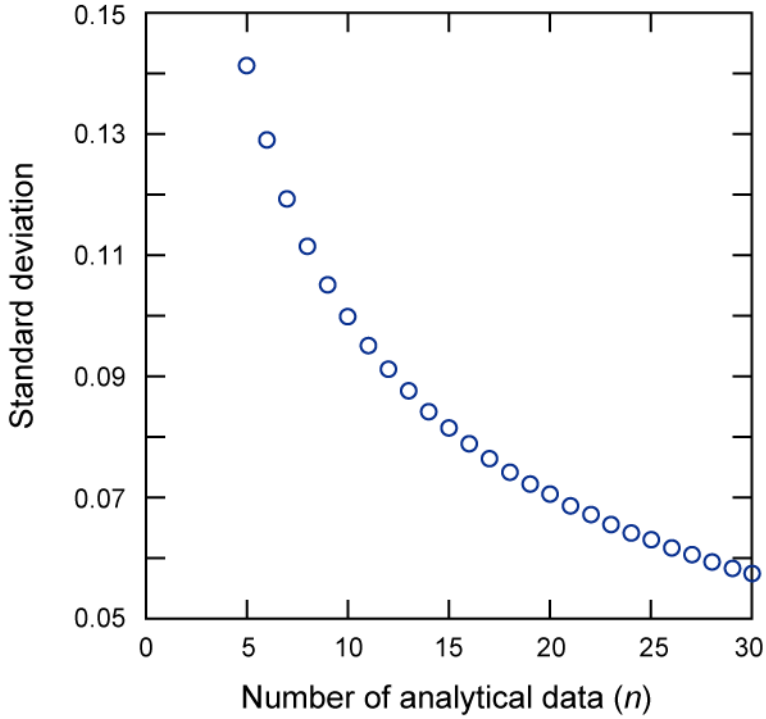

Figure S4.3. Standard deviation vs. number of analytical data per sample.

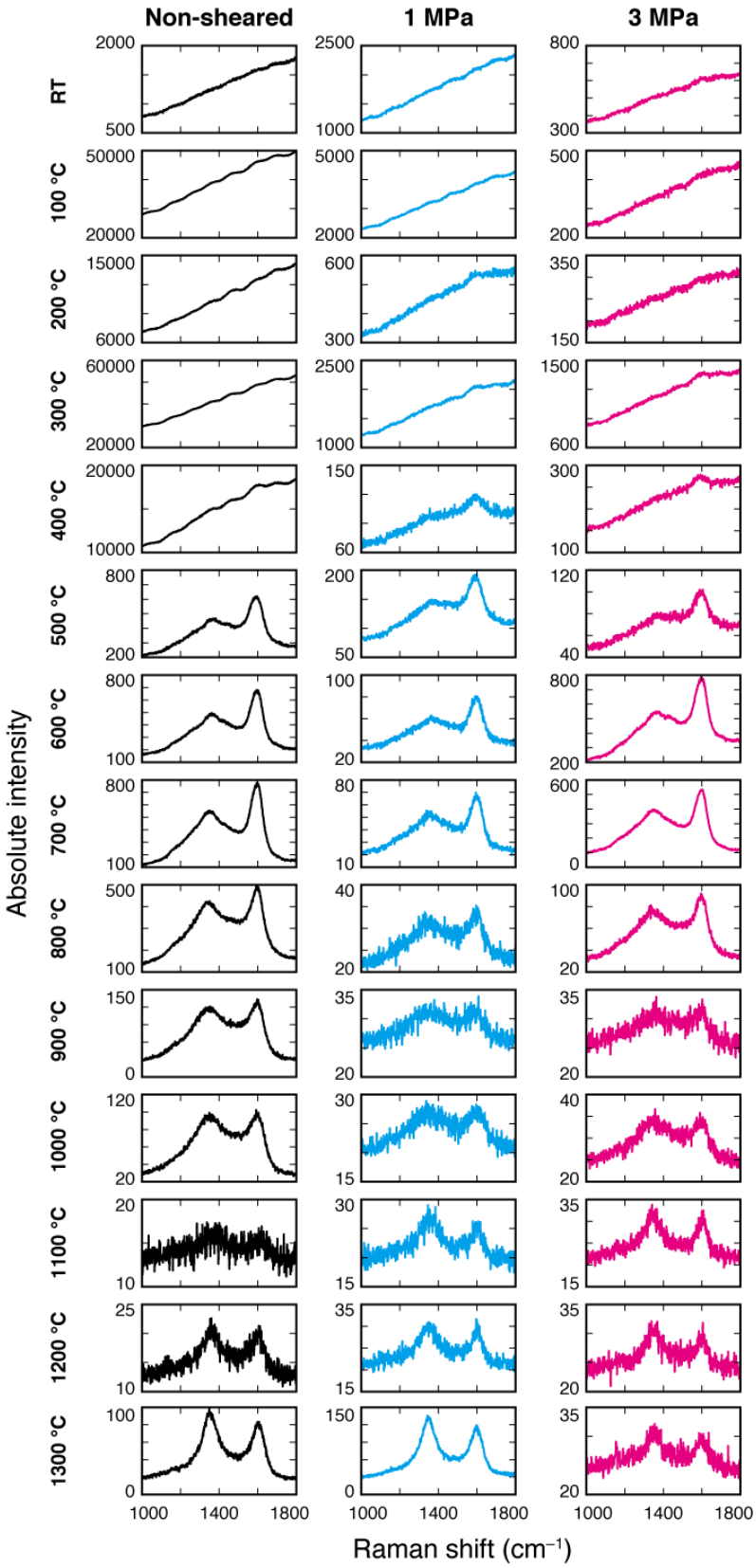

Figure S4.4. Representative raw Raman spectra for all experiments.

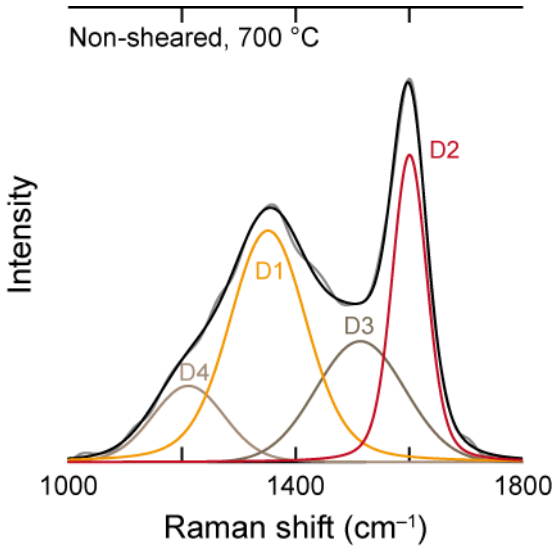

Figure S4.5. Representative Raman spectrum with decomposed peaks for determining intensities of D1 and D2 peaks.

Chapter 5

Kinetic effect of heating rate on the thermal maturity of carbonaceous material as an indicator of frictional heat during earthquakes

Abstract

Because the maximum temperature reached in the slip zone is significant information for understanding slip behaviors during an earthquake, the maturity of carbonaceous material (CM) is widely used as a proxy for detecting frictional heat recorded by fault rocks. The degree of maturation of CM is controlled not only by maximum temperature but also by the heating rate. Nevertheless, maximum slip zone temperature has been estimated previously by comparing the maturity of CM in natural fault rocks with that of synthetic products heated at rates of about 1 °C s–1, even though this rate is much lower than the actual heating rate during an earthquake. In this study, we investigated the kinetic effect of the heating rate on the CM maturation process by performing organochemical analyses of CM heated at slow (1 °C s^{-1}) and fast (100 °C s^{-1}) rates. The results clearly showed that a higher heating rate can inhibit the maturation reactions of CM: for example, extinction of aliphatic hydrocarbon chains occurred at 600 °C at a heating rate of 1 °C s^{-1} and at 900 °C at a heating rate of 100 °C s^{-1}. However, shear-enhanced mechanochemical effects can also promote CM maturation reactions and may offset the effect of a high heating rate. We should thus consider simultaneously the effects of both heating rate and mechanochemistry on CM maturation to establish CM as a more rigorous proxy for frictional heat recorded by fault rocks and for estimating slip behaviors during earthquake.

5.1. Introduction

Frictional heat generated in fault zones constitutes the largest part of the total seismic energy budget during an earthquake (e.g., Chester et al., 2005), and it triggers several kinds of fault-weakening mechanisms, including thermal pressurization (Sibson, 1973) and melt lubrication (Hirose & Shimamoto, 2005), which can strongly affect earthquake energetics and fault slip behaviors. Because the progression of such mechanisms is closely dependent on the amount of heat produced by slip, to understand fault slip behaviors during earthquakes it is crucial to estimate the maximum temperature recorded by the fault rocks.

Several temperature proxies have been proposed as indicators of frictional heat recorded

by fault rocks (Rowe & Griffith, 2015). These include pseudotachylyte formation (e.g., Cowan, 1999; Di Toro et al., 2005), mineral transformations (e.g., Hirono et al., 2007; Mishima et al., 2009; Kameda et al., 2011; Evans et al., 2014), thermal decomposition of carbonate minerals (e.g., Han et al., 2007; Oohashi et al. 2014), dehydration and dehydroxylation of clay minerals (e.g., Hirono et al., 2008; Schleicher et al., 2015), and anomalies in fluid-mobile trace element concentrations and strontium isotope ratios (e.g., Ishikawa et al., 2008; Honda et al., 2011). In particular, the thermal maturity of carbonaceous material (CM) has received considerable attention as a new temperature proxy (e.g., Savage et al., 2014; Hirono et al., 2015; Kaneki et al., 2016; Rabinowitz et al., 2017) because the organochemical characteristics of CM, including its elemental compositions and molecular structures, change irreversibly with increasing temperature (e.g., Beyssac et al., 2002). The frictional heat recorded by CM in both natural and experimental fault rocks has been investigated by spectroscopic analyses (e.g., Furuichi et al., 2015; Hirono et al., 2015; Kaneki et al., 2016, 2018; Ito et al., 2017; Kouketsu et al., 2017; Kuo et al., 2017) and by determining elemental compositions (Kaneki et al., 2016), biomarker indexes (Polissar et al., 2011; Savage et al., 2014; Sheppard et al., 2015; Rabinowitz et al., 2017), and vitrinite reflectance (e.g., O'Hara, 2004; Sakaguchi et al., 2011; Kitamura et al., 2012; Maekawa et al., 2014; Hamada et al., 2015). Several studies have succeeded in inferring slip behaviors on natural faults during past earthquakes from estimations of maximum temperatures recorded by CM (Savage et al., 2014; Hirono et al., 2015; Kaneki et al., 2016; Mukoyoshi et al., 2018).

Maturation of CM is accompanied by the release of various volatile organic components (e.g., aliphatics, aromatics), resulting in the formation of a solid residue with extremely high carbon content (e.g., Spokas, 2010). This devolatilization process can be strongly affected not only by maximum temperature but also by other factors such as a change in reactivity due to shear damage (mechanochemical effect) and the kinetic effect of the heating rate (e.g., Alexander et al., 1986; Kitamura et al., 2012). Recently, Kaneki et al. (2018) experimentally demonstrated that shear-enhanced mechanochemical effects can promote various organochemical reactions of CM at relatively low temperature and suggested that maximum

temperatures estimated in the previous studies might be overestimates. Although it is known that higher heating rates generally lead to higher pyrolytic temperatures of CM (e.g., Alexander et al., 1986; Schenk et al., 1990; Huang & Otten, 1998; Burnham & Braun, 1999; Lievens et al., 2013), however, quantitative evaluation of the kinetic effect of heating rate on the CM maturation process during earthquakes remains unknown. Furthermore, several recent estimates of maximum temperatures are based on heating experiments conducted only at slow heating rates of about 1 °C s^{-1} (Hirono et al., 2015; Kaneki et al., 2016; Mukoyoshi et al., 2018). For example, Kaneki et al. (2016) inferred maximum temperatures and fault slip distances in the CM-bearing slip zone of an ancient plate-subduction fault developed in Kure Mélange, Shikoku, Japan (Figure 5.1), to be 500–600 °C and 2–9 m, respectively, from the results of heating experiments on host-rock CM conducted using a heating rate of 50 °C min^{-1} (approximately 1 °C s^{-1}). This rate is much lower than typical heating rates during earthquake slip (several tens to several hundreds of degrees per second); thus, these estimated temperatures and fault slip behaviors may include uncertainties due to the kinetic effect of heating rate.

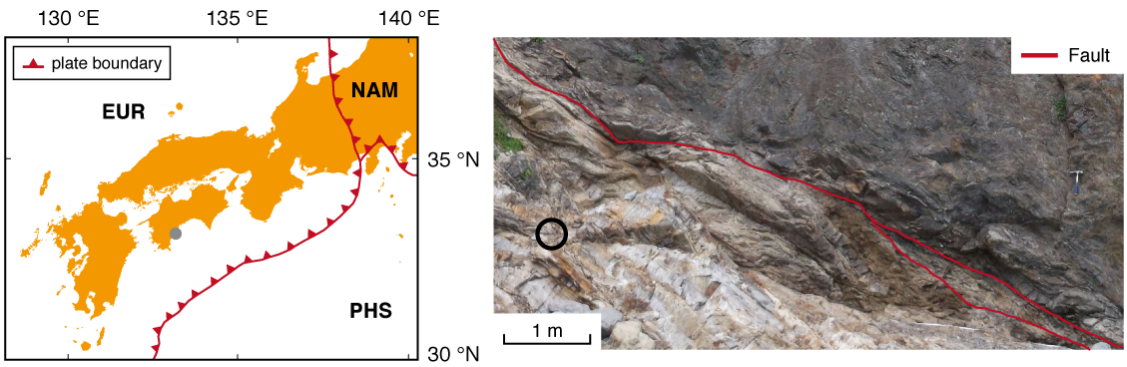

Figure 5.1. Example of a CM-bearing fault. Location (left) and photograph (right) of an ancient plate-subduction fault developed in the Kure Mélange, Shikoku, Japan. The sampling point of CM-bearing non-deformed shale is shown by the black circle on the photograph of the outcrop. *EUR* Eurasia plate, *NAM* North American plate, *PHS* Philippine Sea plate.

In this study, we quantitatively investigated the kinetic effect of heating rate on the

thermal maturation of CM by using infrared (IR) and Raman spectrometry and pyrolysis-gas chromatography-mass spectrometry (py-GC/MS) in conjunction with slow- and fast-heating experiments. On the basis of our results, we show that the effect of heating rate on thermal maturation of CM has implications for the use of CM maturity as a proxy for frictional heat. We consider information about this effect to be crucial for establishing a more rigorous fault geothermometer and for estimating slip behaviors of past earthquakes.

5.2. Materials and methods

5.2.1. Heating experiment

To investigate the kinetic effect of heating rate on CM maturation, we collected CM-bearing bulk-rock samples from non-deformed shale in the Cretaceous Nonokawa Formation, in the Shimanto accretionary complex, which crops out along the coast at Kure, Tosa Town, Japan (Mukoyosh et al., 2006) (Figure 5.1). After extracting pure CM from the bulk samples by chemical treatment (HCl–HF method; see Kaneki et al., 2016 for details), we used a thermogravimetry–differential scanning calorimeter apparatus (STA 449 C Jupiter balance, Netzsch) for our slow-heating experiments. About 30 mg of the CM was placed in a covered $Pt_{90}Rh_{10}$ crucible and heated under Ar gas flow at a rate of 50 °C min^{-1} (approximately 1 °C s^{-1}) from an initial temperature of 50 °C to target temperatures from 100–1000 °C at 100 °C intervals.

For the fast-heating experiments, we used a tube furnace to heat each CM sample. About 10 mg of sample was enclosed in a quartz tube (outer diameter, 8 mm; thickness, 1 mm; length, 25 cm) under vacuum (≤10 Pa), and then the tube was inserted into the tube furnace apparatus, which had been preheated to the target temperature (100–1000 °C at 100 °C intervals), for 10 s. We numerically simulated the heating rates during the experiments by adopting a CM particle diameter of 100 μm (determined from scanning electron microscope observations) and thermal diffusivities of 1.6 x 10^{-7} and 8.7 x 10^{-7} m^2 s^{-1} for CM and silica glass, respectively (Gustafsson et al. 1979; Turian et al. 1991). Then, we simulated the time–

temperature and time–heating rate relationships for a CM particle with these thermophysical properties during the fast-heating experiments (Supporting Information Figure S5.1). The simulated temperature profiles indicate that the heating rate increases as the target temperature increases, and the maximum heating rate that can be achieved is ≥100 °C s^{-1} for all target temperatures except 100 °C (for which 50 °C s^{-1} is the maximum rate) (Supporting Information Figure S5.1). Hereafter, therefore, we refer to the slow- and fast-heating rates during the heating experiments as 1 °C s^{-1} and 100 °C s^{-1}, respectively. We stopped the heating as soon as the targeted temperature was achieved.

5.2.2. Spectroscopic analysis

To investigate the chemical structures of CM, we conducted IR and Raman spectrometry on powdered CM samples. IR spectra of CM exhibit various peaks that correspond to organic and inorganic chemical bonds (e.g., Stuart, 2004). These include an O–H stretching band at around 3400 cm^{-1}; a sharp aromatic C–H band at 3050 cm^{-1}; aliphatic hydrocarbon bands at 2960 cm^{-1} (asymmetrical CH_3 stretching), 2930 cm^{-1} (asymmetrical CH_2 stretching), and 2860 cm^{-1} (symmetrical CH_2 stretching); a C=O stretching band at 1680 cm^{-1}; an aromatic ring C=C stretching band at 1600 cm^{-1}; and weak aliphatic hydrocarbon bending bands at 1455 cm^{-1} (asymmetrical CH_3 bending) and 1375 cm^{-1} (symmetrical CH_2 bending). We followed the methods of Kaneki et al. (2016) to obtain our IR spectra. We used a Fourier transform IR spectrometer (FT/IR-4700, Jasco Inc.) equipped with an IR microscope (IRT-5200, Jasco Inc.) to obtain IR absorbance spectra of CM retrieved from the shale and from the products of heating at 1 °C s^{-1} or 100 °C s^{-1}. The samples were placed on a CaF_2 plate and then hand-pressed to prevent saturation of the IR spectra. Before the measurements, plates and samples were dried in an oven at 50 °C for several hours. To acquire one IR spectrum, 100 spectra were accumulated with a wavenumber resolution of 4 cm^{-1}, a wavenumber range of 4000–1000 cm^{-1}, and an aperture size of 50 x 50 μm^2. Background intensities of the IR spectra were eliminated by measuring a blank CaF_2 plate.

Raman spectra of CM show significant peaks at 1355–1380 and 1575–1620 cm^{-1}, which are known as disordered (D) and graphite (G) bands, respectively (Tuinstra and Koenig, 1970). Several spectral parameters have been used to evaluate the maturity of CM in metamorphic rocks (e.g., Beyssac et al., 2002; Aoya et al., 2010; Kouketsu et al., 2014; Nakamura et al., 2015) and fault rocks (e.g., Hirono et al., 2015; Kaneki et al., 2016; Kouketsu et al., 2017; Kuo et al., 2017). We followed the methods of Kaneki et al. (2016) to acquire our Raman spectra and spectral parameters. We used a Raman microspectrometer (XploRA, Horiba Jobin Yvon Inc.) equipped with a laser (532 nm) to obtain Raman spectra of CM powder derived from the shale and from the samples heated at 1 °C s^{-1} and 100 °C s^{-1}. Before the measurements, samples were dried in an oven at 50 °C for several hours. Although the graphitic structure of CM has a crystallographic orientation (c-axis orientation), we did not control sample orientation during our spectral measurements because the orientation is unlikely to affect the Raman spectral features (Aoya et al., 2010). We used an exposure time of 10 s and a laser power of 0.09–0.11 mW to obtain spectra from the targeted surfaces to avoid thermal damage to the powder samples. Because Raman spectra obtained from the grain boundaries of CM particles might differ from those obtained from the body of CM particles (Tuinstra and Koenig, 1970), we adopted a laser spot size of 5 μm as sufficiently smaller than the average CM particle size (approximately 100 μm). We then used PeakFit 3.0 software (Systat Software Inc.) to fit the D and G bands to the acquired spectra after a linear baseline correction of 1000–1800 cm^{-1} (Supporting Information Figure S5.2). We determined the intensities of both bands. To compare the spectral features among the acquired Raman spectra, we normalized the spectra so that the height of the strongest peak of each spectrum was the same among the spectra being compared. Ten spectra were obtained from each sample (one spectrum per CM particle), and the mean values and standard deviations of the intensity ratios of the D and G bands (I_D/I_G) were calculated. All of the calculated I_D/I_G ratios with their standard deviations are summarized in Supporting Information Table S5.1.

5.2.3. Py-GC/MS

To analyze the composition of gases released from the starting samples and from the samples that had been heated at 1 °C s^{-1} and 100 °C s^{-1}, we followed the methods of Kaneki et al. (2016). We used a py-GC/MS system consisting of a model EGA/PY-3030D pyrolyzer (Frontier Lab) and a model GCMS-QP2010 SE GC/MS (Shimadzu) with an UltraALLOY-5 column. About 1 mg of sample was pyrolyzed at 1000 °C for 1 min under vacuum (≤2 Pa), and chromatographs and chemical compositions of the released gas were then analyzed. First, the intensities of the chromatographs were normalized by the weight of the analyzed samples, and then the intensity ratios of toluene to benzene ($I_{toluene}/I_{benzene}$) were determined. All of the calculated $I_{toluene}/I_{benzene}$ ratios are summarized in Supporting Information Table S5.1.

5.3. Results

5.3.1. Spectroscopic characteristics

The spectra of CM from the shale (starting material) showed sharp absorbance peaks for the aliphatic C–H (2960, 2930, 2860, 1455, and 1375 cm^{-1}), aromatic C–H (3050 cm^{-1}), and C=C bonds (1600 cm^{-1}) (Figure 5.2). In the spectra of samples heated at 1 °C s^{-1}, the absorbance peaks of the aliphatic C–H bonds and the aromatic C–H bond became weak at 600 °C and disappeared at 700 °C, and the absorbance peaks of the aromatic C=C bond became weak at 700 °C and disappeared at 800 °C (Figure 5.2a). In the spectra of samples heated at 100 °C s^{-1}, the absorbance peaks of the aliphatic C–H bonds and the aromatic C–H bond became weak at 800 °C and disappeared at 900 and 1000 °C, respectively, and the absorbance peaks of the aromatic C=C bond became weak at 900 °C and disappeared at 1000 °C (Figure 5.2b).

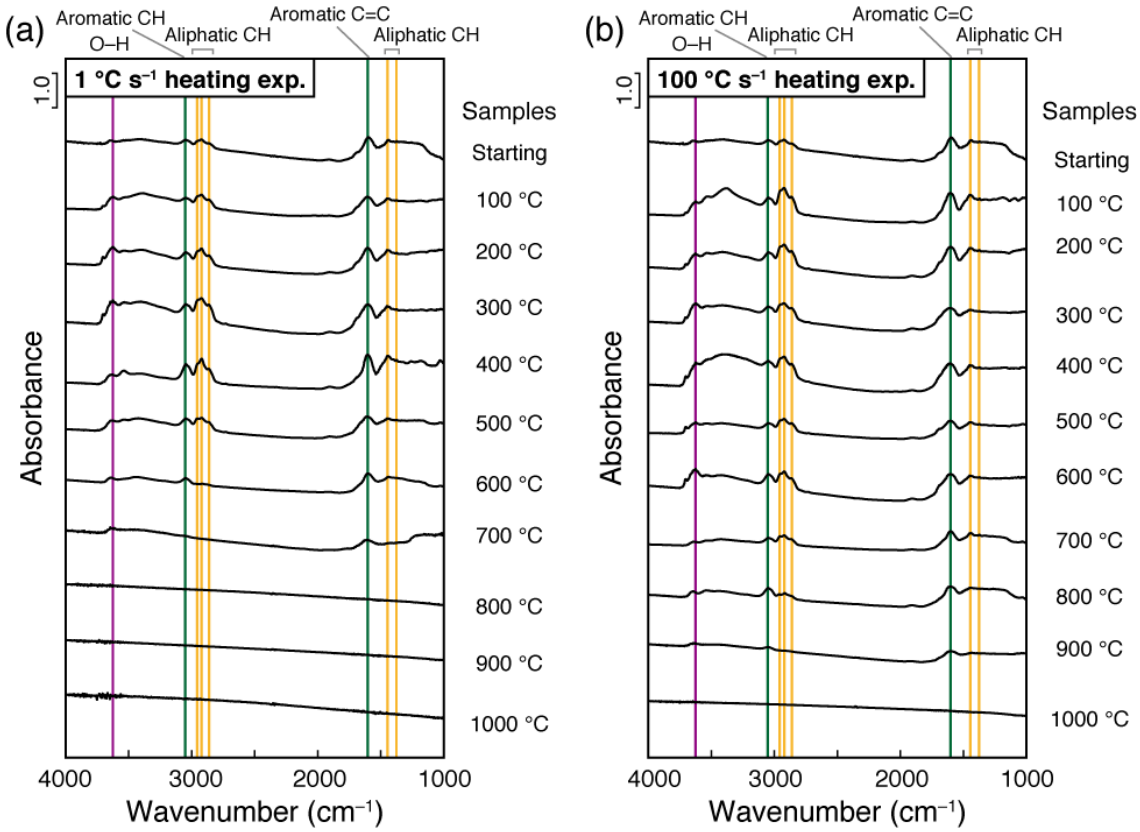

Figure 5.2. Representative IR spectra of the analyzed CM. IR spectra of CM from shale and from products heated at a rate of (a) 1 °C s^{-1} or (b) 100 °C s^{-1}. *exp.* experiment.

The Raman spectra of all of the analyzed samples showed distinct D and G band peaks, and the intensity of the D band relative to that of the G band increased as the target temperature increased (Figure 5.3). The I_D/I_G ratios of the samples heated at 1 °C s^{-1} increased markedly at ≥600 °C, whereas those of samples heated at 100 °C s^{-1} started to increase at ≥900 °C (Figure 5.4).

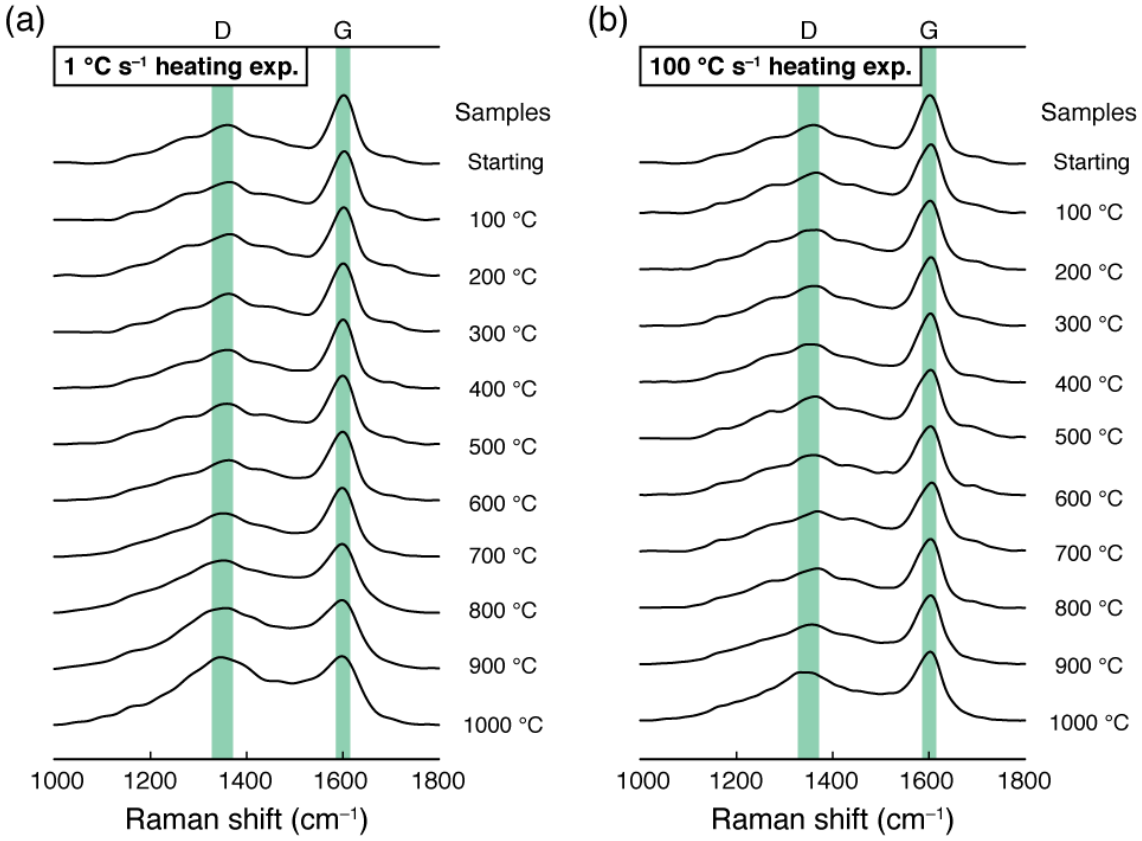

Figure 5.3. Representative Raman spectra of the analyzed CM. Raman spectra of CM from shale and from products heated at a rate of (a) 1 °C s^{-1} or (b) 100 °C s^{-1}. *exp.* experiment.

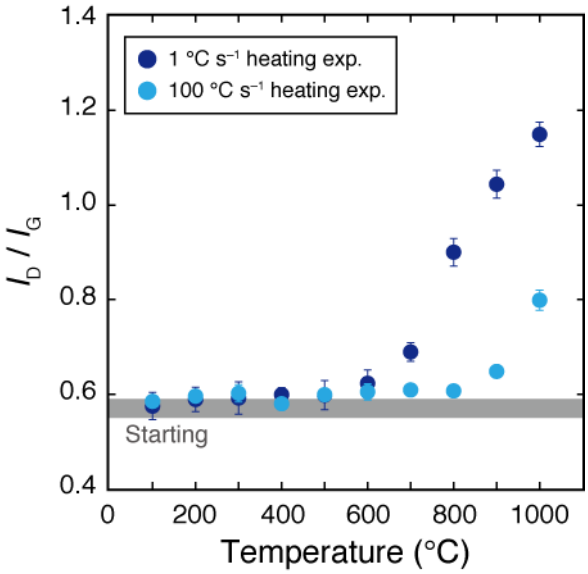

Figure 5.4. Temperature dependence of the I_D/I_G ratios of the analyzed CM. Bars show standard deviations. *exp.* experiment.

5.3.2. Py-GC/MS

Chromatographs for the CM sample from shale and for the products of the heating experiments included clear peaks of various aromatic compounds, and the samples were especially rich in benzene and toluene (Figure 5.5). The chromatographs for the products of the heating experiments showed a systematic decrease in peak intensities as the target temperature increased. Intensities of the benzene and toluene peaks of CM sample heated at 1 °C s^{-1} decreased markedly at 500 °C and approached zero at 700 °C (benzene) and 600 °C (toluene). In contrast, for the CM sample heated at 100 °C s^{-1}, chromatograph peak intensities started to decrease at 800 °C and approached zero at 1000 °C. The $I_{toluene}/I_{benzene}$ ratios of the CM sample heated at 1 °C s^{-1} started to decrease at 500 °C, whereas the ratios of samples heated at 100 °C s^{-1} showed a sudden decrease above 800 °C (Figure 5.6). The $I_{toluene}/I_{benzene}$ ratios in samples heated at 1 °C s^{-1} to ≥700 °C and in those heated at 100 °C s^{-1} to 1000 °C could not be determined because of the extinction of the toluene and benzene peaks on those chromatographs.

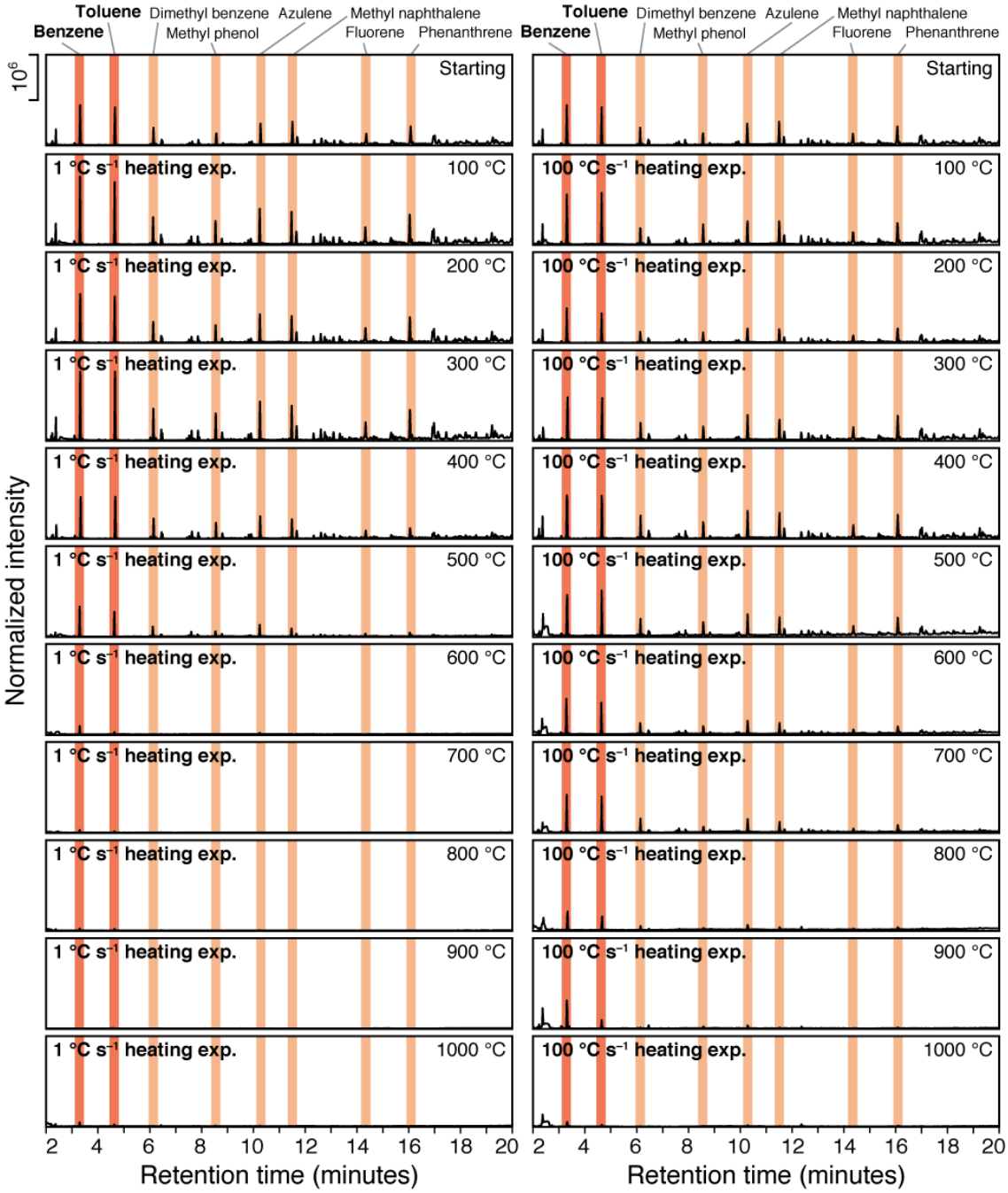

Figure 5.5. Gas chromatographs of the analyzed CM. The two chromatographs at the top of each column show the composition of gas released from the starting CM. The lower 20 chromatographs show the compositions of gas released from the products heated at 1 °C s^{-1} (left column) and 100 °C s^{-1} (right column). *exp.* experiment.

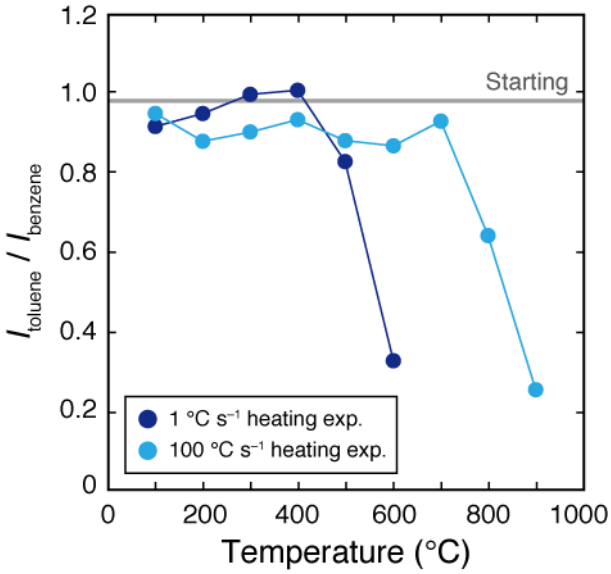

Figure 5.6. Temperature dependence of the $I_{toluene}/I_{benzene}$ ratios of the analyzed CM. The ratios of the products heated to ≥700 °C at 1 °C s^{-1} and to 1000 °C at 100 °C s^{-1} are not available owing to extinction of the toluene and benzene peaks. *exp.* experiment.

5.4. Discussion and conclusions

The py-GC/MS chromatographs revealed that the dominant components of the analyzed CM samples were benzene and toluene, and the amounts of these compounds decreased as the target temperature increased (Figure 5.5). The presence of toluene or phenol, which have aliphatic C–H or O–H bonds in their molecular structures, clearly indicates that the CM from shale was not derived from C-H-O-rich fluid at high temperature (≥500 °C) because such depositional CM is almost fully graphitized (e.g., Luque et al., 2009). In samples heated at 1 °C s^{-1} and 100 °C s^{-1}, the chromatographic peak of toluene disappeared (Figure 5.5), and extinction of the aliphatic C–H absorbance peaks was observed on the IR spectra (Figure 5.2), at 600 and 900 °C, respectively. This result clearly indicates that toluene dominantly controlled the amount of aliphatic C–H chain in the samples. Furthermore, the almost simultaneous disappearance of the chromatographic peak for benzene and the absorbance peak of the aromatic C=C bond at 700–800 °C and 1000 °C in the samples heated at 1 °C s^{-1} and 100 °C s^{-1}, respectively (Figure 5.2 and 5.5), suggests that benzene was the main contributor to the aromatic C=C absorbance

peaks on the IR spectra. The I_D/I_G ratios of the Raman spectra for the products heated at 1 °C s^{-1} and 100 °C s^{-1} began to increase at ≥600 and ≥900 °C, respectively (Figure 5.4). This result is well consistent with the findings of several prior studies that showed I_D/I_G ratios increased when intact CM was exposed to high temperatures of several hundreds of degrees Celsius by heating or friction experiments (e.g., Furuichi et al., 2015; Hirono et al., 2015; Kaneki et al., 2016, 2018; Ito et al., 2017). In these temperature ranges, no significant change in the molecular compounds in gases released from the heating products was observed except for a small decrease in the chromatographic peak of benzene (Figure 5.5). This result suggests that the changes in the I_D/I_G ratios are possibly attributable to pyrolysis of residual benzene with relatively strong bonds within the graphitic sheets accompanied by the formation of a disordered structure as a result of pyrolytic rearrangement. The abrupt decreases of the $I_{toluene}/I_{benzene}$ ratios at ≥500 and ≥800 °C in the products heated at 1 °C s^{-1} and 100 °C s^{-1}, respectively, might be due to the difference in the pyrolytic temperatures of benzene and toluene (Figure 5.6).

On the basis of these results, we inferred that the dominant maturation process controlling the changes in the organochemical characteristics of the starting CM during the heating experiments was the thermal decomposition of benzene and toluene, which resulted in the extinction of absorbance peaks in the IR spectra at higher temperatures, and the subsequent rearrangement of residual aromatic nuclei, which in turn increased the I_D/I_G ratios of the Raman spectra. Although Kaneki et al. (2016) attributed changes in the characteristics of IR and Raman spectra of heated CM to the thermal decomposition of toluene and the growth of aromatic rings, our series of organochemical analyses, including py-GC/MS analyses, revealed that thermal decomposition not only of toluene but also of benzene, along with subsequent structural rearrangement that increased the I_D/I_G ratios, may have played a significant role in maturation process of our CM at high temperature.

Although our CM heating experiments were conducted under dry conditions, the in-situ environment of natural fault rocks is usually water-saturated. Water saturation may affect the CM maturation process by providing an exogenous source of hydrogen (e.g., Lewan, 1997).

However, this hydrothermal effect is reported to appear only after a long reaction time of ≥70 h at temperatures of ≥330 °C (Lewan, 1997). Because our heating experiments were completed within 20 minutes, we can ignore the effect of water saturation.

The I_D/I_G ratio of Raman spectra has long been believed to decrease with increasing CM maturity (e.g., Beyssac et al., 2002; Kuo et al., 2017), whereas we observed a completely opposite trend in our results (Figure 5.4). However, recent friction and heating experiments conducted with pure CM or CM-bearing samples have demonstrated increases in the I_D/I_G ratios of CM with increasing temperature (e.g., Furuichi et al., 2015; Hirono et al., 2015; Kaneki et al., 2016, 2018; Ito et al., 2017). Furthermore, Mukoyoshi et al. (2018) reported an increase of the I_D/I_G ratios of CM in a natural pseudotachylyte-bearing slip zone relative to the ratios in host-rock samples. These contradictory results might be explained by heterogeneity of the initial condition of the CMs among these studies. For example, Kuo et al. (2017) obtained lower I_D/I_G ratios for anthracite samples in a high-velocity friction experiment, whereas Furuichi et al. (2015) reported an increase in the I_D/I_G ratios of brown coal in a similar friction experiment. If it is assumed that the direction of change of the I_D/I_G ratios of Raman spectra with increasing temperature depends on the initial maturity of the starting CM (e.g., Kouketsu et al., 2014, 2017; Schito et al., 2017), the increasing I_D/I_G ratios of the Raman spectra of CM with increasing temperature in our study might be attributable to the relatively low maturity of the starting CM (bituminous coal). Thus, to characterize fully the temperature–maturity relationship, further friction and heating experiments and organochemical analyses should be performed using CM samples with various initial maturities.

We obtained experimental evidence for the first time that a kinetic effect of heating rate is involved in various organochemical reactions of CM. The results of our organochemical analyses clearly indicate that a higher heating rate can inhibit various CM maturation reactions, including the thermal decomposition of several aromatic compounds and structural rearrangement, thus causing extinction of some IR spectral absorbance peaks, increases in the I_D/I_G ratios of Raman spectra, and decreases in the $I_{toluene}/I_{benzene}$ ratios on py-GC/MS chromatographs (Figure 5.7). These results suggest that the maximum temperatures reported

previously (Hirono et al., 2015; Kaneki et al., 2016; Mukoyoshi et al., 2018) might be too low. On the other hand, Kaneki et al. (2018) demonstrated that shear-induced mechanochemical effects can increase a reactivity of various organochemical reactions, thus lowering the temperatures necessary for the occurrence of CM maturation reactions by approximately 100 °C under a normal stress of 3 MPa and a slip distance of 10 m (Figure 5.7). Although this study focused only on the kinetic effect of heating rate, to understand the CM maturation process during earthquake slip and to establish a more rigorous fault geothermometer based on CM maturity, these two, possibly opposite, effects should be considered simultaneously.

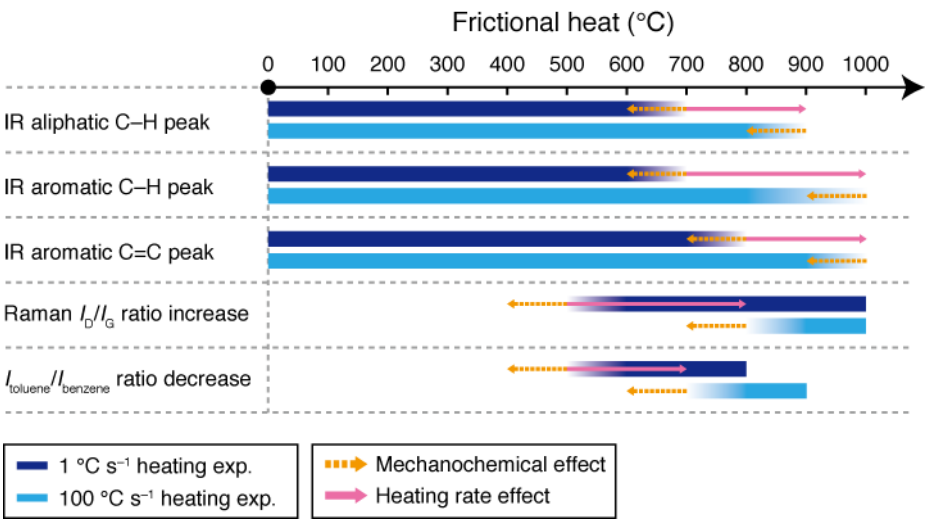

Figure 5.7. Summary of organochemical reactions of CM as a function of temperature. Quantitative data on the mechanochemical effect on reaction temperature are from Kaneki et al. (2018), who reported that the mechanochemical effect can cause CM maturation reactions to occur at temperatures approximately 100 °C lower under a normal stress of 3 MPa and a slip distance of 10 m. *exp.* experiment.

In this study, we focused on how the heating rate might affect the maturation of CM during earthquake slip, and demonstrated experimentally that a high heating rate can inhibit various organochemical reactions of CM. Our results suggest that the maximum slip zone temperatures estimated previously by slow-rate CM heating experiments (Hirono et al., 2015; Kaneki et al., 2016; Mukoyoshi et al., 2018) might be underestimated. Furthermore,

mechanochemical effects during earthquake slip can also strongly affect the maturation of CM (Kaneki et al., 2018). Therefore, comprehensive consideration of the effects on CM maturation of both heating rate and mechanochemistry, as well as of the initial maturity of the starting CM, is needed to establish a more rigorous proxy of frictional heat recorded in fault rocks and to infer fault slip behaviors during earthquakes.

References

Aoya, M., Kouketsu, Y., Endo, S., Shimizu, H., Mizukami, T., Nakamura, D. & Wallis, S. (2010). Extending the applicability of the Raman carbonaceous-material geothermometer using data from contact metamorphic rocks. *J. Metamorph. Geol.* **28**, 895–914.

Beyssac, O., Goffé, B., Chopin, C. & Rouzaud, J.N. (2002). Raman spectra of carbonaceous material in metasediments: a new geothermometer. *J. Metamorph. Geol.* **20**, 859–871.

Burnham, A.K. & Braun, R.L. (1999). Global kinetic analysis of complex materials. *Energy Fuels* **13**, 1–22.

Chester, J.S., Chester, F.M. & Kronenberg, A.K. (2005). Fracture surface energy of the Punchbowl fault, San Andreas system. *Nature* **437**, 133–136.

Cowan, D.S. (1999). Do faults preserve a record of seismic slip? A field geologist's opinion. *J. Struct. Geol.* **21**, 995–1001.

Di Toro, G., Nielsen, S. & Pennacchioni, G. (2005). Earthquake rupture dynamics frozen in exhumed ancient faults. *Nature* **436**,1009–1012.

Evans, J.P., Prante, M.R., Janecke, S.U., Ault, A.K. & Newell, D.L. (2014). Hot faults: Iridescent slip surfaces with metallic luster document high-temperature ancient seismicity in the Wasatch fault zone, Utah, USA. *Geology* **42**, 623–626.

Furuichi, H., Ujiie, K., Kouketsu, Y., Saito, T., Tsutsumi, A. & Wallis, S. (2015). Vitrinite reflectance and Raman spectra of carbonaceous material as indicators of frictional heating on faults: Constraints from friction experiments. *Earth Planet. Sci. Lett.* **424**,

191–200.

Gustafsson, S.E., Karawacki, E. & Khan, M.N. (1979). Transient hot-strip method for simultaneously measuring thermal conductivity and thermal diffusivity of solids and fluids. *J. Phys. D: Appl. Phys.* **12**, 1411–1421.

Hamada, Y., Sakaguchi, A., Tanikawa, W., Yamaguchi, A., Kameda, J. & Kimura, G. (2015). Estimation of slip rate and fault displacement during shallow earthquake rupture in the Nankai subduction zone. *Earth Planets Space* **67**, 39.

Han, R., Shimamoto, T., Hirose, T., Ree, J.-H. & Ando, J. (2007). Ultralow friction of carbonate faults caused by thermal decomposition. *Science* **316**, 878–881.

Hirono, T. *et al*. (2007). A chemical kinetic approach to estimate dynamic shear stress during the 1999 Taiwan Chi-Chi earthquake. *Geophys. Res. Lett.* **34**, L19308.

Hirono, T. *et al*. (2008). Clay mineral reactions caused by frictional heating during an earthquake: An example from the Taiwan Chelungpu fault. *Geophys. Res. Lett.* **35**, L16303.

Hirono, T., Maekawa, Y. & Yabuta, H. (2015). Investigation of the records of earthquake slip in carbonaceous materials from the Taiwan Chelungpu fault by means of infrared and Raman spectroscopies. *Geochem. Geophys. Geosyst.* **16**, 1233–1253.

Hirose, T. & Shimamoto, T. (2005). Growth of molten zone as a mechanism of slip weakening of simulated faults in gabbro during frictional melting. *J. Geophys. Res.* **110**, B05202.

Honda, G., Ishikawa, T., Hirono, T. & Mukoyoshi, H. (2011). Geochemical signals for determining the slip-weakening mechanism of an ancient megasplay fault in the Shimanto accretionary complex. *Geophys. Res. Lett.* **38**, L06310.

Huang, W.L. & Otten, G.A. (1998). Oil generation kinetics determined by DAC-FS/IR pyrolysis: technique development and preliminary results. *Org. Geochem.* **5–7**, 1119–1137.

Ishikawa, T. *et al*. (2008). Coseismic fluid–rock interactions at high temperatures in the Chelungpu fault. *Nat. Geosci.* **1**, 679–683.

Ito, K., Ujiie, K. & Kagi, H. (2017). Detection of increased heating and estimation of coseismic

shear stress from Raman spectra of carbonaceous material in pseudotachylytes. *Geophys. Res. Lett.* **44**, 1749–1757.

Kameda, J., Ujiie, K., Yamaguchi, A. & Kimura, G. (2011). Smectite to chlorite conversion by frictional heating along a subduction thrust. *Earth Planet. Sci. Lett.* **305**, 161–170.

Kaneki, S., Hirono, T., Mukoyoshi, H., Sampei, Y., & Ikehara, M. (2016). Organochemical characteristics of carbonaceous materials as indicators of heat recorded on an ancient plate subduction fault. *Geochem. Geophys. Geosyst.* **17**, 2855–2868.

Kaneki, S., Ichiba, T. & Hirono, T. (2018). Mechanochemical effect on maturation of carbonaceous material: Implications for thermal maturity as a proxy for temperature in estimation of coseismic slip parameters. *Geophys. Res. Lett.* **45**, 2248–2256.

Kitamura, M., Mukoyoshi, H., Fulton, P.M. & Hirose, T. (2012). Coal maturation by frictional heat during rapid fault slip. *Geophys. Res. Lett.* **39**, L16302.

Kouketsu, Y., Mizukami, T., Mori, H., Endo, S., Aoya, M., Hara, H., Nakamura, D. & Wallis, S. (2014). A new approach to develop the Raman carbonaceous material geothermometer for low-grade metamorphism using peak width. *Island Arc* **23**, 33–50.

Kouketsu, Y., Shimizu, I., Wang, Y., Yao, L., Ma, S. & Shimamoto, T. (2017) Raman spectra of carbonaceous materials in a fault zone in the Longmenshan thrust belt, China; comparisons with those of sedimentary and metamorphic rocks. *Tectonophysics* **699**, 129–145.

Kuo, L.-W. *et al*. (2017). Fault gouge graphitization as evidence of past seismic slip. *Geology* **45**, 979–982.

Lewan, M.D. (1997). Experiments on the role of water in petroleum formation. *Geochem. Cosmochem. Acta* **61**, 3691–3723.

Lievens, C., Ci, D., Bai, Y., Ma, L., Zhang, R., Chen, J.Y., Gai, Q., Long, Y. & Guo, X. (2013). A study of slow pyrolysis of one low rank coal via pyrolysis–GC/MS. *Fuel Process. Technol.* **116**, 85–93.

Luque, F.J., Ortega, L., Barrenechea, J.F., Millward, D., Beyssac, O. & Huizenga, J.M. (2009). Deposition of highly crystalline graphite from moderate-temperature fluids. *Geology* **37**,

275–278.

Maekawa, Y., Hirono, T., Yabuta, H., Mukoyoshi, H., Kitamura, M., Ikehara, M., Tanikawa, W. & Ishikawa, T. (2014). Estimation of slip parameters associated with frictional heating during the 1999 Taiwan Chi-Chi earthquake by vitrinite reflectance geothermometry. *Earth Planets Space* **66**, 28.

Mishima, T., Hirono, T., Nakamura, N., Tanikawa, W., Soh, W. & Song, S.-R. (2009). Changes to magnetic minerals caused by frictional heating during the 1999 Taiwan Chi-Chi earthquake. *Earth Planets Space* **61**, 797–801.

Mukoyoshi, H., Sakaguchi, A., Otsuki, K., Hirono, T. & Soh, W. (2006). Co-seismic frictional melting along an out-of-sequence thrust in the Shimanto accretionary complex. Implications on the tsunamigenic potential of splay faults in modern subduction zones. *Earth Planet. Sci. Lett.* **245**, 330–343.

Mukoyoshi, H., Kaneki, S. & Hirono, T. (2018). Slip parameters on major thrusts at a convergent plate boundary: regional heterogeneity of potential slip distance at the shallow portion of the subducting plate. *Earth Planets Space* **70**, 36.

Nakamura, Y., Oohashi, K., Toyoshima, T., Satish-Kumar, M. & Akai, J. (2015). Strain-induced amorphization of graphite in fault zones of the Hidaka metamorphic belt, Hokkaido, Japan. *J. Struct. Geol.* **72**, 142–161.

O'Hara, K. (2004). Paleo-stress estimates on ancient seismogenic faults based on frictional heating of coal. *Geophys. Res. Lett.* **31**, L03601.

Oohashi, K., Han, R., Hirose, T., Shimamoto, T., Omura, K. & Matsuda, T. (2014). Carbon-forming reactions under a reducing atmosphere during seismic fault slip. *Geology* **42**, 787–790.

Polissar, P.J., Savage, H.M. & Broadsky, E.E. (2011). Extractable organic material in fault zones as a tool to investigate frictional stress. *Earth Planet. Sci. Lett.* **311**, 439–447.

Rabinowitz, H.S., Polissar, P.J. & Savage, H.M. (2017). Reaction kinetics of alkenone and n-alkane thermal alteration at seismic timescales. *Geochem. Geophys. Geosyst.* **18**, 204–219.

Rowe, C. & Griffith, W.A. (2015). Do faults preserve a record of seismic slip: A second opinion. *J. Struct. Geol.* **78**, 1–26.

Sakaguchi A. *et al*. (2011). Seismic slip propagation to the updip end of plate boundary subduction interface faults: Vitrinite reflectance geothermometry on Integrated Ocean Drilling Program NanTro SEIZE cores. *Geology* **39**, 395–398.

Savage, H.M., Polissar, P.J., Sheppard, R., Rowe, C.D. & Broadsky, E.E. (2014). Biomarkers heat up during earthquakes: New evidence of seismic slip in the rock record. *Geology* **42**, 99–102.

Schenk, H.J., Witte, E.G., Littke, R. & Schwochau, K. (1990). Structural modifications of vitrinite and alginite concentrates during pyrolytic maturation at different heating rates. A combined infrared, 13C NMR and microscopical study. *Org. Geochem.* **16**, 943–950.

Schito, A., Romano, C., Corrado, S., Grigo, D. & Poe, B. (2017). Diagenetic thermal evolution of organic matter by Raman spectroscopy. *Org. Geochem.* **106**, 57–67.

Schleicher, A.M., Boles, A. & van der Pluijm, B.A. (2015). Response of natural smectite to seismogenic heating and potential implications for the 2011 Tohoku earthquake in the Japan Trench. *Geology* **43**, 755–758.

Sheppard, R.E., Polissar, P.J. & Savage, H.M. (2015). Organic thermal maturity as a proxy for frictional fault heating: Experimental constraints on methylphenanthrene kinetics at earthquake timescales. *Geochim. Cosmochim. Acta* **151**, 103–116.

Sibson, R.H. (1973). Interactions between temperature and pore-fluid pressure during earthquake faulting and a mechanism for partial or total stress relief. *Nature* **243**, 66–68.

Spokas, K.A. (2010). Review of the stability of biochar in soils: predictability of O:C molar ratios. *Carbon Management* **1**, 289–303.

Stuart, B. (2004). *Infrared Spectrometry: Fundamentals and Applications*. Chichester, UK: John Wily.

Tuinstra, F. & Koenig, J.L. (1970). Raman spectrum of graphite. *J. Chem. Phys.* **53**, 1126–1130.

Turian, R.M., Sung, D.J. & Hsu, F.L. (1991). Thermal conductivity of granular coals, coal-water mixtures and multi-solid/liquid suspensions. *Fuel* **70**, 1157–1172.

Supporting information

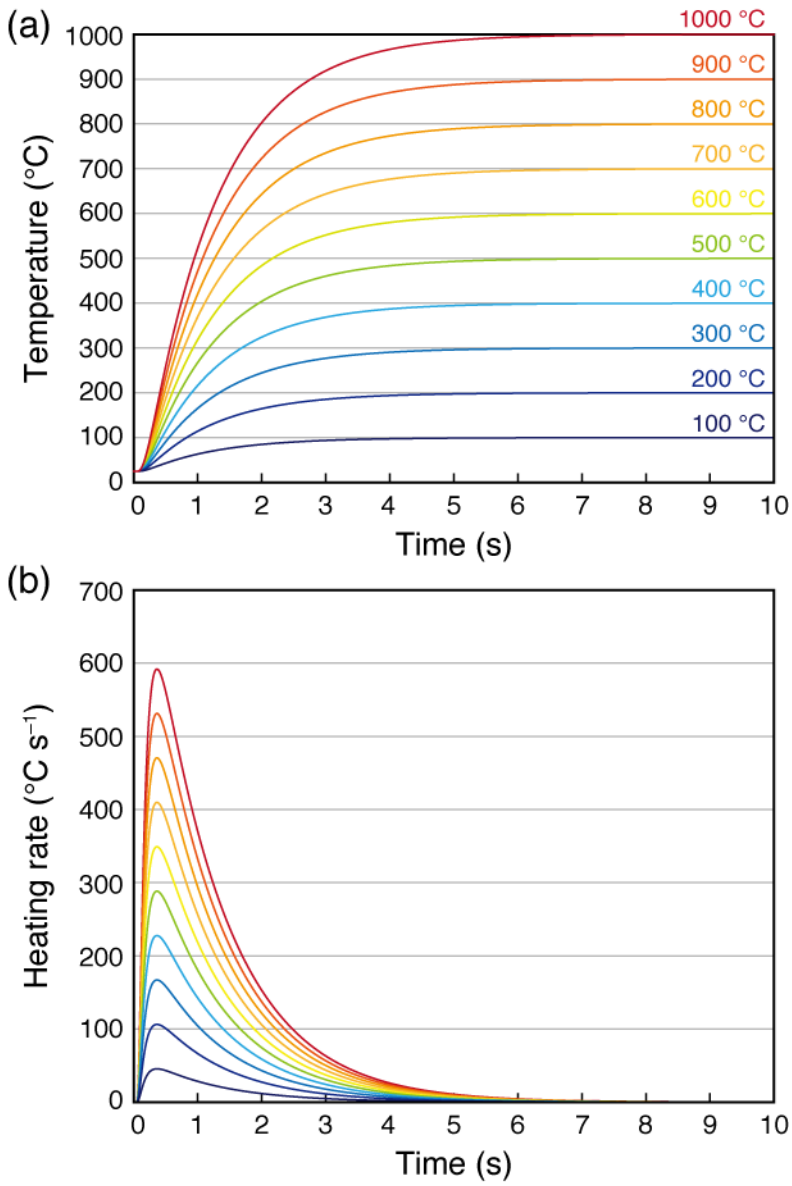

Figure S5.1. Numerical simulation results for the heating experiments. Simulated experimental relationships between (a) temperature and (b) heating rate and time for a 100-μm-diameter particle of CM.

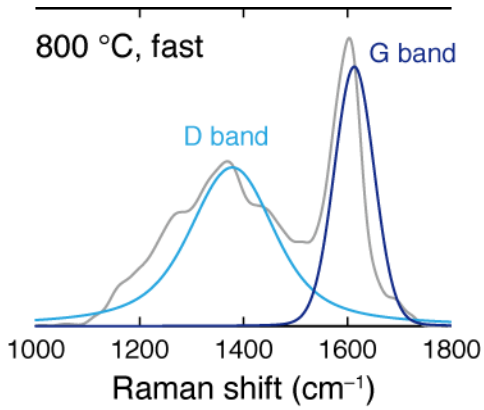

Figure S5.2. Peak decomposition method for Raman spectra. Representative Raman spectrum (800 °C, fast-rate heating experiment) with peaks decomposed for calculation of the I_D/I_G ratio. Our I_D/I_G ratios roughly correspond to I_{D1}/I_{D2} ratios calculated by several prior studies (e.g., Furuichi et al., 2015; Ito et al., 2017).

Table S5.1. Estimated Raman spectral parameters and gas composition ratios. Average I_D/I_G ratios with standard deviations and $I_{toluene}/I_{benzene}$ ratios, for the starting CM and the products of heating experiments. *N.A.*, not available.

Condition	Heating Temperature (°C)	I_D/I_G	$I_{toluene}/I_{benzene}$
	Starting material	0.571 ± 0.020	0.983
Slow heating	100	0.576 ± 0.029	0.918
	200	0.590 ± 0.026	0.950
	300	0.593 ± 0.035	0.999
	400	0.600 ± 0.015	1.009
	500	0.599 ± 0.031	0.829
	600	0.624 ± 0.028	0.326
	700	0.690 ± 0.020	N.A.
	800	0.900 ± 0.029	N.A.
	900	1.043 ± 0.030	N.A.
	1000	1.148 ± 0.026	N.A.
Fast heating	100	0.586 ± 0.013	0.951
	200	0.597 ± 0.013	0.880
	300	0.603 ± 0.018	0.904
	400	0.581 ± 0.012	0.935
	500	0.600 ± 0.013	0.899
	600	0.606 ± 0.018	0.869
	700	0.610 ± 0.009	0.931
	800	0.608 ± 0.012	0.642
	900	0.649 ± 0.012	0.253
	1000	0.799 ± 0.021	N.A.

Chapter 6

Diagenetic weakening with depth of carbon-bearing faults along the plate subduction interface

This chapter is preparing for submission to an international scientific journal (2018/01/23).

Abstract

Subduction-related diagenetic reactions, such as the smectite to illite transformation, affect fault strength and are thus important for understanding earthquake dynamics in subduction zones. Carbonaceous material (CM) is found worldwide in active plate-boundary and inland faults, yet the effect of its diagenetic transformation on frictional strength and earthquake rupture dynamics remains unknown. We conducted high-velocity friction experiments, chemical analyses, X-ray diffraction measurements and transmission electron microscope observations on CM in the form of lignite, bituminous coal, anthracite and graphite. Our results clearly show that an increase in CM crystallinity through stacking of graphene sheets leads to a decrease in the yield friction coefficient (from 0.5 to 0.2). These findings suggest that diagenetic transformation of CM progressively weakens carbon-bearing faults with increasing depth along the subducting plate interface, possibly affecting rupture propagation processes. Thus, diagenetic transformation of CM appears to contribute to the depth-dependences of frictional strength and rupture dynamics on plate-subduction faults.

6.1. Introduction

Earthquakes at and around plate-subduction zones sometimes generate gigantic tsunamis that endanger coastal areas. Understanding the effect of diagenetic reactions that change the physical, hydrological and thermal conditions and processes at plate interfaces is important for understanding earthquake dynamics in subduction zones (Moore & Saffer, 2001; Saffer & Tobin, 2011). The links between diagenesis and earthquake dynamics along the shallow parts of plate subduction interfaces (depths of up to several tens of kilometres) have been attributed to changes of the chemistry of fault-forming materials, changes of local physical and hydrological properties and changes of pore-fluid pressures (Moore & Vrojilk, 1992), all of which are related to smectite to illite transformations (Spinelli & Saffer, 2004; Peltonen et al., 2009; Saffer et al., 2012; Lauer et al., 2017), as well as crystallization of opal to quartz (Spinelli & Saffer, 2004; Hüpers et al., 2017), crystallization of palagonite to smectite (Hüpers et al.,

2017) and lithification processes (Moore & Saffer, 2001; Saffer & Tobin, 2011; Hüpers et al., 2017; Lauer et al., 2017). For example, it is likely that large historical earthquakes ($Mw \geq 6.9$) offshore Costa Rica were associated with dehydration of smectite and illitization-induced silica cementation (Lauer et al., 2017). Similarly, the 2004 Sumatra-Andaman earthquake ($Mw = 9.2$) was driven by dehydration of silicates before subduction (Hüpers et al., 2017). However, the relationship of diagenetic thermal maturation of carbonaceous material (Schito et al., 2017) to fault strength and earthquake rupture dynamics remains poorly understood.

The frictional strength of faults within the brittle crust is an important controlling factor in earthquake mechanics; it governs the dynamics of earthquake nucleation and rupture propagation (Scholz, 2002). The results of conventional geological and seismological observations and laboratory friction experiments suggest that some faults within the brittle crust are frictionally weak (Faulkner et al., 2006; Chiaraluce et al., 2007; Moore & Rymer, 2007; Oohashi et al., 2012; Ujiie et al., 2013). Plausible explanations for fault weakness include the presence of frictionally weak materials (Moore & Rymer, 2007; Oohashi et al., 2012; Ujiie et al., 2013), high pore-fluid pressures (Faulkner et al., 2006; Chiaraluce et al., 2007), foliation fabrics in fault rocks (Collettini et al., 2009) and dynamic fault-weakening processes (Di Toro et al., 2011). In particular, the abundance of weak clay minerals has been widely used as an explanation for fault weakness in subduction zones (Vrojilk, 1990).

Carbonaceous material (CM) is another common material in the brittle crust. Carbon-bearing rocks are common in both plate-boundary faults (Kaneki et al., 2016; Kirilova et al., 2017; Mukoyoshi et al., 2018) and inland active faults (Zulauf et al., 1990; Manatschal, 1999; Craw, 2002; Oohashi et al., 2011, 2012; Kameda et al., 2014; Kuo et al., 2014; Nakamura et al., 2015), and in seafloor sediments near plate-subduction trenches (Premuzic et al., 1982) (Figure 6.1). Laboratory experiments have shown that CM has lower frictional resistance (Adams et al., 1993; Yu et al., 2007; Oohashi et al., 2011, 2013; Rutter et al., 2013) than typical crust-forming rocks on Earth such as granite and sandstone (Byerlee, 1978) and its presence weakens fault strength and affects rupture process (Oohashi et al., 2013; Yao et al., 2013; Zhang et al., 2013; Kuo et al., 2014; Spagnuolo et al., 2015; Kouketsu et al., 2017). Furthermore,

increases of the thermal maturity of CM as a result of diagenetic reactions9 probably affect its frictional properties (Atkinson & Ko, 1977; Oohashi et al., 2011). However, we know little about the relationship of diagenesis-driven CM transformation (maturation of CM) to frictional properties in carbon-bearing faults.

To examine this relationship, we performed chemical analyses, X-ray diffraction measurements and transmission electron microscope observations on four samples of simulated carbon-rich fault material (lignite, bituminous coal, anthracite and graphite) and then, using those samples, conducted rotary-shear friction experiments designed to reproduce seismic slip. The frictional properties and chemistry of the CM that we determined enabled us to infer the main cause of changes in its frictional strength and to consider the implications of these changes for depth-dependent frictional strength of faults and rupture dynamics in plate-subduction zones.

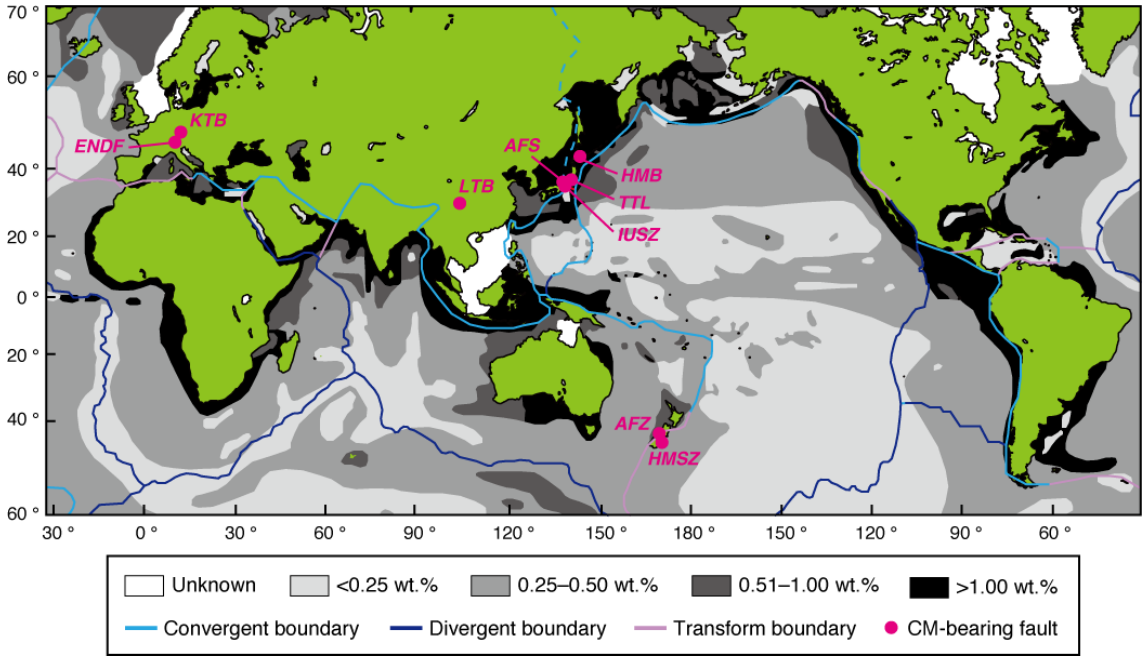

Figure 6.1. Worldwide distribution of carbon-bearing faults. Map showing concentrations of CM in oceanic sediments (Premuzic et al., 1982) and major plate boundaries. *ENDF*, Err Nappe detachment fault (Manatschal, 1999); *KTB*, KTB borehole (Zulauf et al., 1990); *LTB*, Longmenshan thrust belt (Kuo et al., 2014); *AFS*, Atotsugawa fault system (Oohashi et al., 2012); *IUSZ*, Inuyama-Unuma shear zone (Kameda et al., 2014); *TTL*, Tanakura Tectonic Line (Oohashi et al., 2011); *HMB*, Hidaka metamorphic belt (Nakamura et al., 2015); *AFZ*, Alpine fault zone (Kirilova et al., 2017); *HMSZ*, Hyde–Macraes shear zone (Craw, 2002).

6.2. Materials and methods

6.2.1. Extraction of CMs

Three bulk coal samples (lignite from Yasu, Shiga Prefecture, Japan; bituminous coal from Ashibetsu, Hokkaido Prefecture, Japan; anthracite from a mine in Yamaguchi Prefecture, Japan) were manually powdered using an agate mortar and pestle. These samples were then treated with 18 N HCl for 1 h to remove metals, sulfides, and carbonates. The reacted liquid and solid residues were then separated by using a centrifuge. The solid

residues were treated with 46 N HF for 1 day to remove silicates, after which the supernatant liquid was removed. The precipitates were treated again with 18 N HCl for 1 day to remove fluoride by-products, and the supernatant liquid was again removed. Finally, the precipitates were rinsed with distilled water and the solid residues were separated by using a centrifuge. After three repetitions of this rinsing process, the final solid CM residues were dried at 50 °C.

The concentrations of CM in the bulk coal samples were 90.0 ± 12.7 wt.% (lignite), 99.9 ± 2.5 wt.% (bituminous coal) and 62.8 ± 14.1 wt.% (anthracite).

We also used a sample of pure graphite (Wako Pure Chemical Industries product No. 072-03845) to represent fully mature CM.

6.2.2. Elemental analysis

Elemental compositions (C, H, and O) of the four types of CM were determined with an elemental analyser (Flash EA 1112, Thermo Finnigan). About 1 mg of dried CM wrapped in tin film was first heated to 1000 °C to dissolve the film and then combusted at 1800 °C in a quartz column. In CHN measurement mode, N_2, CO_2, and H_2O gas from the heated CM were separated in a quartz tube filled with chrome oxide, reduced copper, and cobalt. In O measurement mode, a carbon nickel plate, quartz turnings, soda lime, and magnesium perchlorate were used to extract CO gas from the pyrolysates in the quartz tube. Sulfanilamide (C, 41.84 wt.%; H, 4.68 wt.%; N, 16.27 wt.%; S, 18.62 wt.%; O, 18.58 wt.%) was used as a standard to obtain a calibration curve for each element. Five measurements were carried out on each type of CM to obtain mean values and standard deviations of the atomic ratios of O/C and H/C.

6.2.3. Transmission electron microscope observation

The transmission electron microscope (TEM; JSM-2100, JEOL) we used was operated at an acceleration voltage of 200 kV with a magnification of 500,000. Before TEM observations,

approximately 30 μL of distilled water was added to a small amount of CM, and 3 μL of the resultant suspension was titrated onto a copper microgrid. The microgrid was then dried for 1 week at 40 °C under vacuum (≤10 Pa).

6.2.4. X-ray diffraction analysis

X-ray diffraction (XRD) profiles of CM were obtained by using a Spectris PANalytical X'Pert PRO MPD spectrometer with monochromatised CuKα radiation operated at tube voltage of 45 kV and tube current of 40 mA. The scan range was 3°–75° (Δ2θ), an angle resolution of 0.001°, a scan rate of 0.1° s^{-1}, and a step width of 0.008°. Before analysis, each CM sample was dried at 50 °C for several hours. The acquired raw profiles were smoothed by the polynomial cubic method at a convolution range of 15, and were thinned by a step width of 0.020°. A zero-diffraction plate (made from silicon) was used as a sample holder.

6.2.5. Friction experiment

We used a rotary-shear friction apparatus at Yamaguchi University (Supporting Information Figure S6.1) to obtain the changes of shear stress of CM with slip displacement. For each experiment, two cylinders of Berea sandstone were first immersed in distilled water under vacuum for 1 h. CM powder (particle size ≤75 μm) was then placed on the circular surface of the sandstone cylinder to be used on the rotating side of the friction apparatus and saturated with 1.0 mL of distilled water. The two cylinders were then placed end to end with the CM between them (Supporting Information Figure S6.1) and enclosed in a polytetrafluoroethylene sleeve that was attached to the cylinder to be used on the rotating side of the apparatus. The sample thus assembled was again immersed in distilled water under vacuum for 1 h.

After placing the sample in the apparatus, it was rotated 2–3 times under normal stress of ~0.4 MPa to ensure a uniform thickness of gouge and then, after application of the target

normal stress (the pre-compaction step), it was held stationary for 30 min. For all experiments, the thickness of the CM after pre-compaction was about 1.3 mm. During pre-compaction, the sample was wrapped with a water-saturated cleaning tissue which was in turn wrapped in polyolefin film to prevent drying of the CM. Before each experiment, N_2 gas was flowed through the apparatus for 5 min at a pressure of 0.1 MPa to prevent oxidation (combustion) of CM during the experiments. The raw torque data were acquired at a frequency of 200 Hz. Torque data acquired before each experiment were used for background correction of the raw data, and then the torque data between the Berea sandstone cylinders and the polytetrafluoroethylene sleeve was subtracted (Supporting Information Figure S6.2).

The mechanical data, after subtracting the background noise and friction between the specimen and the polytetrafluoroethylene sleeve (Supporting Information Figure S6.2), were fitted by the empirical exponential power law using a least-squares fitting method. Although this is a broadly accepted method for fitting curves to mechanical data obtained in high-speed friction experiments (Oohashi et al., 2011, 2013; Kouketsu et al., 2017), the choice of fitting variables is a critical concern. We therefore fitted the corrected mechanical data for four sets of variables: (i) τ_y, τ_d, and D_c, (ii) τ_d and D_c, (iii) τ_y and D_c, and (iv) D_c, where τ_d is dynamic shear stress (MPa), τ_y is yield shear stress (MPa), and D_c is dynamic slip-weakening distance (m), respectively. Fitting curves of representative mechanical data for these four sets of variables are shown in Supporting Information Figure S6.3. For the cases where τ_y and τ_d were constant, we adopted the values of the maximum shear stress at the initial stage of the experiment and the average shear stress at displacement of 14–15 m for τ_y and τ_d, respectively (Supporting Information Figure S6.3). The coefficient of determination (R^2) is defined as follows:

$$R^2 = 1 - \frac{\sum(\tau_{meas} - \tau_{calc})^2}{\sum(\tau_{meas} - \tau_{mean})^2} \ , \tag{6.1}$$

where τ_{meas} is the corrected shear stress (MPa), τ_{calc} is the shear stress calculated by using a least-squares fitting method (MPa), and τ_{mean} is the shear stress obtained by averaging the corrected shear stress (MPa). Supplementary Figure S6.4 shows all of the corrected mechanical data for the four fitting curves for each normal stress and each type of CM. Supplementary Figure S6.5 shows the fitting lines and curves for the estimated τ_y, τ_d, and D_c values for each

type of CM and the four sets of variables. Supporting Information Tables S1–S4 summarize the frictional properties we obtained for lignite, bituminous coal, anthracite, and graphite, respectively. Among the four fitting methods, using τ_y, τ_d, and D_c as variables resulted in the best fitting curve with the highest R^2 value for all stress conditions. Therefore, we adopted τ_y, τ_d, and D_c as variables in our calculations of frictional properties.

6.3. Results

6.3.1. Chemistry of CM specimens.

Our elemental analyses showed the atomic O/C and H/C molar ratios of our samples to be respectively 0.37 ± 0.03 and 1.93 ± 0.11 for lignite, 0.07 ± 0.00 and 1.58 ± 0.16 for bituminous coal, 0.03 ± 0.00 and 0.74 ± 0.08 for anthracite and 0.00 ± 0.00 and 0.00 ± 0.00 for graphite.

Transmission electron microscope (TEM) observations of the lignite and bituminous coal samples showed an absence of crystalline structure without distinct diffraction patterns (Figure 6.2a and b), whereas the anthracite showed a small diffraction pattern (Figure 6.2c) and the graphite showed well-ordered crystalline structure with a clear diffraction pattern (Figure 6.2d).

X-ray diffraction (XRD) profiles of the lignite and bituminous coal samples showed no distinct peaks, but each showed a broad peak at 2θ = 20°–30° indicating an amorphous structure (Figure 6.2e and f). In contrast, the XRD profile of the anthracite sample showed a relatively sharp peak at around 2θ = 25.4° (Figure 6.2g) and that of graphite showed a strong peak at 2θ = 26.7° (Figure 6.2h).

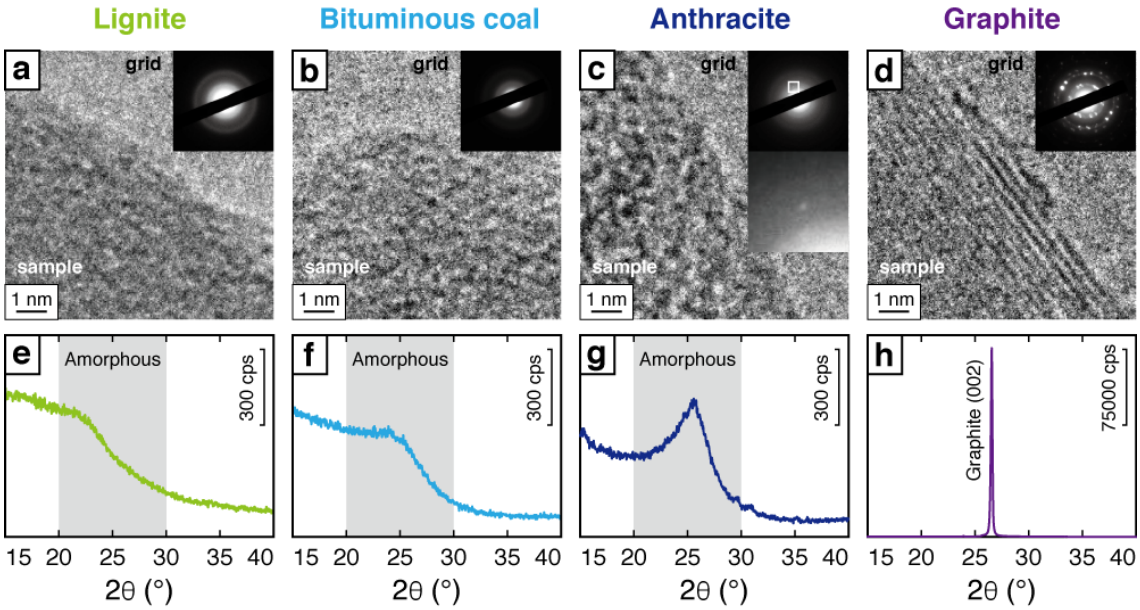

Figure 6.2. Crystallinity of CM specimens. Results of TEM observations of CM showing nanoscale structure and diffraction patterns (a to d) and XRD profiles of CM (e to h).

6.3.2. Frictional properties of CMs

We conducted rotary-shear friction experiments on our CM samples at normal stresses of 0.5, 1.0, 1.5 and 2.0 MPa and a slip rate of 1 m s^{-1} under water-saturated conditions in a N_2 atmosphere at room temperature. We applied the following empirical exponential slip-weakening friction law to determine the best-fit curves for the changes of shear stress with displacement:

$$\tau = \tau_d - (\tau_d - \tau_y) exp\left(-\frac{D}{D_c}\right) \tag{6.2}$$

where τ is shear stress (MPa) as a function of displacement, D is displacement (m), τ_d is dynamic shear stress (MPa), τ_y is yield shear stress (MPa), and D_c is dynamic slip-weakening distance (m). We then applied the empirical law to determine best-fit curves for the calculated values of τ_y, τ_d, and D_c:

$$\tau_{y(d)} = \mu_{y(d)}\sigma_n + C \tag{6.3}$$

$$D_c = \alpha {\sigma_n}^{-\beta} \tag{6.4}$$

where μ_y and μ_d are yield and dynamic friction coefficients, respectively, σ_n is normal stress (MPa), C is a cohesion term (MPa) and α and β are experimentally determined coefficients. All of the samples showed clear decreases in shear stress with increasing slip distance under all normal stress conditions (Supporting Information Figure S6.4), and the data were well fitted by equation (6.2). The estimated values of τy and τd show strong linearity but the slopes of the best-fit lines differ according to the type of CM tested (Figure 6.3a and b), except for τ_d of bituminous coal. Although the μy values for lignite and bituminous coal were almost the same (~0.5), those of anthracite and graphite were slightly and markedly lower (0.3–0.4 and 0.1–0.2, respectively) (Figure 6.3a). All of the samples showed similar μ_d values of ~0.1–0.2 (Figure 6.3b). D_c values decreased with increasing σ_n and were well fitted by equation (6.4) for all samples except graphite, for which Dc values were zero for all stress conditions (Figure 6.3c). Although the calculated values of α and β differed slightly (0.00 to 2.63 and 0.00 to 0.66, respectively) depending on the type of CM tested, the values obtained are negligible compared to those of other rock-forming minerals (3–78 and 1.13–1.24 for α and β, respectively) (Di Toro et al., 2011).

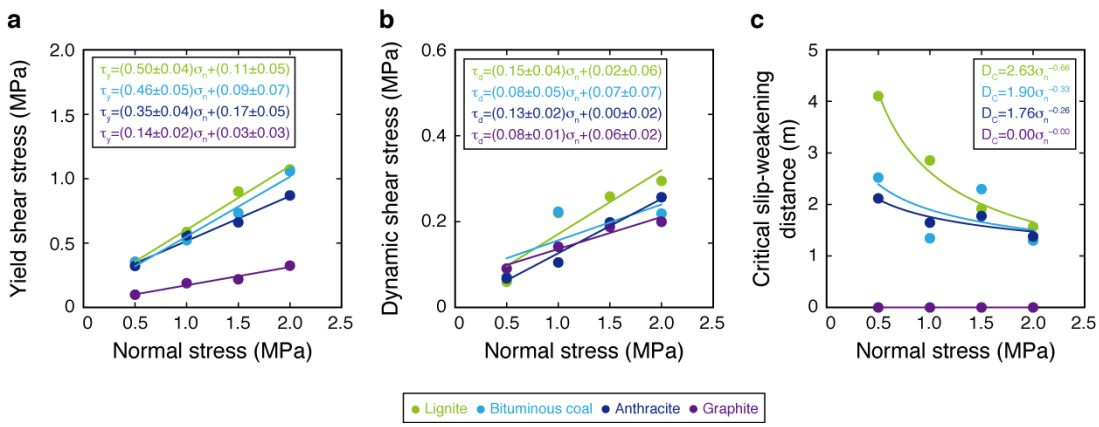

Figure 6.3. Determination of frictional properties of CM specimens. Estimated values of yield shear stress (τ_y) (a), dynamic shear stress (τ_d) (b), and dynamic slip-weakening distance (D_c) (c) plotted against normal stress. Fitting errors and intercepts of best-fit slopes for yield and dynamic friction are also shown.

6.4. Discussion and conclusions

Our TEM observations and XRD measurements clarified the differences in the crystallinity of the four types of CM we used. The lignite and bituminous coal samples were completely amorphous, with no diffraction patterns in TEM images (Figure 6.2a and b) and a clear broad peak at 2θ = 20°–30° in XRD profiles (Figure 6.2e and f). Although lignite showed a slightly brighter ring in TEM images than bituminous coal (Figure 6.2a and b), indicating that lignite particle observed had more crystal-like structure, such difference is unlikely to cause dramatic changes in bulk crystallinity investigated in XRD profiles between two CM samples (Figure 6.2 e and f). Anthracite showed a weak diffraction pattern in a TEM image and a relatively sharp peak at 2θ = 25.4° in an XRD profile (Figure 6.2c and g), strongly suggesting a partly crystallized structure. Graphite was fully crystallized with a clear diffraction pattern and a very sharp peak at 2θ = 26.7° (Figure 6.2d and h).

Previous high-velocity friction experiments on amorphous carbon samples corresponding to the lignite and bituminous coal used in this study revealed μ_y and μ_d values of 0.54 and 0.15, respectively (Oohashi et al., 2011); these values are well consistent with our experimental results (Figure 6.3a and b). Natural CM-bearing fault rocks or their surrounding host rocks, such as those of the Longmenshan fault that slipped during the 2008 Wenchuan earthquake, include ~25–30 wt.% poorly crystallized CM and have μy and μd values of 0.47–0.53 and 0.13–0.16, respectively (Kuo et al., 2014; Kouketsu et al., 2017); these characteristics are also well consistent with our results (Figure 6.3a and b). Among the frictional properties we determined (Figure 6.3), only the yield friction coefficient μ_y showed a systematic change related to the chemistry of CM, which means that it is a crucial factor when considering friction and rupture dynamics along carbon-bearing faults. Our results showed that μ_y decreased with decreasing O/C and H/C ratios (Figure 6.4), and the amorphous CM specimens (lignite and bituminous coal) had higher values of μ_y (~0.5) than the more crystalline anthracite and graphite specimens (0.3–0.4 and 0.1–0.2, respectively). Thus, the relationship of the crystallinity of CM to its elemental composition is an essential controlling factor for frictional strength.

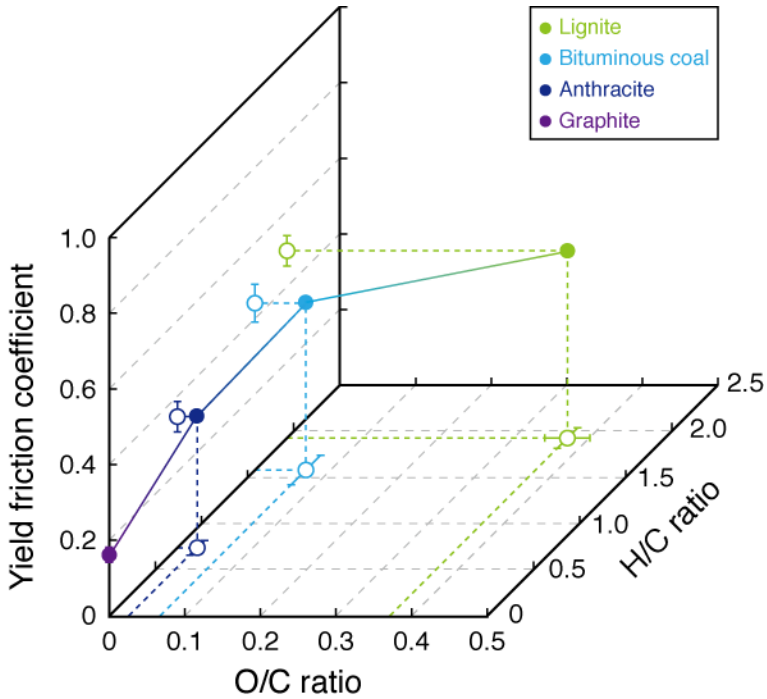

Figure 6.4. Relationships of yield friction with H/C and O/C ratios of CM specimens. Errors of yield friction and atomic ratios were derived from fitting errors and standard deviations (n = 5), respectively.

Previous studies have reported that faults become weak when they contain ≥20 vol.% CM in bulk samples (Oohashi et al., 2013; Rutter et al., 2013). Thus, although the typical concentrations of CM in and around plate-subduction zones (≥1 vol.%; Figure 6.1) might be insufficient to cause quasi-static fault weakening, the segregation of weak material into layers on the fault plane can weaken faults at much lower concentrations of CM (a few vol.%) (Niemeijer et al., 2010; Rutter et al., 2013; Smeraglia et al., 2017). Such layering may be a result of deposition of CM from C-H-O-rich fluids along faults (Luque et al., 2009), diffusive mass transfer processes (Oohashi et al., 2012), and formation of CM from carbonate minerals by frictional slip (Oohashi et al., 2014; Spagnuolo et al., 2015; Delle Piane et al., 2018). Thus, small amounts of CM in faults are likely to cause disproportionate fault weakening in and around subduction zones.

The progress of diagenetic reactions depends mainly on temperature and burial depth.

For example, the smectite to illite transformation at temperatures of 60–140 °C (Freed & Peacor, 1989) can lead to an increase in the frictional strength of fault rocks. The crystallinity of CM can increase with increasing temperature (Schito et al., 2017), leading to a dramatic decrease in yield friction (Figure 6.4). By considering our results together with previous chapters, we developed a schematic cross section illustrating the transitions with increasing temperature of yield frictional strength, crystallinity and representative molecular structures of CM in a subducting oceanic plate (Figure 6.5). In addition, mechanical and thermal processes during coseismic slip on a carbon-bearing fault can enhance the transformation of CM (Chapters 3–5), which might contribute to the maturation of the CM in plate-subduction faults. Thus, in addition to diagenetic CM reactions, coseismic transformation should be considered as a potential factor controlling CM distribution and thus frictional strength of carbon-bearing faults.

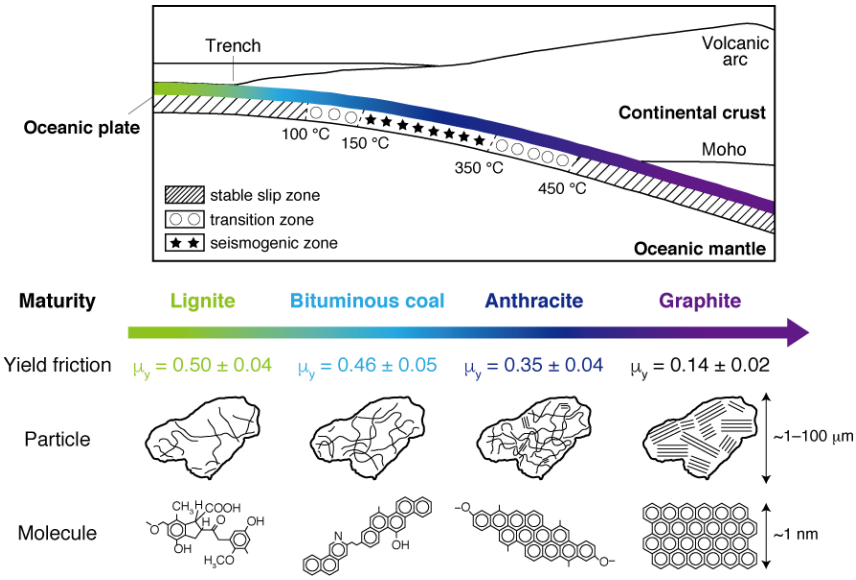

Figure 6.5. Schematic model of diagenetic transformation of CM along a subducting plate interface. Simplified tectonic cross section showing depth- and temperature-dependent changes in typical slip behaviours (Hyndman et al., 1997) and progressive maturation of CM. Changes with depth of yield friction, crystallinity and representative molecular structure for each type of CM are also shown (as inferred from friction experiments, TEM observations and XRD measurements, and Matthews & Chaffee, 2012, respectively).

The frictional data obtained from high-velocity friction experiments provide insights into the process of rupture propagation during an earthquake (Faulkner et al., 2011; Yao et al., 2013). For example, fracture energy, *G*, which is calculated from the evolution of shear stress during slip, is a key factor for the control of rupture dynamics during an earthquake (McGarr et al., 2004; Andrews, 2005; Cocco et al., 2006). *G* is the energy required to advance a rupture front along a fault and, in the case of an "ideal" (Griffith) crack, all of the fracture energy is consumed as surface energy to generate new slip interface (Palmer & Rice, 1973). Some seminal studies (Andrews, 1976; McGarr et al., 2004; Cocco et al., 2006) have proposed that *G* determines rupture velocity. Theoretical calculations have suggested that the lower the ratio of *G* to total seismic energy (i.e., as *G* decreases), the higher the rupture velocity (Andrews, 2005), possibly because the lower yield shear strength of the fault provides less resistance to rupture propagation. To investigate the influence of diagenetic reactions of CM on the rupture dynamics of carbon-bearing faults, we calculated *G* for all of our experiments (with the exception of bituminous coal under 1 MPa) by using the following equation (Abercrombie & Rice, 2005):

$$G = \int_0^D (\tau_{meas} - \tau_d)\, dt \tag{6.5}$$

The resultant values of *G* for amorphous CM samples were 1.15 ± 0.08 and 1.00 ± 0.26 MJ m^{-2} for lignite and bituminous coal, respectively, which were higher than those of partly and completely crystallized CM (0.72 ± 0.13 and 0.00 ± 0.00 MJ m^{-2} for anthracite and graphite, respectively). These results suggest that diagenetic crystallization of CM with increasing depth decreases *G* and may thus increase rupture velocity in plate-subduction faults. Given that rupture velocity of mode III crack cannot exceed S-wave velocity V_S (Scholz, 2002), such potential differences in rupture velocity cannot be attributable to the increase in density with increasing CM maturity that results in decrease in V_S. Although another factor controlling V_S, shear modules, may play a dominant role in increase in rupture velocity, however, further investigations are required to determine the main control on changes in rupture velocity of CM.

The stress ratio (*S*) is another important influence on rupture propagation and is expressed as follows (Andrews, 1976; Scholz, 2002):

$$S = (\tau_y - \tau_i)/(\tau_i - \tau_d) = (\mu_y - \mu_i)/(\mu_i - \mu_d) \quad (6.6)$$

where τ_i is initial shear stress (MPa) and μ_i is initial friction coefficient. S is a dimensionless parameter that controls the evolution of rupture with time and slip (Andrews, 1976, 1985; Das & Aki, 1977; Bruhat et al., 2016). For example, numerical modelling of rupture propagation along a mode II crack by assuming a simple slip-weakening model and S of 0.8 has shown that as time and slip increase, rupture velocity passes through Rayleigh-wave velocity and finally approaches P-wave velocity (Andrews, 1985). Similarly, fault-plane modelling (Das & Aki, 1977) has suggested that a fault patch with a higher stress ratio than surrounding patches restrains rupture propagation because its higher yield shear strength or lower initial background shear strength makes rupture propagation more difficult. Thus, the stress ratio is universally applicable in studies of earthquake rupture dynamics.

We calculated stress ratios for each of our CM samples based on the experimentally determined frictional properties (Figure 6.3) and equation (6.6). Although our high-velocity friction experiments provided only τ_y and τ_d, previous experiments on pure CM have provided friction coefficients at low slip velocity, which corresponds to μ_i in equation (6.6), of 0.43 and 0.09 for amorphous and crystallized CM, respectively (Oohashi et al., 2011). Therefore, we calculated the stress ratios for lignite, bituminous coal and graphite to be 0.25, 0.15 and 5.00, respectively. Importantly, this systematic increase of stress ratio with increasing maturity of CM indicates that the progressive diagenetic reactions of CM with increasing depth may inhibit rupture propagation. Thus, we can infer from our experimental results that higher values of G, lower stress ratios and lower rupture velocities are more likely to occur along the shallow part of plate-boundary faults; these conditions are consistent with the results of analyses of dense seismic array data (Meng et al., 2011) and two-dimensional dynamic rupture modelling (Huang et al., 2014) of the 2011 Tohoku-Oki earthquake. Therefore, the diagenetic reactions of CM are important processes that affect earthquake rupture dynamics along carbon-bearing plate-subduction faults.

Our experiments revealed that the yield friction of CM decreases systematically as its crystallinity increases. Diagenetic reactions of CM accompanying plate subduction can increase

CM crystallinity such that carbon-bearing faults are progressively weakened with increasing depth along the subducting plate interface. Our experimental results also imply that the progression with depth of diagenetic reactions of CM in faults is likely to cause a decrease in fracture energy and an increase in stress ratio, possibly affecting the rupture process of those faults. We suggest that, in addition to the effect of diagenetic reactions such as the smectite to illite transformation, the increase with depth of crystallinity of CM is an important mechanism that affects earthquake dynamics at plate-subduction boundaries worldwide. To improve our understanding of earthquake mechanics for carbon-bearing faults, in terms of both rupture initiation and propagation, further low-velocity friction experiments on CM, which determine frictional properties and its relation to the rate-and-state friction law (Dieterich, 1978; Ruina, 1983), are needed.

References

Abercrombie, R.E. & Rice, J.R. (2005). Can observations of earthquake scaling constrain slip weakening? *Geophys. J. Int.* **162**, 406–424.

Adams, M.J., Briscoe, B.J., Motamedi, F. & Streat, M. (1993). The frictional characteristics of coal particles. *J. Phys. D: Appl. Phys.* **26**, 73–82.

Andrews, D.J. (1976). Rupture velocity of plane strain shear cracks. *J. Geophys. Res.* **81**, 5679–5687.

Andrews, D.J. (1985). Dynamic plane-strain shear rupture with a slip-weakening friction law calculated by a boundary integral method. *Bull. Seismol. Soc. Am.* **75**, 1–21.

Andrews, D.J. (2005). Rupture dynamics with energy loss outside the slip zone. *J. Geophys. Res.* **110**, B01307.

Atkinson, R.H. & Ko, H.-Y. (1977). Strength characteristics of U.S. coals. *The 18th U.S. Symposium on Rock Mechanics (USRMS)*, 2B3-1–6.

Bruhat, L., Fang, Z. & Dunham, E.M. (2016). Rupture complexity and the supershear transition on rough faults. *J. Geophys. Res.* **121**, 210–224.

Byerlee, J. (1978). Friction of rocks. *Pure Appl. Geophys.* **116**, 615–626.

Chiaraluce, L., Chiarabba, C., Collettini, C., Piccinini, D. & Cocco, (2007). M. Architecture and mechanics of an active low-angle normal fault: Alto Tiberina Fault, northern Apennines, Italy. *J. Geophys. Res.* **112**, B10310.

Cocco, M., Spudich, P. & Tinti, E. (2006). On the mechanical work absorbed in faults during earthquake ruptures. *Earthquakes Radiated Energy and the Physics of Faulting 170*, 237–254.

Collettini, C., Niemeijer, A., Viti, C. & Marone, C. (2009). Fault zone fabric and fault weakness. *Nature* **462**, 907–910.

Craw, D. (2002). Geochemistry of late metamorphic hydrothermal alteration and graphitisation of host rock, Macraes gold mine, Otago Schist, New Zealand. *Chem. Geol.* **191**, 257–275.

Das, S. & Aki, K. (1977). Fault plane with barriers: A versatile earthquake model. *J. Geophys. Res.* **82**, 5658–5670.

Delle Piane, C. *et al*. Generation of amorphous carbon and crystallographic texture during low-temperature subseismic slip in calcite fault gouge. *Geology* **46**, 163–166.

Dieterich, J.H. (1978). Time-dependent friction and the mechanics of stick-slip. *Pure Appl. Geophys.* **116**, 790–806.

Di Toro, G., Han, R., Hirose, T., De Paola, N., Nielsen, S., Mizoguchi, K., Ferri, F., Cocco, M. & Shimamoto, T. (2011). Fault lubrication during earthquakes. *Nature* **471**, 494–498.

Faulkner, D.R., Mitchell, T.M., Healy, D. & Heap, M.J. (2006). Slip on 'weak' faults by the rotation of regional stress in the fracture damage zone. *Nature* **444**, 922–925.

Faulkner, D.R., Mitchell, T.M., Behnsen, J., Hirose, T. & Shimamoto, T. (2011). Stuck in the mud? Earthquake nucleation and propagation through accretionary forearcs. *Geophys. Res. Lett.* **38**, L18303.

Freed, R.L. & Peacor, D.R. Variability in temperature of the smectite/illite reaction in Gulf Coast sediments. *Clay Miner.* **24**, 171–180.

Huang, Y., Ampuero, J.-P. & Kanamori, H. (2014). Slip-weakening models for the 2011

Tohoku-Oki earthquake and constraints on stress drop and fracture energy. *Pure Appl. Geophys.* **171**, 2555–2568.

Hüpers, A. *et al*. (2017). Release of mineral-bound water prior to subduction tied to shallow seismogenic slip off Sumatra. *Science* **356**, 841–844.

Hyndman, R.D., Yamano, M. & Oleskevich, D.A. (1997). The seismogenic zone of subduction thrust faults. *Island Arc* **6**, 244–260.

Kaneki, S., Hirono, T., Mukoyoshi, H., Sampei, Y. & Ikehara, M. (2016). Organochemical characteristics of carbonaceous materials as indicators of heat recorded on an ancient plate-subduction fault. *Geochem. Geophys. Geosyst.* **17**, 2855–2868.

Kameda, J. *et al*. (2014). The influence of organic-rich shear zones on pelagic sediment deformation and seismogenesis in a subduction zone. *J. Mineral. Petrol. Sci.* **109**, 28–238.

Kirilova, M. *et al*. (2017). Textural changes of graphitic carbon by tectonic and hydrothermal processes in an active plate boundary fault zone, Alpine Fault, New Zealand. *Geol. Soc. London* **453**.

Kouketsu, Y., Shimizu, I., Wang, Y., Yao, L., Ma, S. & Shimamoto, T. (2017). Raman spectra of carbonaceous materials in a fault zone in the Longmenshan thrust belt, China; comparisons with those of sedimentary and metamorphic rocks. *Tectonophysics* **699**, 129–145.

Kuo, L.-W. *et al*. (2014). Gouge graphitization and dynamic fault weakening during the 2008 Mw 7.9 Wenchuan earthquake. *Geology* **42**, 4570–4573.

Lauer, R.M., Saffer, D.M. & Harris, R.N. (2017). Links between clay transformation and earthquakes along the Costa Rican subduction margin. *Geophys. Res. Lett.* **44**, 7725–7732.

Luque, F.J., Ortega, L., Barrenechea, J.F., Millward, D., Beyssac, O. & Huizenga, J.-M. (2009). Deposition of highly crystalline graphite from moderate-temperature fluids. *Geology* **37**, 275–278.

Manatschal, G. (1999). Fluid and reaction assisted low angle normal faulting: evidence from rift

related brittle fault rocks in the Alps (Err Nappe, eastern Switzerland). *J. Struct. Geol.* **21**, 777–793.

Mathews, J.P. & Chaffee, A.L. (2012). The molecular representations of coal – A review. *Fuel* **96**, 1–14.

McGarr, A., Fletcher, J.B. & Beeler, N.M. (2004). Attempting to bridge the gap between laboratory and seismic estimates of fracture energy. *Geophys. Res. Lett.* **31**, L14606.

Meng, J., Inbal, A. & Ampuero, J.-P. (2011). A window into the complexity of the dynamic rupture of the 2011 Mw 9 Tohoku-Oki earthquake. *Geophys. Res. Lett.* **38**, L00G07.

Moore, D.E. & Rymer, M.J. (2007). Talc-bearing serpentinite and the creeping section of the San Andreas fault. *Nature* **448**, 795–797.

Moore, J.C. & Vrojilk, P. (1992). Fluids in accretionary prisms. *Rev. Geophys.* **30**, 113–135.

Moore, J.C. & Saffer, D. (2001). Updip limit of the seismogenic zone beneath the accretionary prism of southwest Japan: An effect of diagenetic to low-grade metamorphic processes and increasing effective stress. *Geology* **29**, 183–186.

Mukoyoshi, H., Kaneki, S. & Hirono, (2018). T. Slip parameters on major thrusts at a convergent plate boundary: regional heterogeneity of potential slip distance at the shallow portion of the subducting plate. *Earth Planets Space* **70**, 36.

Nakamura, Y., Oohashi, K., Toyoshima, T., Satish-Kumar, M. & Akai, J. (2015). Strain-induced amorphization of graphite in fault zones of the Hidaka metamorphic belt, Hokkaido, Japan. *J. Struct. Geol.* **72**, 142–161.

Niemeijer, A., Marone, C. & Elsworth, D. (2010). Fabric induced weakness of tectonic faults. *Geophys. Res. Lett.* **37**, L03304.

Oohashi, K., Hirose, T. & Shimamoto, T. (2011). Shear-induced graphitization of carbonaceous materials during seismic fault motion: experiments and possible implications for fault mechanics. *J. Struct. Geol.* **33**, 1122–1134.

Oohashi, K., Hirose, K., Kobayashi, K. & Shimamoto, T. (2012). The occurrence of graphite-bearing fault rocks in the Atotsugawa fault system, Japan: Origins and implications for fault creep. *J. Struct. Geol.* **38**, 39–50.

Oohashi, K., Hirose, T. & Shimamoto, T. (2013). Graphite as a lubricating agent in fault zones: An insight from low- to high-velocity friction experiments on a mixed graphite-quartz gouge. *J. Geophys. Res.* **118**, 2067–2084.

Oohashi, K., Han, R., Hirose, T., Shimamoto, T., Omura, K. & Matsuda, T. (2014). Carbon-forming reactions under a reducing atmosphere during seismic fault slip. *Geology* **42**, 787–790.

Palmer, A.C. & Rice, J.R. (1973). The growth of slip surfaces in the progressive failure of over-consolidated clay. *Proc. R. Soc. London Ser. A* **332**, 527–548.

Peltonen, C., Marcussen, Ø., Bjørlykke, K. & Jahren, J. (2009). Clay mineral diagenesis and quartz cementation in mudstones: The effects of smectite to illite reaction on rock properties. *Marine Petrol. Geol.* **26**, 887–898.

Premuzic, E.T., Benkovitz, C.M., Gaffney, J.S. & Walsh, J.J. (1982). The nature and distribution of organic matter in the surface sediments of world oceans and seas. *Org. Geochem.* **4**, 63–77.

Ruina, A. (1983). Slip instability and state variable friction laws. *J. Geophys. Res.* **88**, 10359–10370.

Rutter, E.H., Hackston, A.J., Yeatman, E., Brodie, K.H., Mecklenburgh, J. & May, S.E. (2013). Reduction of friction on geological faults by weak-phase smearing. *J. Struct. Geol.* **51**, 52–60.

Saffer, D.M. & Tobin, H.J. (2011). Hydrogeology and mechanics of subduction zone forearcs: fluid flow and pore pressure. *Annu. Rev. Earth Planet. Sci.* **39**, 157–86.

Saffer, D.M., Lockner, D.A. & McKiernan, A. (2012). Effects of smectite to illite transformation on the frictional strength and sliding stability of intact marine mudstones. *Geophys. Res. Lett.* **39**, L11304.

Schito, A., Romano, C., Corrado, S., Grigo, D. & Poe, B. (2017). Diagenetic thermal evolution of organic matter by Raman spectroscopy. *Org. Geochem.* **106**, 57–67.

Scholz, C.H. (2002) *The Mechanics of Earthquakes and Faulting* (Cambridge Univ. Press).

Smeraglia, L., Billi, A., Carminati, E., Cavallo, A., Di Toro, G., Spagnuolo, E. & Zorzi, F.

(2017). Ultra-thin clay layers facilitate seismic slip in carbonate faults. *Sci. Rep.* **7**, 664.

Spagnuolo, E., Plümper, O., Violay, M., Cavallo, A. & Di Toro, G. (2015). Fast-moving dislocations trigger flash weakening in carbonate-bearing faults during earthquakes. *Sci. Rep.* **5**, 16112.

Spinelli, G.A. & Saffer, D.M. (2004). Along-strike variations in underthrust sediment dewatering on the Nicoya margin, Costa Rica related to the updip limit of seismicity. *Geophys. Res. Lett.* **31**, L04613.

Ujiie, K. *et al*. (2013). Low coseismic shear stress on the Tohoku-Oki megathrust determined from laboratory experiments. *Science* **342**, 1211–1214.

Vrolijk, P. (1990) On the mechanical role of smectite in subduction zones. *Geology* **18**, 703–707.

Yao, L.,Ma, S., Shimamoto, T. & Togo, T. (2013). Structures and high-velocity frictional properties of the Pingxi fault zone in the Longmenshan fault system, Sichuan, China, activated during the 2008 Wenchuan earthquake. *Tectonophysics* **599**, 135–156.

Yu, X., Zhang, X., Wang C.-B., Liu, F.-T. & Fu Z.-Q. (2007). Structural, mechanical and frictional properties of tetrahedral amorphous carbon film by altered cathodic vacuum arc system. *Surf. Coat. Tech.* **201**, 4995–4998.

Zhang, L. & He, C. (2013). Frictional properties of natural gouges from Longmenshan fault zone ruptured during the Wenchuan Mw 7.9 earthquake. *Tectonophysics* **594**, 149–164.

Zulauf, G., Kleinschmidt, G. & Oncken, G. (1990). Brittle Deformation and graphitic cataclasites in the pilot research well KTB-VB (Oberpfalz, FRG). *Geol. Soc. London* **54**, 97–103.

Supporting information

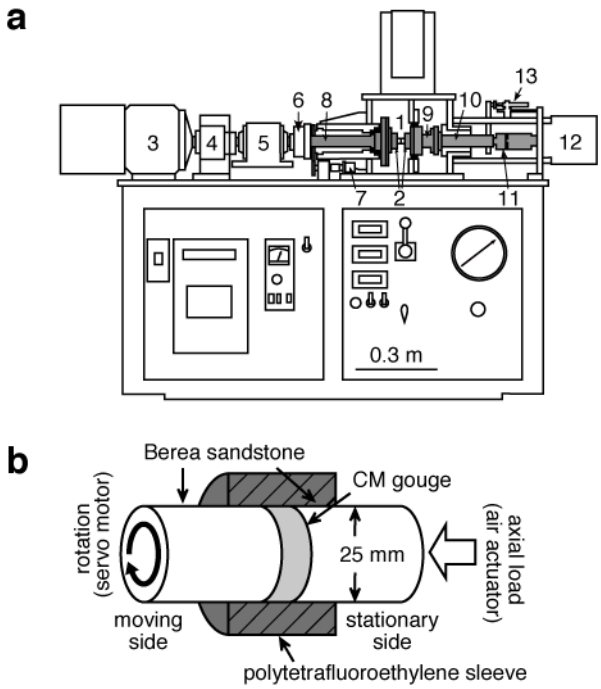

Figure S6.1. Friction apparatus and sample assemblage. (a) Simplified sketch of high-velocity rotary friction apparatus at Yamaguchi University (modified from Mizoguchi et al., 2009). 1, specimen; 2, specimen holder; 3, motor; 4, torque limiter; 5, torque gauge; 6, electromagnetic clutch; 7, rotary encoder; 8, rotary column; 9, torque-axial force gauge; 10, ball spin; 11, axial force gauge; 12, air actuator; 13, displacement transducer. (b) Detailed view of sample assemblage.

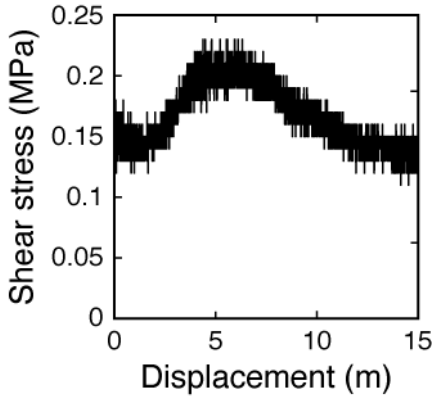

Figure S6.2. Change of shear stress of polytetrafluoroethylene sleeve with slip. Mechanical data used for correction of torque between the polytetrafluoroethylene sleeve and the Berea sandstone (Supporting Information Figure S6.1b).

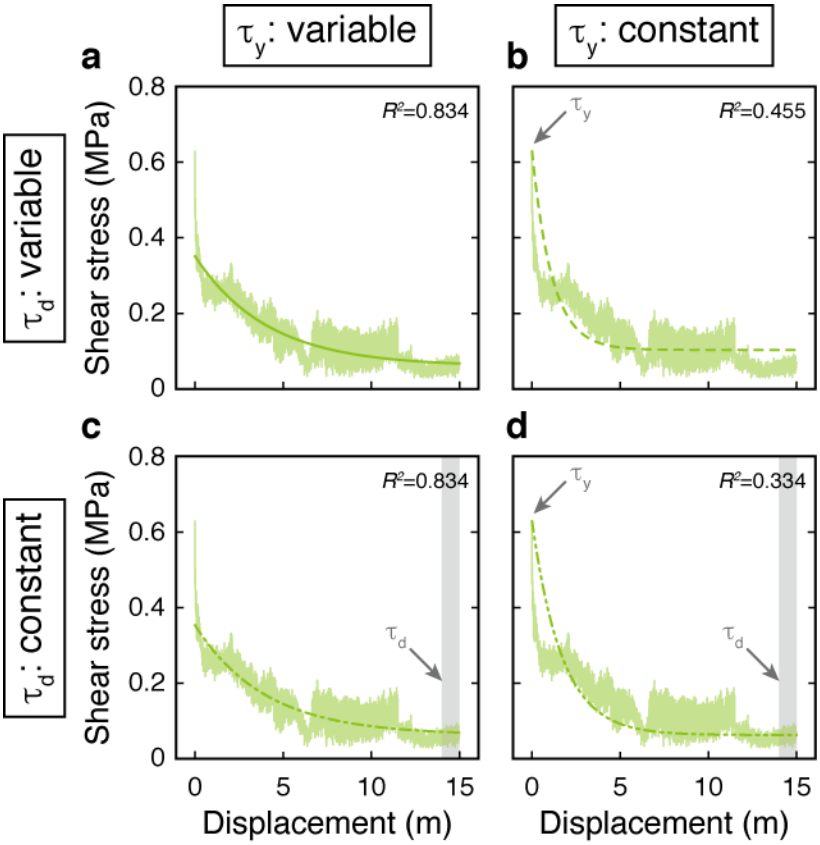

Figure S6.3. Four patterns for fitting of data from friction experiments. Variables for fitting were (a) τ_y, τ_d, and D_c, (b) τ_d and D_c, (c) τ_y and D_c, and (d) D_c. Data of shear stress with slip shown are from lignite at 0.5 MPa normal stress. Coefficients of determination (R^2 values) are calculated by using equation (6.1).

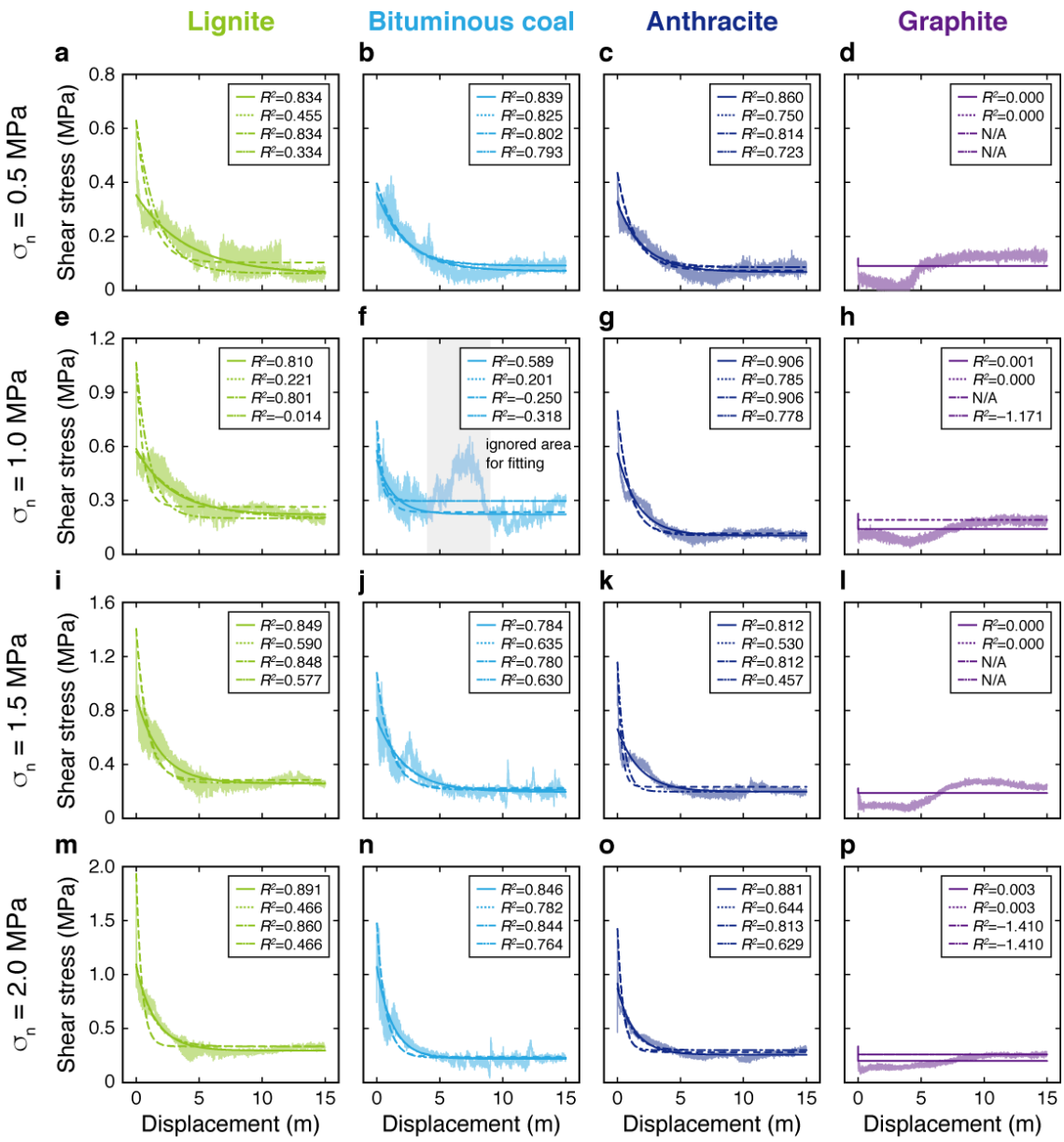

Figure S6.4. Results of curve fittings for all experiments. Normal stresses applied were (a–d) 0.5 MPa, (e–h) 1.0 MPa, (i–l) 1.5 MPa, and (m–p) 2.0 MPa. Each graph shows fitting curves derived by applying equation (6.2) with four different sets of variables. Coefficients of determination (R^2 values) were calculated using equation (6.1) in the Methods section.

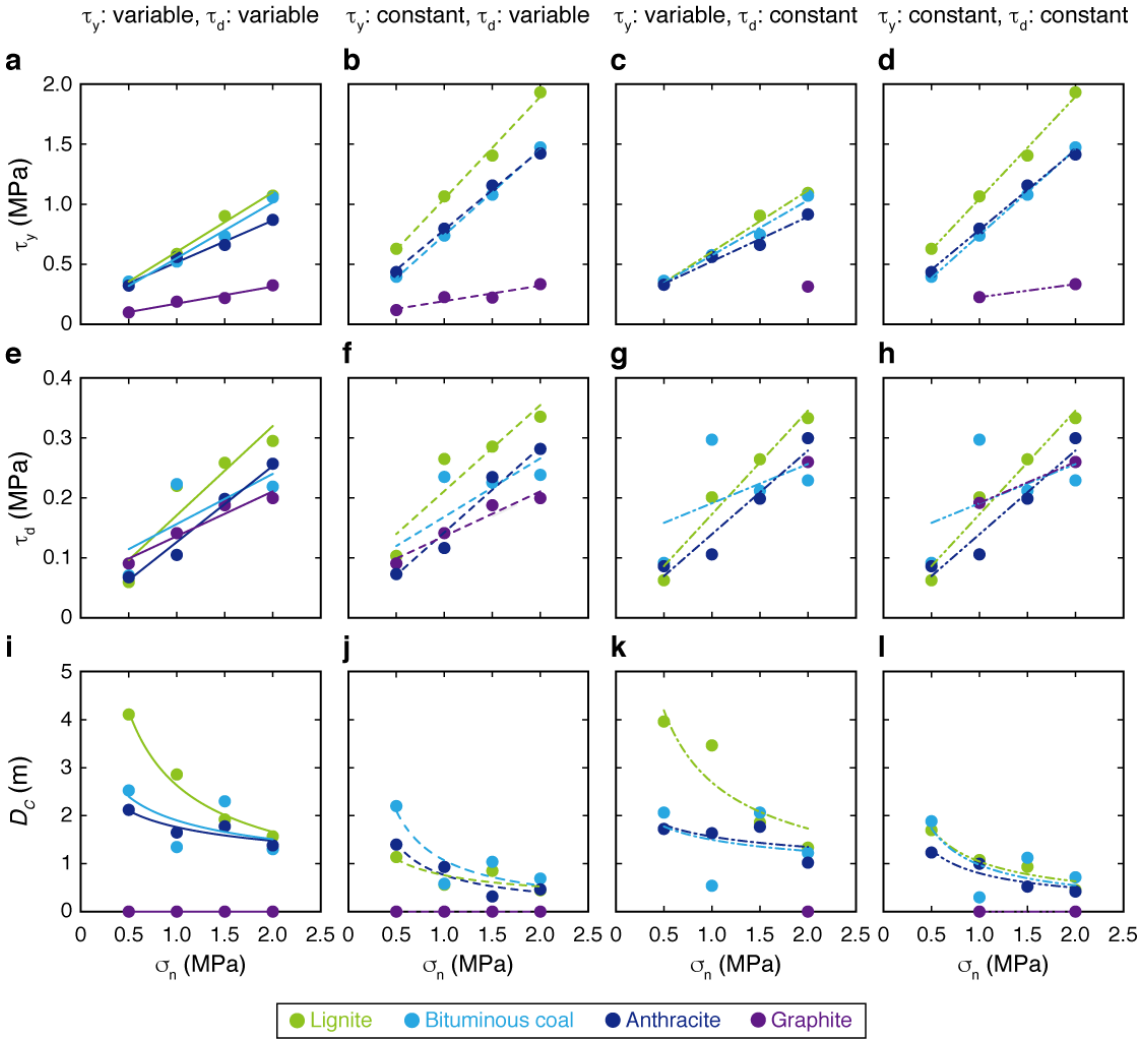

Figure S6.5. Determination of frictional properties for variable fitting conditions and CM types. Linear correlations of normal stress with (a–d) yield shear stress and (e–h) dynamic shear stress were obtained using equation (6.3). Exponential correlation of normal stress with critical slip-weakening distance (i–l) were obtained using equation (6.4). All values of the frictional properties presented are summarized in Supporting Information Tables S1–4.

Table S6.1. Summary of frictional properties determined for lignite for all curve-fitting cases with different sets of variables and normal stresses.

Sample	Variables	σ_n (MPa)	τ_y (MPa)	τ_d (MPa)	D_c (m)	μ_y	μ_d	α	β
Lignite	τ_y, τ_d, D_c	0.5	0.351	0.060	4.103	0.50 ± 0.04	0.15 ± 0.04	2.63	0.66
		1.0	0.586	0.220	2.855				
		1.5	0.901	0.258	1.918				
		2.0	1.072	0.295	1.566				
	τ_d, D_c	0.5	0.629	0.103	1.136	0.85 ± 0.05	0.14 ± 0.04	0.76	0.53
		1.0	1.066	0.265	0.579				
		1.5	1.405	0.285	1.036				
		2.0	1.932	0.335	0.689				
	τ_y, D_c	0.5	0.353	0.063	3.963	0.51 ± 0.04	0.17 ± 0.03	2.69	0.64
		1.0	0.569	0.201	3.465				
		1.5	0.905	0.264	1.861				
		2.0	1.094	0.333	1.333				
	D_c	0.5	0.629	0.063	1.698	0.85 ± 0.05	0.17 ± 0.03	1.04	0.73
		1.0	1.066	0.201	1.075				
		1.5	1.405	0.264	0.934				
		2.0	1.932	0.333	0.715				

Table S6.2. Summary of frictional properties determined for bituminous coal for all curve-fitting cases with different sets of variables and normal stresses.

Sample	Variables	σ_n (MPa)	τ_y (MPa)	τ_d (MPa)	D_c (m)	μ_y	μ_d	α	β
Bituminous coal	τ_y, τ_d, D_c	0.5	0.356	0.071	2.522	0.46 ± 0.05	0.08 ± 0.05	1.90	0.33
		1.0	0.522	0.223	1.344				
		1.5	0.733	0.197	2.297				
		2.0	1.057	0.219	1.300				
	τ_d, D_c	0.5	0.396	0.073	2.197	0.72 ± 0.02	0.10 ± 0.06	1.07	0.98
		1.0	0.739	0.235	0.579				
		1.5	1.079	0.225	1.036				
		2.0	1.474	0.238	0.689				
	τ_y, D_c	0.5	0.362	0.092	2.064	0.46 ± 0.05	0.07 ± 0.08	1.50	0.25
		1.0	0.577	0.297	0.539				
		1.5	0.746	0.212	2.064				
		2.0	1.071	0.229	1.225				
	D_c	0.5	0.396	0.092	1.884	0.72 ± 0.02	0.07 ± 0.08	0.97	0.83
		1.0	0.739	0.297	0.297				
		1.5	1.079	0.212	1.122				
		2.0	1.474	0.229	0.715				

Table S6.3. Summary of frictional properties determined for anthracite for all curve-fitting cases with different sets of variables and normal stresses.

Sample	Variables	σ_n (MPa)	τ_y (MPa)	τ_d (MPa)	D_c (m)	μ_y	μ_d	α	β
Anthracite	τ_y, τ_d, D_c	0.5	0.322	0.068	2.118	0.35 ± 0.04	0.13 ± 0.02	1.76	0.26
		1.0	0.560	0.105	1.646				
		1.5	0.661	0.198	1.775				
		2.0	0.870	0.257	1.378				
	τ_d, D_c	0.5	0.435	0.073	1.395	0.66 ± 0.03	0.14 ± 0.02	0.76	0.91
		1.0	0.797	0.116	0.931				
		1.5	1.156	0.235	0.315				
		2.0	1.423	0.282	0.462				
	τ_y, D_c	0.5	0.329	0.086	1.724	0.37 ± 0.04	0.14 ± 0.03	1.56	0.21
		1.0	0.561	0.106	1.634				
		1.5	0.661	0.199	1.769				
		2.0	0.916	0.299	1.020				
	D_c	0.5	0.435	0.086	1.232	0.66 ± 0.03	0.14 ± 0.03	0.80	0.69
		1.0	0.797	0.106	0.997				
		1.5	1.156	0.199	0.521				
		2.0	1.423	0.299	0.419				

Table S6.4. Summary of frictional properties determined for graphite for all curve-fitting cases with different sets of variables and normal stresses.

Sample	Variables	σ_n (MPa)	τ_y (MPa)	τ_d (MPa)	D_c (m)	μ_y	μ_d	α	β
Graphite	τ_y, τ_d, D_c	0.5	0.099	0.091	0.000	0.14 ± 0.02	0.08 ± 0.01	0.000	0.000
		1.0	0.188	0.141	0.000				
		1.5	0.219	0.188	0.000				
		2.0	0.325	0.200	0.000				
	τ_d, D_c	0.5	0.119	0.091	0.000	0.13 ± 0.03	0.08 ± 0.01	0.000	0.000
		1.0	0.226	0.141	0.000				
		1.5	0.222	0.188	0.000				
		2.0	0.334	0.200	0.000				
	τ_y, D_c	0.5	N/A	N/A	N/A	N/A	N/A	N/A	N/A
		1.0	N/A	N/A	N/A				
		1.5	N/A	N/A	N/A				
		2.0	0.314	0.260	0.000				
	D_c	0.5	N/A	N/A	N/A	0.11	0.07	0.000	0.000
		1.0	0.226	0.192	0.000				
		1.5	N/A	N/A	N/A				
		2.0	0.334	0.260	0.000				

Chapter 7

Summary and implication

In this thesis, I have reported experimentally-based studies focusing on CM reactions that take place at plate-subduction faults and its effect on earthquake dynamics. The main findings in this thesis are listed below.

(1) Earthquake-induced CM reactions that changes its maturity are likely to occur in natural and experimental fault rocks (Chapters 2, 3, 4, and 5).

(2) CM maturity can be a useful indicator for detecting frictional heat in fault rocks (Chapter 3).

(3) Kinetic effects by mechanochemistry and heating rate can strongly affect progress of CM reactions during earthquake (Chapters 4 and 5).

(4) CM loses its frictional strength with increasing maturity, possibly affecting earthquake rupture dynamics in plate-subduction zones (Chapter 6).

Although this thesis provided clear evidences that verify CM as a useful thermal indicator (Chapter 3), comprehensive understanding on reaction kinetics of CM is hampered by the complicated mechanical and thermal effect during earthquakes (Chapters 4 and 5). Nakamura et al. (2017) recently examined crystallization of amorphous carbon under different normal stress conditions and reported kinetic parameters for graphitization process. However, they only focused on graphitization of CM, and thus reaction kinetics of CM associated with earthquake slip should be experimentally investigated. As addressed in Chapter 5, initial condition of CM may control reaction paths of CM maturation (Furuichi et al., 2015; Kuo et al., 2017), suggesting that fault geothermoremeter based on CM maturity should consider its initial condition by means of elemental analysis and py-GC/MS analysis. Furthermore, cumulative effect by repeated earthquake events on CM maturation should be considered for more accurate geothermometer for fault rocks (Fulton & Harris, 2012). To overcome these problem, further experiments that aim to construct kinetics of CM reactions by considering all of described effects are required.

Chapter 6 showed systematic decrease in frictional strength of CM with increasing crystallinity. However, I only used CM samples with three different crystallinity; perfectly amorphous carbon (lignite and bituminous coal), partly crystalized carbon (anthracite), and perfectly crystalized carbon (graphite). It is thus necessary to conduct additional experiments on

CM samples for describing empirical law laying between degree of crystallinity and frictional strength. Furthermore, as described in Chapter 6, high-velocity friction experiments can only consider rupture propagation process. Another important dynamics process, rupture nucleation, should be discussed based on the rate-and-state friction law of CM obtained by performing low-velocity friction experiments. For better understanding of earthquake dynamics of carbon-bearing faults, further friction experiments at both low and high slip velocity should be conducted in the future.

References

Fulton, P.M. & Harris, R.N. (2012). Thermal considerations in inferring frictional heating from vitrinite reflectance and implications for shallow coseismic slip within the Nankai Subduction Zone. **Earth Planet. Sci. Lett.** *335–336*, 206–215.

Furuichi, H., Ujiie, K., Kouketsu, Y., Saito, T., Tsutsumi, A. & Wallis, S. (2015). Vitrinite reflectance and Raman spectra of carbonaceous material as indicators of frictional heating on faults: Constraints from friction experiments. **Earth Planet. Sci. Lett.** *424*, 191–200.

Kuo, L.-W., Di Felice, F., Spagnuolo, E., Di Toro, G., Song, S.-R., Aretusini, S., Li, H., Suppe, J., Si, J. & Wen, C.-Y. (2017). Fault gouge graphitization as evidence of past seismic slip. **Geology** *45*, 979–982.

Nakamura, Y., Yoshino, T. & Satish-Kumar, M. (2017). An experimental kinetic study on the structural evolution of natural carbonaceous material to graphite. **Am. Mineral.** *102*, 135–148.

Oohashi, K., Hirose, T. & Shimamoto, T. (2011). Shear-induced graphitization of carbonaceous materials during seismic fault motion: Experiments and possible implications for fault mechanics. **J. Struct. Geol.** *33*, 1122–1134.

Lists of publications and presentations

Peer-reviewed papers

1. Kaneki, S. & Hirono, T. (2016). Blackening of fault gouge by comminution and pyrolysis of carbonaceous materials during earthquake slip. **Tectonophysics** *678–678*, 160–170.
2. Kaneki, S., Hirono, T., Mukoyoshi, H., Sampei, Y. & Ikehara, M. (2016). Organochemical characteristics of carbonaceous materials as indicators of heat recorded on an ancient plate-subduction fault. **Geochem. Geophys. Geosyst.** *17*, 2855–2868.
3. Hirono, T., Asayama, S., Kaneki, S. & Ito, A. (2016). Preservation of amorphous ultrafine material: A proposed proxy for slip during recent earthquakes on active faults. **Scientific Reports** *6*, 36536.
4. Kaneki, S., Ichiba, T. & Hirono, T. (2018). Mechanochemical effect on maturation of carbonaceous materials: Implications for thermal maturity as a proxy for temperature in estimation of coseismic slip parameters. **Geophys. Res. Lett.** *45*, 2248–2256.
5. Mukoyoshi, H., Kaneki, S. & Hirono, T. (2018). Slip parameters on major thrusts at a convergent plate boundary: regional heterogeneity of potential slip distance at the shallow portion of the subducting plate **Earth Planets Space** *70*, 36.
6. Kaneki, S. & Hirono, T. (2018). Kinetic effects of heating rate on the thermal maturity of carbonaceous material as an indicator of frictional heat during earthquakes. **Earth Planets Space** *70*, 92.
7. Cerchiari, A., Fukuchi, R., Gao, B., Hsiung, K.–H., Jaeger, D., Kaneki, S., Keller, J., Kimura, G., Kuo, S.–T., Lymer, G., Maison, T., Motohashi, G., Regalla, C., Singleton, D. & Yabe, S. (2018). IODP workshop: Core-Log Seismic Investigation at Sea – Integrating legacy data to address outstanding research questions in the Nankai Trough Seismogenic Zone Experiment. **Scientific Drilling**, *24*, 93–107.

Non peer-reviewed papers

8. Kaneki, S. & Hirono, T. (2017). Investigation of slip behavior in fault zone applied by IR

and Raman spectroscopies. **JASCO report**, *59*, 15–22 (in Japanese).

Presentations in international conference

9. Kaneki, S. & Hirono, T. Blackening of fault gouge by comminution and pyrolysis of carbonaceous materials during earthquake slip. AGU Fall Meeting 2015, MR33A-2651, San Francisco, US, 16th December 2015 (Poster).
10. Kaneki, S., Hirono, T., Mukoyoshi, H., Sampei, Y. & Ikehara, M. Slip parameters of ancient subduction earthquake determined by multiple analyses of carbonaceous materials. International Workshop of Organic Geochemistry "Biomarkers and Molecular Isotopes", P05, Osaka, Japan, 4-5th July 2016 (Poster).
11. Kaneki, S. & Hirono, T. Inferring parameters of earthquake slip using an integrated field, experiment and material analysis: A new proxy using maturation of carbonaceous materials. Crustal Dynamics 2016, BP47, Takayama, Japan, 21st July 2016 (Poster).
12. Kaneki, S. & Hirono, T. A new temperature proxy on faults during earthquake by using maturity of carbonaceous materials: Kinetic effect on the maturation. IAG-IASPEI 2017, J05-3-05, Kobe, Japan, 2nd August 2017 (Talk).
13. Kaneki, S. & Hirono, T. Importance of weak minerals on earthquake mechanics. AGU Fall Meeting 2017, 231009, MR33B-0458, New Orlens, US, 13th December 2017 (Poster).
14. Ogawa, T., Ishikawa, T., Kaneki, S. & Hirono, T. Geochemical anomaly in ancient subduction boundary fault: Trench-parallel heterogeneity in slip behavior caused by variation of mineral composition. AGU Fall Meeting 2017, H43G-1721, New Orlens, US, 14th December 2017 (Poster).
15. Kaneki, S., Yokoyama, Y., Hirono, T. & Ogasawara, H. XRD analysis on DSeis core samples. NRF-JSPS Workshop: ICDP-DSeis Scientific Drilling & Rock Physics, Johannesburg, South Africa, 27th June 2018 (Talk).

Supplementary information

Copyright permission

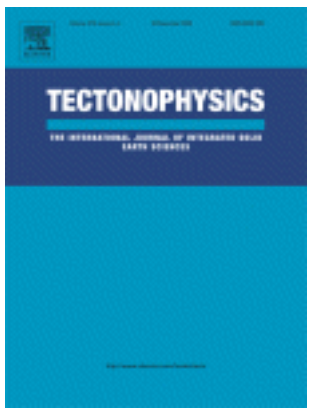

Title: Blackening of fault gouge by comminution and pyrolysis of carbonaceous materials during earthquake slip

Author: Shunya Kaneki,Tetsuro Hirono

Publication: Tectonophysics

Publisher: Elsevier

Date: 23 May 2016

Title: Organochemical characteristics of carbonaceous materials as indicators of heat recorded on an ancient plate-subduction fault

Author: S. Kaneki, T. Hirono, H. Mukoyoshi, et al

Publication: Geochemistry, Geophysics, Geosystems

Publisher: John Wiley and Sons

Date: Jul 24, 2016

Order Completed

Thank you for your order.

This Agreement between Shunya Kaneki ("You") and John Wiley and Sons ("John Wiley and Sons") consists of your license details and the terms and conditions provided by John Wiley and Sons and Copyright Clearance Center.

Your confirmation email will contain your order number for future reference.

printable details

License Number	4458070363578
License date	Oct 29, 2018
Licensed Content Publisher	John Wiley and Sons
Licensed Content Publication	Geochemistry, Geophysics, Geosystems
Licensed Content Title	Organochemical characteristics of carbonaceous materials as indicators of heat recorded on an ancient plate-subduction fault
Licensed Content Author	S. Kaneki, T. Hirono, H. Mukoyoshi, et al
Licensed Content Date	Jul 24, 2016
Licensed Content Volume	17
Licensed Content Issue	7
Licensed Content Pages	14
Type of use	Dissertation/Thesis
Requestor type	Author of this Wiley article
Format	Print and electronic
Portion	Full article
Will you be translating?	No
Title of your thesis / dissertation	Earthquake-induced thermal maturation of carbonaceous materials and its implication for earthquake dynamics in plate-subduction zones
Expected completion date	Mar 2019
Expected size (number of pages)	160
Requestor Location	Shunya Kaneki Machikaneyama-cho 1-1, Toyonaka, Japan Toyonaka, 5600043 Japan Attn: Shunya Kaneki

Publisher Tax ID	EU826007151
Total	0.00 USD

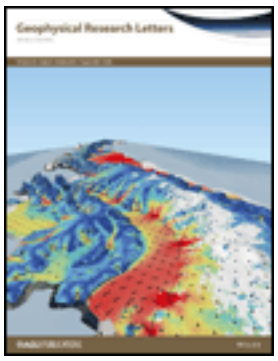

Title: Mechanochemical Effect on Maturation of Carbonaceous Material: Implications for Thermal Maturity as a Proxy for Temperature in Estimation of Coseismic Slip Parameters

Author: S. Kaneki, T. Ichiba, T. Hirono

Publication: Geophysical Research Letters

Publisher: John Wiley and Sons

Date: Mar 8, 2018

Order Completed

Thank you for your order.

This Agreement between Shunya Kaneki ("You") and John Wiley and Sons ("John Wiley and Sons") consists of your license details and the terms and conditions provided by John Wiley and Sons and Copyright Clearance Center.

Your confirmation email will contain your order number for future reference.

printable details

License Number	4458070175715
License date	Oct 29, 2018
Licensed Content Publisher	John Wiley and Sons
Licensed Content Publication	Geophysical Research Letters
Licensed Content Title	Mechanochemical Effect on Maturation of Carbonaceous Material: Implications for Thermal Maturity as a Proxy for Temperature in Estimation of Coseismic Slip Parameters
Licensed Content Author	S. Kaneki, T. Ichiba, T. Hirono
Licensed Content Date	Mar 8, 2018
Licensed Content Volume	45
Licensed Content Issue	5
Licensed Content Pages	9
Type of use	Dissertation/Thesis
Requestor type	Author of this Wiley article
Format	Print and electronic
Portion	Full article
Will you be translating?	No
Title of your thesis / dissertation	Earthquake-induced thermal maturation of carbonaceous materials and its implication for earthquake dynamics in plate-subduction zones
Expected completion date	Mar 2019
Expected size (number of pages)	160
Requestor Location	Shunya Kaneki Machikaneyama-cho 1-1, Toyonaka, Japan Toyonaka, 5600043 Japan Attn: Shunya Kaneki

Publisher Tax ID	EU826007151
Total	0 JPY